EROSION OF ICE FILMS BY ENERGETIC IONS

Thesis by

Barbara Hope Cooper

In Partial Fulfillment of the Requirements

for the Degree of

Doctor of Philosophy

California Institute of Technology

Pasadena, California

1982

(Submitted Aug 26, 1981)

ACKNOWLEDGEMENTS

I would like to thank all the faculty, students, and technical staff of Kellogg Radiation Lab for providing a friendly and stimulating enviornment which made this work possible and my stay in Kellogg enjoyable. I am especially grateful to my advisor, Tom Tombrello, for his enthusiastic support and guidance throughout this research.

Many members of the lab and visitors to Kellogg have contributed useful suggestions and ideas to this research. I would like to mention especially C. Barnes, G. Fuller, J. Griffith, P. Haff, S. Koonin, C. Meins, P. Parker, Y. Qiu, C. Watson, and B. Weller. W. Brown, J. Mayer, and L. Miller were also very helpful. Thanks go to P. Goodwin, D. LePoire, T. Terrano, and H. Wilson for their assistance in the laboratory.

Finally, I would like to thank my family and friends, too numerous to list here, for their support and encouragement during this work.

ABSTRACT

We measured the sputtering yields of ice films by ^{19}F ions in the electronic stopping power energy regime. The yield was a function of the incident energy and charge state of the F beam, but did not vary for target thicknesses ranging from about $30-70\times10^{16} H_2O/cm^2$, or substrate temperatures from 10–60°K.

The energy dependence of the yield demonstrates that the sputtering mechanism is related to the electronic stopping power of the incident ion in the ice film. The detailed nature of this dependence is not understood. Predictions of thermal models and ion explosion models are compared to the experimental results.

Our F data on ice is compared to H and He sputtering of ice. We also review results from the literature where sputtering of other dielectric targets with ions in the electronic stopping power regime have been studied.

Possible connections with nuclear track formation in dielectrics and laser annealing are discussed. We also briefly mention the applications of enhanced sputtering of dielectrics; for example, in non-destructive desorption of large biomolecules and in astrophysical enviornments where frozen gas surfaces are bombarded by energetic ion fluxes.

TABLE OF CONTENTS

I. Introduction and Theoretical Background

A. General Introduction

Sputtering of solid targets by ion bombardment is the process by which target atoms are ejected from the surface of the target after being excited by the passage of an incident ion. The experiments described in this dissertation were designed to investigate a very specific type of sputtering which occurs following bombardment of insulating materials by ions in the electronic stopping power regime.

An energetic ion travelling through solid matter loses energy continuously to the atoms and electrons of the solid, and eventually comes to rest at some depth in the solid. Let x be the distance travelled by the ion after it enters the target ($x=0$ represents the surface of the target). The amount of energy transferred per unit distance travelled by the ion is referred to as the stopping power, dE/dx, which is not necessarily a simple function of x. The energy is transferred by one of several mechanisms, the choice of which is governed largely by the velocity of the incident ion at a given depth in the target. Energy lost by the ion is transferred to excitation and kinetic energy of the atoms and electrons of the solid. After passage of the ion, if the solid remains permanently altered from its steady state configuration, we say that it is radiation damaged. Sputtering is one manifestation of the radiation damage process. There are other related phenomena, such as the formation of tracks or dislocations in solids.

A general schematic of the energy loss per unit path length, dE/dx, of energetic ions travelling through matter is shown in figure 1a (Sigmund 1977). There are two broad peaks in a graph of dE/dx as a function of the energy of the incident ion. These can be divided into two distinct curves

which describe two very different mechanisms for energy loss. The curve which reaches its maximum at lower energies (~1keV/amu) is referred to as the nuclear stopping power, while that which peaks at the higher energies (~0.5 MeV/amu) is the electronic stopping power. The sputtering process under investigation here pertains to ions in the energy range spanning the peak of the electronic stopping power curve. Most of the previous work on sputtering, both theoretical and experimental, was performed with ions of relatively low energy (~1-100 keV/amu) incident on metal and semiconductor targets. This type of sputtering, which is related to the nuclear stopping power, is referred to as Sigmund sputtering. The Sigmund theory (Sigmund 1969, 1972b) has been quite successfully applied to explaining experimental results.

In this chapter, some of the theoretical concepts of high energy sputtering of dielectrics are introduced. First, however, it is instructive to briefly review the major features of the Sigmund model of sputtering. In this picture, sputtering is an obvious consequence of the energy loss mechanism for low energy ions in matter. This connection between energy loss and sputtering becomes much less obvious for high energy ions in dielectric materials.

B. Energy Loss and Sputtering by Low Energy Ions

When an ion of relatively low energy (1-100 keV/amu) enters a target, it undergoes a series of elastic or quasi-elastic collisions with the target atoms. This mechanism for energy loss per unit length is referred to as the nuclear stopping power. Nuclear stopping has been calculated by Sigmund (1972a) from classical scattering theory using the Thomas-Fermi model of interacting atoms. In this theory, the incident ion undergoes screened Rutherford collisions with the target atoms. In each collision,

the ion suffers an energy loss coupled with an angular deflection. The atom recoils with an energy equal to that lost by the incident ion, minus the lattice binding energy of the solid. The incident ion continues to travel through the solid losing energy to the target atoms, until it eventually comes to rest.

As the target atoms recoil from their initial collisions with the incident ion (these atoms are called the primary recoils), they in turn transfer energy to their neighboring atoms (which become secondary recoils) via elastic or quasi-elastic collisions. By colliding with their own neighboring atoms, these secondary recoils continue to dissipate the energy lost by the incident ion. This process continues until, in some region of the target surrounding the path of the incident ion, atoms of the solid are set in motion with isotropically directed trajectories. This region is referred to as a collision cascade.

The radius and lifetime of the cascade will be determined by the amount of energy lost by the incident ion, ΔE, per unit path length in the solid (or the nuclear stopping power). The collision cascade develops as the atoms of the solid share the deposited energy ΔE. When the trajectory of an atom in the cascade is directed through the target surface, this atom will leave the solid as a sputtered atom provided it has enough energy to overcome the surface binding energy of the solid. At some point, after several recoil collisions have occurred, an individual recoil is unable to transfer enough energy to a neighboring atom to overcome its lattice binding energy. When this is the case for most of the recoiling atoms, the cascade dies, and sputtering stops.

The Sigmund sputtering yield, S=(target atoms removed)/(incident ion), is proportional to the nuclear stopping power, and inversely

proportional to the surface binding energy of the target.

$$S(E)=\frac{0.042\alpha S_n(E)}{U_o}$$

where S_n is the nuclear stopping power as calculated by Lindhard et al. (1968), U_o is the surface binding potential, and α is a constant that depends on the ion mass (Sigmund 1969).

For ions incident on metal surfaces, absolute sputtering yields range between 10^{-2} and 10^{2} atoms/ion, depending on the particular ion target combination. The highest yields are obtained with the heaviest ions (high nuclear stopping power) bombarding materials with the lowest surface binding energies (Sigmund 1977).

C. Energy Loss and Sputtering by High Energy Ions

The connection between sputtering and the energy loss processes for low energy ions in solids is conceptually straightforward. In nuclear stopping, energy is transferred directly from kinetic energy of the ion to kinetic energy of the target atoms via quasi-elastic collisions.

Now consider the case of high energy ions (MeV/amu) incident on insulating target materials. Sputtering yields have been measured which are two to three orders of magnitude larger than those found or expected from Sigmund sputtering. For ions with MeV energies, nuclear stopping contributes very little to the total stopping power of the incident ion. In this regime the ion loses energy to the solid via the electronic stopping power. That is, on its passage through the solid, it scatters from atomic electrons, and leaves a track of excited atoms or ions. Since we observe sputtered particles, we know that eventually some fraction of the energy deposited by the ion must end up as kinetic energy of the target atoms.

The major problem in developing a model for high energy dielectric sputtering is to explain how the energy is transferred from the excited electrons to the target atoms. There have been several attempts to explain this phenomenon.

In the next section, we present an outline of some of the models that have been proposed to account for dielectric sputtering. A more thorough discussion is reserved for chapter V where we present the models in some detail and compare them with experimental results.

D. Models for Dielectric Sputtering by High Energy Ions

The first two models discussed here are the thermal spike model (Sigmund et al. 1980, Macfarlane et al. 1976a, Ollerhead et al. 1962) and the ion explosion model (Haff 1976, Brown et al. 1980a, Stiegler et al. 1962) of dielectric sputtering. They were chosen because they represent two extreme pictures of the events which occur in the solid after passage of the high energy ion. In both models, the sputtering process is initiated by the trail of ions and electronically excited atoms left behind by the incident ion. For every ion created, there is also a free electron which has been given some kinetic energy by the incident ion. In the thermal spike model, the events immediately following the passage of the ion have to do mostly with subsequent collisions of the excited free electrons. In the ion explosion model, on the other hand, these electrons, once freed from the atoms, are no longer of principal importance to the sputtering process. The energy available for sputtering is dissipated in a series of events initiated by Coulomb repulsion of the neighboring ions created along the path of the incident ion.

The third model discussed here was developed by Seiberling et al. (1980) to explain experimental results they found by sputtering UF_4 (an

insulator) with high energy F ions. This model combines ideas from the thermal spike model and the ion explosion model and will be referred to as the thermalized ion explosion model.

These models are useful as a framework in which to organize the data and plan future experiments. However, it will be seen in chapter five that the sputtering process is sufficiently complicated that a simple model will meet with only limited success when applied to experimental data. A comprehensive treatment of the sputtering process is very difficult. Work along these lines has been begun by C. C. Watson (1981). Some of his ideas will be discussed briefly as well.

1. Thermal spike sputtering

In this model, the incident beam particle creates a path of ions along its trajectory through the solid. The associated electrons are pulled off the ions and travel through the solid with a kinetic energy imparted to them during the ionization event. The assumption is made that these electrons do not get trapped in the solid, but are free to move about. They oscillate back and forth through a region centered on the positive track of ions left by the beam particle. Through a series of collisions with the atoms in this cylindrical region, they transfer some fraction of their energy to kinetic energy of these atoms. This effectively raises the temperature of the solid in this cylinder, which is referred to as the hot spike. (A cylinder is chosen only because of the cylindrical geometry of the problem). Since the temperature in the hot spike is elevated, the vapor pressure of the solid is enhanced, and atoms will evaporate through the intersection of this cylinder with the surface of the target, until the surrounding solid has cooled the hot spike by heat conduction. The atoms escaping from the surface should represent a thermal spectrum

for the spike temperature, T, which is characteristic of the particular target used.

There are some problems with this model. For example, it requires that the free electrons are able to move through the solid without getting trapped. A further complication (see chapter V), is that the time scales involved in transferring energy from the electrons to the solid atoms, via collisions, is much longer than the time it would take the rest of the solid to conduct heat out of the spike region (a time which is governed by the thermal diffusivity of the target material).

2. Ion explosion sputtering

Consider now the ion explosion model of sputtering in dielectric materials. This idea was first proposed by Haff (1976), and was motivated by arguments put forth by Fleischer et al. (1965) to explain the production of nuclear tracks by ionizing particles in dielectric media.

The sputtering process is initiated in this model, as in the thermal spike model, by ionization produced along the trajectory of the incident ion. The basic assumption is that ion pairs are produced on neighboring atomic sites in the solid. These ions subsequently recoil under their mutual Coulomb repulsion. These recoiling ions collide with neighboring atoms in the solid, and generate a collision cascade very similar to the collision cascade of Sigmund sputtering. Some of these recoils near the surface are able to escape as sputtered particles, provided their trajectories and energies are such that they are able to overcome the surface binding and leave the target. Haff argues that the sputtering yield will reflect the total energy released to the ion pairs in the solid, which is proportional to the square of the average number of e^- removed per atom along the ion trajectory. This, he argues, is proportional to the square of

the primary ionization rate, dJ/dx, a quantity which gives the number of ionizations produced per unit path length of the ion in the solid. The primary ionization rate is related to the electronic stopping power, but does not weight the free electrons by their energy. It also does not take into account the component of dE/dx that goes into electronic excitation of the solid atoms rather than ionization. Haff's arguments lead to the prediction that $S \propto (dJ/dx)^2$. The spectrum of sputtered particles will represent the energy distribution in the cascade set up by the Coulomb repulsion of the neighboring ions. Detailed calculations using this model are difficult to perform since dJ/dx is not a well understood quantity (see chapter V).

Brown et al. (1980a) have also proposed a model which invokes Coulomb repulsion. Their model requires that the free e^- can be trapped at some distance a from the positive ion track. They envision that the situation established will be a positive line charge centered in a negative cylindrical sheath of radius a. They argue that this cylindrical space charge region will exert strong forces on the ions, with a net component in the direction of the surface normal. This force will eject ions, within one mean free path of the surface, as sputtered atoms. In this case one might expect a large fraction of charged, ions in the sputtered flux. In their treatment, they predict a $(dE/dx)^2$ dependence for S. Following the arguments of Haff (1976), it would be more appropriate to use $(dJ/dx)^2$ rather than $(dE/dx)^2$ for a Coulomb repulsion mechanism.

3. Thermalized ion explosion sputtering

The thermalized ion explosion model was proposed by Seiberling et al. (1980) to explain some experimental results obtained by sputtering UF_4 (an insulator) with high energy F ions (Griffith et al. 1980). In one of

these experiments, the velocity spectrum of the sputtered U was measured using time of flight. It was found to have a Maxwell-Boltzmann shape characteristic of the velocity distribution expected from a gas of U in thermal equilibrium at ~3620°K. This implies that the atoms of the solid were heated to a temperature which exceeded the melting point of the solid (1309°K for UF_4), and target atoms evaporated from the hot spike region until the spike was cooled by heat diffusion to the rest of the solid (Seiberling et al. 1980).

In this picture, as opposed to thermal spike sputtering, one does not have to wait for the electrons to transfer their energy to the atoms by collisions. Instead, the heating occurs by successive collisions of the target atoms themselves, initiated by Coulomb repulsion of the initial ions left by the passage of the incident ion. Seiberling et al. claim that for a lattice spacing in UF_4 of 4.3 angstroms, a triply ionized pair of adjacent atoms will gain a kinetic energy of 10.2 eV as they recoil from one to three lattice spacings. The claim is, that in each collision of these recoiling atoms with neighboring atoms, the recoils will, on the average, transfer half of their energy per collision. They then calculate the time it takes a 1 eV U atom to travel one lattice spacing and find that this time is $t_{aa}=4.8\times10^{-13}$ sec. This is to be compared to $t_{hc}=1.3\times10^{-12}$ sec they get by calculating $t_{hc}=(r_0^2/4)(C\rho/\kappa)$ for UF_4. t_{hc} is the characteristic time one gets in solving the heat diffusion equation in cylindrical geometry starting from a line heat source. It represents the time scale on which heat conduction from a cylinder of radius r_o will occur in a solid with mass density ρ, heat capacity C, and thermal conductivity κ. Seiberling et al. argue that the U atoms have time to undergo several collisions, and create a region of local thermal equilibrium in the solid before heat conduction

quenches the hot region.

The assumption is, then, that local thermal equilibrium is established inside the cylinder by collisions of recoiling atoms. Target atoms evaporate through the surface of the taget until the hot spike is quenched by heat diffusing to the rest of the solid during a time t_{hc}. They assume that for $t<t_{hc}$, the atoms are in thermal equilibrium at some elevated temperature T. This implies that the atoms inside the cylinder have a Maxwell-Boltzmann velocity distribution given by

$$F(v)dv = n\left(\frac{M}{2\pi kT}\right)^{3/2} 4\pi v^2 \exp\left(-\frac{Mv^2}{2kT}\right)dv$$

where v is the magnitude of the velocity, n is the number density of the target particles, each of which has a mass M, k is Boltzmann's constant, and T is the equilibrium temperature of the cylinder.

Let v' be the velocity of the atom outside the target, and ϑ the angle between v'(vector) and the normal to the target surface. The flux of atoms sputtered into solid angle $d\Omega$ for a given $(v', v'+dv')$ is

$$\varphi(v',\Omega)dv'd\Omega = n\left(\frac{M}{2\pi kT}\right)^{3/2} \exp\left(-\frac{Mv'^2}{2kT}\right)\cos\vartheta v'^3 dv'd\Omega$$

The characteristic time for conducting heat from the hot region in a solid with mass density ρ, heat capacity C, thermal conductivity κ, and a hot spike of radius r_o is $t_{hc}=(C\rho r_o^2/4\kappa)=(r_o^2/4K)$. K is the thermal diffusivity $\kappa/C\rho$.

The number of atoms sputtered into solid angle $d\Omega$ and ϑ with velocity (v, dv) is found by multiplying the sputtered flux $\varphi(v',\Omega)$ by t_{hc} and the cross sectional area of the hot cylinder. This gives $S(v,\Omega)dvd\Omega$ equal to

$$S(v,\Omega)dvd\Omega = \varphi(v,\Omega)(\pi r_o^2)\left[\frac{r_o^2}{4K}\right]dvd\Omega$$

The total sputtering yield S is given by

$$S=\int\int S(v,\Omega)dvd\Omega = n\left[\frac{\pi r_o^4}{4K}\right]\left[\frac{kT}{2\pi M}\right]^{1/2}\exp\left[-\frac{E_b}{kT}\right]$$

The temperature and radius of the spike are expected to depend on the primary ionization rate dJ/dx. Seiberling et al. derive an energy per atom in the spike, E_o , due to the incident ion

$$E_o \propto \left[\frac{dJ/dx}{r_o}\right]^2$$

which gives for the spike temperature, T,

$$kT = D\left[\frac{dJ/dx}{r_o}\right]^2 + kT_o$$

where D is a constant and T_o is the ambient target temperature.

It remains to calculate the dependence of r_o on dJ/dx. They consider two cases.

In case I they assume that the spike temperature is independent of dJ/dx and that the spike radius expands or contracts to accomodate changes in dJ/dx. They argue that this would hold if the spike temperature were determined only by physical and chemical properties of the target. In this case, the sputtering yield has the following functional form

$$S \propto \left[\frac{dJ}{dx}\right]^4$$

In case II they assume that the spike radius is determined by properties

of the target, while the spike temperature varies as $(dJ/dx)^2$. Here they get for S,

$$S \propto \frac{dJ}{dx}\exp\left[-\frac{E_b r_o^2}{D(dJ/dx)^2}\right]$$

where D is a normalization factor for dJ/dx and E_b is the surface binding energy of the target.

That neither of these extreme cases holds exactly is provided by subsequent work in which UF_4 was sputtered by 13 MeV ^{35}Cl ions. Again the energy spectrum had the Maxwell-Boltzman form, but with T=5240°K. (Seiberling et al. 1981) dJ/dx has increased by a factor of 2, but T has increased only by $\sim(dJ/dx)^{\frac{1}{2}}$.

A potential problem with this model is that the electrons removed from the ions along the path of the incident ion are required to leave the vicinity of the track, and remain trapped until the ions have had a chance to respond to their mutual Coulomb repulsion. The holes left behind by the incident ion must remain near the track long enough for the ions to recoil at least one lattice spacing (see below). Another difficulty is that very little is known about the primary ionization rate, dJ/dx. This makes it difficult to distinguish between models on the basis of experimental results.

4. Other possibilities

The models mentioned above require that following ionization by the incident ion, the electrons and ions remain spatially separated for the duration of the sputtering event. C.C. Watson (1981) points out that this may be unreasonable. He argues that if the spike radius is indeed on the order of ~20 angstroms, the energy deposited into the electronic system

is enough to elevate one e^- on every atom in this region by several eV. With a region of highly excited electrons, it is not clear why some of these excited electrons do not migrate toward the ions along the initial track. This causes the holes left by the incident ion to migrate away from each other to the walls of the cylinder. Watson is proposing a model in which charge separation is not crucial. He treats the electronic excitations as a Fermi gas at elevated temperature. Clearly, as the electronic states of the solid are excited, the potential field seen by the solid atoms is altered from the equilibrium state of the undisturbed lattice. He proposes that the atoms of the solid gain kinetic energy by responding to this change in potential. This idea is attractive because it removes specific restrictions, such as long-lived, immobile ionic states. There are, however, no numerical results available yet. These ideas are similar to ones proposed by Van Vechten (1980a, 1980b) to explain certain phenomena seen in laser annealing.

Two final models which will be mentioned briefly here, and discussed in more detail in chapter V are an electron plasma desorption model suggested by Krueger (1977), and a thermal pulse model suggested by Sigmund and Claussen (1980).

Krueger proposes a model in which molecular ions are polar bound to the surface of the solid. The fast heavy ion induces polarization in the electron plasma which breaks these polar bonds and induces desorption of the molecular ion. This mechanism is capable of desorbing large molecular ions without exciting their internal degrees of freedom.

The thermal pulse model of Sigmund and Claussen predicts the formation of a hot spike region in the solid after passage of the high energy ion. Atoms of the solid are evaporated from this hot spike. Their

expression for the sputtering yield, Y, says that $Y \propto F_D^2$ where F_D is related to dE/dx. By making some further assumptions (see chapter V), one gets the result that $Y \propto (dE/dx)^2$ for a thermal model.

E. Applications of High Energy Sputtering in Dielectrics

We mention here that the results of these high energy sputtering yields are of interest in certain applications. Most notably, so far, are areas of astrophysics where it is desirable to know sputtering yields from high energy bombardment of frozen gas surfaces (Tombrello 1981, Haff et al. 1981, Lanzerotti et al.1978b, et al.1979, et al. 1978, Draine 1977, Johnson et al. 1981, Lanzerotti et al. 1978a), and in biophysics, where high energy sputtering has been used to desorb large biomolecules nondestructively (Macfarlane et al. 1976b, Hakansson et al. 1981a, 1981b, 1981c, Duck et al. 1980a, 1980b, Furstenau et al. 1977). These, and other, applications will be discussed in chapter VI.

II. Experimental Apparatus

A. General Requirements and Description of Apparatus

The experiments described in this thesis were designed to investigate the sputtering of frozen water ice by high energy ion beams.

Ice targets were prepared and sputtered in an ultra-high vacuum (UHV) chamber with a base pressure of 1×10^{-9} torr. Water ice was vapor deposited onto a cold Be target substrate located at the center of the chamber. After target formation, the pressure was typically $1-2 \times 10^{-9}$ torr. The ice was sputtered with ^{19}F beams at energies ranging from 1.6 MeV to 25 MeV. These energies were chosen to include regions on either side of the peak of the electronic stopping power for F in H_2O ice. Ice thicknesses before and after sputtering were measured by Rutherford backscattering of 1.5MeV ^4He particles.

The Be substrate for ice target formation was mounted at the tip of a liquid He transfer line. Target temperature was adjustable from 4.2 to 300°K. A cold (~20 to 30°K) copper radiation shield attached to the cold finger shielded the target from the 300°K chamber walls. During target formation, water vapor was directed onto the cold Be substrate through a differentially pumped target formation line.

Much care was taken in the collimation and integration of the analysis and sputtering beams. Both beams were Rutherford backscattered at 180° into an annular surface barrier detector. The number of sputtered water molecules was calculated using backscattering spectra from the He analysis runs. Charge integration of the sputtering beam was a particular problem for targets exhibiting high sputtering yields. To solve this problem backscattering spectra accumulated during the sputtering runs were used to calculate the number of ^{19}F particles

incident on the target.

B. Hardware

1. Beams

During each run, a ^{19}F beam was used for sputtering, and a ^{4}He beam was used to measure ice thicknesses before and after sputtering. The high energy ^{19}F beams were obtained from the negative ion duoplasmatron source on the HVEC 6MeV EN tandem accelerator in Kellogg Lab. Energies and charge states were chosen using an Alpha Scientific, Inc. Model 3193 NMR Gaussmeter at the 90° magnet downstream of the high energy end of the tandem. Energy selection is reported to be good to a few keV. When a higher charge state than that produced in normal operation of the accelerator was desired, a foil stripper was used just upstream of the 90° magnet.

The analysis beam used to profile the target before and after sputtering was always a 1.5MeV ^{4}He beam. These beams were obtained from the 1.5MeV JN van de Graff. Positive beams were extracted from the RF oscillator source of the JN, and neutralized before injection into the tandem. Once inside the tandem tank, the particles were stripped at the terminal and energy selected at the 90° magnet.

After energy selection, the beams were deflected by a switching magnet into a diffusion pumped beam line with a base pressure of approximately 2×10^{-7} torr. The beam line was equipped with a magnetic quadrupole for focusing, and magnetic deflectors for steering the beam. Finally the beam passed into the experimental chamber. The 10^{-9} torr vacuum in the chamber was isolated from the relatively poor vacuum in the beam line by an in-line cold trap which consisted of a 1cm I.D. diameter tube, 40 cm long, held at liquid nitrogen temperatures (see figure 2a).

Once delivered to the experimental chamber, the beams had to be collimated in order to sputter and measure well defined spots on the ice target. Before describing the beam collimation procedure, some time should be spent describing the vacuum chamber and target related apparatus.

2. Experimental chamber

The experimental vacuum chamber was a 6" diameter stainless steel UHV chamber with several access ports sealed by Conflat flanges with OFHC copper gaskets. It was equipped with an Ion Equipment Corp. Model COV-500 combination titanium sublimation pump (500 l/sec pumping speed for N_2) and 25 l/sec noble ion pump. In order to avoid contamination of the target surface with titanium, the sublimation pump was never used. All valves associated with the chamber were UHV stainless steel metal-sealed valves. The chamber pressure was read using an Ion Equipment Corp. Model PS-150 ion pump power supply (see figure 2b).

3. Cold finger

An open cycle liquid He transfer line extended through one of the large ports in the chamber. The Be target substrate was mounted on the tip of the cold finger, which positioned the Be at the center of the chamber. The transfer line was an Air Products and Chemicals, Inc. Model Lt-3B-110 HELI-TRAN (referred to hereafter as the cold finger; see figure 2c). The target and cold finger were cooled by flowing liquid He from a dewar, through the center of an evacuated transfer line, onto the tip of the cold finger. He flow was achieved by pressurizing the dewar with He gas at 5 to 10 psi. This pressure had to be maintained throughout the entire run in order to achieve temperature stability at the target. Upon reaching the target end of the cold finger, the He flowed back, in

gaseous form, along the space between the walls and inner tube of the cold finger. Part of the cold He gas was vented into the atmosphere at the far end of the cold finger (outside the vacuum; see figure 2d). A thermostatically controlled heater kept this end of the transfer line from freezing up. The rest of the cold returning He gas flowed back, as a cooling counter flow, along the walls of the vacuum jacket surrounding the center tube of the liquid He transfer line.

Liquid He flow to the target was controlled by two methods. One was to adjust the needle valve through which liquid He flowed onto the tip of the cold finger. The other was to adjust the amount of flow through the transfer line either by restricting the vent gas outlets, or by adjusting the He gas pressure at the dewar.

A given temperature, at the target, was achieved by flowing He onto the cold tip, and simultaneously introducing a heat flow to the cold tip. The heat was supplied by a resistance heater located near the target end of the cold finger. The heater was constructed for operation in ultra-high vacuum. It consisted of a 1"O.D., 5/8" long, pyrex tube which had slots perpendicular to its axis. Resistance wire (25 Ω/ft) was wrapped helically around the slots in the pyrex tube. The pyrex tube was coupled to the cold finger through a copper shim which was corrugated and pressed tightly between the tube and the cold finger. The total resistance of the heater was ~55Ω. The heater was used not only to provide control of the target temperature, but also to return the cold finger to room temperature at the end of a run (see figure 2e).

Temperature at the target end of the cold finger was measured using a calibrated thermocouple [Au(.07% Fe) vs Chromel (APC); reference junction 273.2 ° K] supplied by Air Products and Chemicals, Inc. (see

figure 2f). The thermocouple was soldered into the target end of the cold finger with an indium alloy solder. Measured values for the thermocouple voltage at room temperature (~295° K) and at ~4.2°K were +.000475V and ~-.005210V. In comparison, the calibration data for +.000475V and -.005210V are, respectively, 292°K and 10°K.

Both the heater and thermocouple wires were brought out along the length of the cold finger through a mini-conflat electrical feedthrough located at the warm end. The wires were electrically isolated with pyrex beads. Current to the resistance heater was supplied by a 0-40V DC, 0-1 amp Lambda Electronics Corp. Model LPD 422FM regulated power supply. A John Fluke MFG Co. Model 885AB DC differential voltmeter was used to monitor the voltage across the thermocouple (see figure 2c).

4. Target assembly and target electron suppression system

The target assembly was located on the end of the cold finger. It consisted of a threaded OFHC copper block screwed into the copper end of the cold finger. For good thermal contact, an acid etched indium gasket was compressed between the acid etched copper mating surfaces of the cold tip and the copper block. The copper block extended past the center of the chamber. It served as a heat sink for the Be target substrate, and positioned the target such that the center of the Be disk coincided with the line of direction of the beam. The surface of the copper block which faced the beam was angled so that its normal was 30° from the direction defined by the beam. This angled surface had three threaded holes through which to anchor the Be substrate. This substrate was a 1/16" by 3/4" disk of Be (98% pure by weight-supplied by L.A. Gauge Co, Inc.) A thin layer of Au (~7.9μg cm^{-2})was evaporated onto the surface of the Be to provide a heavy marker for the backscattering runs. The Be

disk was electrically isolated, but thermally coupled to the copper block by a 3/4" by 1/16" quartz disk. Acid etched indium gaskets compressed between the acid etched surfaces of the copper, quartz, and Be provided thermal contact at the copper-quartz and Be quartz interfaces.

The target assembly was a stack consisting of; copper block, indium, quartz, indium, Be (see figure 2e). A small stainless steel plate was put as a final layer on top of this stack. The plate had a large central hole to admit the beam, and clearance holes for insulated stainless steel screws which mated with the threaded holes in the copper block. Tightening these screws held the target stack in place, and compressed the indium gaskets for good thermal contact. Beam was integrated directly off the stainless steel plate which was in electrical contact with the Be-Au surface. The beam integration wire was brought out along the cold finger, and through a mini-conflat electrical feedthrough located at the warm end.

During normal running conditions, the target assembly was the coldest surface in the chamber. A 1 1/2" O.D. copper radiation shield, in thermal contact with the cold finger, surrounded the target to shield it from contaminants, and from the surrounding room temperature chamber walls. It enclosed the target entirely, except for apertures to let the beam in, backscattered particles out, and H_2O vapor in during target formation. With liquid He flowing, and the tip heater off, the radiation shield was about 20° warmer than the target (see figure 2e).

To provide the secondary and tertiary electron suppression necessary for accurate integration of high energy heavy ion beams, the target was surrounded by a ~1 1/4" O.D. copper wire suppression cage. It was estimated to be ~95% transmitting to backscattered beam particles and

electrons. Care was taken to ensure that no direct beam could come into contact with the cage. The cage was supported on insulating ceramic rings which slip fit inside the radiation shield. It was biased to large negative voltages, typically -2000V, during the runs (see figure 2e).

5. Heat loads on the cold finger, beam heating of the target

With a liquid He flow rate of 0.7 liters per hour, the refrigeration capacity of the cold finger was 500 mwatts at 4.2° K, 3 watts at 20° K, and 7 watts at 50° K. This capacity was adjustable from 0 to 250% by changing the He flow rate.

Consider first the heat deposited by the sputtering beam in the Be target substrate. A typical sputtering beam was a few particle nanoamps of 15MeV ^{19}F . This represented a power load of

$$(5\times10^{-9}C/sec)(e/1.6\times10^{-19}C)(15\times10^{6}eV)=4.69\times10^{17}eV/sec$$

$$(4.69\times10^{17}eV/sec)(1.6\times10^{-19}J/eV)=.075watts$$

Other heat loads to the cold finger were introduced by the wires running from the room temperature mini-conflat feedthroughs to the target end of the cold finger. The tip heater, cage bias, and beam integration wires were all made of constantan, which has a low thermal conductivity. The thermocouple wires were Fe doped Au and chromel. The estimated heat load due to conduction through these wires was ~75 mwatts. An estimate for the heat load on the cold finger due to radiation is less than 10 mwatts.

A typical liquid He consumption rate was ~1 l/hr. At this flow rate the refrigeration capacity of the cold finger was in excess of 500 mwatts, which was adequate to handle these heat loads.

It is of interest to know whether the heat conductivity through the quartz disk was adequate to handle the thermal load introduced to the Be by the sputtering beam. It is estimated that with the copper target block at ~10°K , and a beam depositing ~75 mwatts into the Be disk, the temperature rise at the Be across the fused quartz disk was on the order of 2–4°K.

6. Target formation line

Ice targets were formed by directing water vapor (or any other gas) through a target formation line onto the cold Be substrate.

The far end of the line was a pyrex vessel filled with water and water vapor in equilibrium (17.54 torr for 20° C). Rough flow control was provided by a leak valve which restricted access to the rest of the line. Between the water vessel and the chamber was a line leading to a mechanical roughing pump. A final valve isolated the line from the UHV chamber. When this valve was opened, water vapor flowed into the chamber through a 1/4" copper tube. The tip of the copper tube was ~3/4" from the Be disk, and pointed normal to the Be-Au surface. The water vessel and roughing pump could each be independently valved off (see figures 2g and 2h).

The roughing pump was separated from the line by a copper coil which, during target formation, was immersed in liquid nitrogen. The purpose of the roughing pump was to evacuate the line before the valve to the water vessel was opened, and to reduce the pressure of the water vapor in the line during target formation. The coil provided some pumping action of its own, and isolated the pump oils from the water vapor.

The target formation line was made of stainless steel, pyrex, and Kovar parts welded together or coupled with copper gasket Cajon fittings.

There was one Viton O-ring in the needle valve.

After the UHV isolation valve, entry into the chamber was made through a 1/4" stainless steel tube welded into the conflat flange bolted to the chamber. Inside the chamber, the stainless steel tube was joined to the twisted copper line, used to direct water vapor onto the Be, by a stainless steel Swagelok connection. The copper tube was equipped with a ~45Ω heater to be used in the event that ice accumulated inside the tip of the copper tube. This heater was similar to the one used on the cold finger. It consisted of a resistance wire wrapped around a pyrex tube, and coupled to the line with copper shim. The electrical leads for this heater were brought out through an electrical feedthrough bolted to one of the access ports on the chamber (see figure 2g).

The rest of this chapter deals with the collimation and integration of the beam, detection of backscattered particles, and the processing of signals produced by the surface barrier detector.

7. Detector

The detector used to measure the backscattered beams was located close to the chamber wall between the beam line and the target (see figure 2g). It was an Ortec TC-017-100-100 annular surface barrier detector with ~ 100 pF capacitance. The +50V detector bias was supplied by an Ortec Model 210 0-1000V power supply, which was also used to monitor the detector's leakage current. The detector had a 100mm sensitive surface area, and a depletion depth of 100 μm. A depletion depth of 100 μm was quite adequate to handle the beams in question here. The ranges in Si of 1.5 MeV He and 2MeV/amu ^{16}O are, respectively, 4 μm (according to a data sheet from EG&G Ortec) and 20 μm (data quoted in the Ortec Silicon Charged Particle Radiation Detectors Instruction Manual). The ranges of

the F sputtering beams were similar to that quoted for the O beam.

8. Beam collimation and integration

The detector was supported by an aluminum holder, which in turn, was attached to a Huntington Model VF-172-2 UHV vernier manipulator feedthrough with 2" vertical motion. The collimators used to define the beam and suppress electron production were also attached to this aluminum holder (see figure 2i).

There were basically two configurations of detector and collimators which the beam could have encountered upon entering the chamber. One was with the 2" manipulator positioned such that beam passed through the annular detector on its way to the target. The other was with the 2" manipulator raised to such a position that beam passed through a set of collimators below below the aluminum target holder (see figure 2j).

First examine the situation where the beam passed through the detector. In this configuration, beam could be scattered at 180° from several spots on a single ice target by moving the detector up and down in the vertical line of the beam (see figure 2j).

Upon entering the vacuum chamber, the beam first encountered an electrically isolated collimator with a hole 0.041" in diameter. This collimator was a 0.010" thick tantalum sheet mounted on the back of the aluminum detector holder, and positively biased at +300V to suppress electron production. Beam falling on this aperture could be sent to a current integrator.

The collimated beam then passed through a 0.020" thick, 0.080" diameter Ta collimator mounted directly on the grounded casing of the detector. It travelled next through a thin walled stainless steel (.081" I.D.) tube mounted through the hole in the annular detector. This tube

protected the back side of the Si wafer from scattered beam. It also provided support for a collimator mounted in front of the detector used to block backscattered beam from reaching the ragged edges of the detector's sensitive Au layer, where incomplete charge collection could occur. This collimator and the tube were both grounded to the detector's casing. Another larger collimator, also located in front of the detector shielded the outer ragged edge of the sensitive Au layer, and the epoxy layer of the Si wafer, from backscattered particles. These two collimators defined the solid angle subtended by the detector in the backscattered beam. The smaller of the two (see figure 2j) was a 0.200" O.D. stainless steel hat with a hole to let beam through. The larger one was a 0.010" Ta collimator with a .377" hole. These collimators sat ~1/8" in front of the sensitive surface of the detector, and 2.055 ±~.060" from the target surface. For particles backscattered from the target, they defined a solid angle of 1.90×10^{-2} sr which was accurate to ~10%.

Now consider the configuration in which the detector was moved up out of the way, so that beam passed below the aluminum holder and never through the detector (see figure 2i). This configuration had the advantage that beam never travelled through the 0.081" I.D. tube extending through the hole in the detector. This tube could cause electron production problems if the beam was slightly misaligned. This second configuration provided a useful cross check on the beam integration procedure.

After entering the chamber, the beam first passed through an electrically isolated collimator with a 0.062" by 0.161", biased at +300V (part of the same +300V collimator mentioned above). The collimated and suppressed beam then travelled directly between the pole faces of a

small 750-800 Gauss horseshoe magnet. The purpose of this magnet was to deflect any electrons travelling through the aperture with the beam. The beam then passed through another Ta aperture located on the side of the aluminum holder which faced the target. This aperture was a .010" thick Ta sheet with a 1/4" x 1/4" hole. It was also electrically isolated and was usually biased at -600V. Any scattered beam could be read off this aperture to a current integrator. The -600V turned back any electrons deflected toward the target by the horseshoe magnet.

Electrical connections to these collimators and to the detector were made using bare copper wire, indium solder, crimp connections, and pyrex beads. The wires were connected to an electrical feedthrough bolted to the top flange of the chamber (see figure 2g).

In order to minimize the production of scattered beam by the collimator system, the collimators and UHV chamber were aligned with a telescope mounted at the switching magnet of the accelerator. This ensured that beam that had passed through the center of the beam line quadrupole magnets would be aligned properly with respect to the collimators in the UHV system. Furthermore, beam that had passed through the collimators would fall on the center line of the Be-Au target, after passing symmetrically through the aperture in the radiation shield. Note that the hole in the radiation shield (0.5" by 1.25") was elongated in the vertical direction so that as the beam was steered vertically to go through the collimators, backscattered beam into the detector's solid angle had a clear path from the target to the detector at all times.

Sputtering measurements were made by depositing an ice target, measuring several spots on the ice target, sputtering several of these measured spots, and then scanning the whole target with the analysis

beam to measure the remaining ice. While it was desirable to have motion of the detector in the vertical direction, it was necessary to keep the horizontal position of the detector fixed as rigidly as possible. A 1/4" stainless steel ball bushing was attached to the side of the aluminum detector holder. As the detector was moved up and down during the sputtering and measurement runs, this ball bushing ran up and down along a 1/4" stainless steel rod fixed relative (and perpendicular) to the top flange of the chamber (see figure 2i). To avoid uncertainties, due to backlash, in repositioning the manipulator between sputtering and analysis runs, the manipulator was always turned down below the desired value, and brought back up into position.

9. Electronics

Since the experimental chamber was at ultra high vacuum, care had to be taken in making a shielded coaxial cable to transmit the output signal of the detector. Pulses from the detector travelled through a bare, copper wire. One end of the wire was crimp connected to a Au plated pin compatible with the detector's output connector. The other end of the wire was attached to an electrical feedthrough on the top of the chamber. The signal wire was electrically shielded along its entire length by a grounded copper braid sheath. Pyrex beads strung along the central wire insulated it from the copper braid. As signal travelled through the pin of the electrical feedthrough, it was electrically shielded by the chamber walls. Finally, connection to the preamplifier was made outside the vacuum by connecting the signal pin of the electrical feedthrough to the input of the preamplifier with a 93Ω/ft coaxial cable. The grounded sheath of this cable connected the ground of the preamplifier casing to a second pin on the electrical feedthrough. Inside the vacuum, this pin was

attached directly to the detector's casing.

The signal from the detector was fed to a Canberra 808 charge-sensitive preamplifier. The input impedance of the preamplifier was lowered to 1.14 MΩ to minimize the voltage drop due to rather large leakage currents from the detector(~.2μA) The signal was then fed to one of two amplifiers, both Canberra 2010's. One was used to amplify the signal from backscattered He particles, the other for backscattered F particles. At the beginning of every run, the gain, pole zero, variable threshold, and DC level adjustments on each of the amplifiers were made. A 1-2 μsec shaping constant, and symmetric, medium restorer settings were chosen to give the best resolution for Si detectors at the typical count rates we used (usually well below 1 kHz). The unipolar output signal from the Canberra 2010 was fed to the DC coupled input of a Nuclear Data, Inc GEN II 100 MHz ADC. The ADC signal was then fed to a Nuclear Data ND4420 MCA with a video display. The bipolar output pulses from the 2010 were monitored with an oscilloscope during the run.

It was essential that the gain of the amplifier system remain constant throughout the run. Gain stability was monitored by feeding a pulser signal into the test input of the Canberra 808. Pulses for this purpose were obtained from a Berkeley Nucleonics Corp. Model BNC DB-2 pulser. The resolution of the pulser peak was approximately a factor of two worse than it should have been. The noise, however, was Gaussian, and therefore not expected to have any effect on the backscattered peak centroids.

This same pulser was used to check the linearity of the system. A cross check on linearity was run by backscattering ^{4}He particles of 1.0, 1.5, and 2.0 MeV energy from the Be-Au surface and observing the

position of the backscattered Au peak.

The detector had a .5 μsec time constant. The 808 accepted a charge pulse from the semiconductor detector and produced an output pulse ±4V with a rise time of .150 μsec, and a fall time of 50 μsec. The Canberra 2010 accepted ±12V, with a rise time less than or equal to the shaping time constant (in our case 1-2 μsec). Its output unipolar pulses were ±10V maximum Gaussian pulses, with time to peak of 2.2 x 2 μsec. The ADC accepted 0 to +8V DC pulses with rise times greater than 0.2 μsec.

During the runs, the beam current impinging on the Be-Au target (biased at +300V) was fed to a Brookhaven Nuclear Instr. Model 1000 current integrator. Digital pulses from the Brookhaven integrator were sent to two destinations. The first was a homemade (Mann 1975) preset charge collector. Accumulation of a spectrum was begun by starting the preset collector as beam was put on target. When a given preset charge had accumulated on target, the ADC was gated from accepting any more pulses. At this time, beam was taken off the target. The second destination for the digital output pulses from the Brookhaven current integrator was to the input of a pair of master-slave Tennelec TC 550P scalers. These scalers were used to moniter the dead time of the ADC in the following sense. The master and slave scalers received pulses from the digital output of the Brookhaven. The master was gated by the preset charge collector. Therefore, digital pulses were counted in both scalers from the start of a run until the preset charge was reached. The slave scaler was also gated by the busy output of the ADC. The total number of counts in the two scalers were used to calculate the fraction of time that the ADC was busy during accumulation of a spectrum. Typical differences between the two scalers were on the order of 1%. A general schematic of the

electronics used to accumulate spectra is shown in figure 2k.

III. Experimental Procedure

This chapter describes the procedure used to measure and calculate the sputtering yields of frozen ice targets bombarded with high energy ^{19}F beams. The chapter is divided into two parts. Section A describes the experimental procedure used to acquire backscattering spectra with the ^{19}F and ^{4}He beams. Section B describes how to calculate the sputtering yields from these spectra.

A. Measurements

The sequence of measurements made in a typical run will be outlined first. This will be followed by a more detailed account of particular aspects of the measurement procedure.

The first step in any run was to cool the target down to liquid He temperatures and apply operating biases to the detector, collimators, suppression cage, and target. Using a tail pulse generator, varying amplitude pulses introduced at the test input of the preamplifier were sent through each of the two amplifiers to check linearity. The pulse amplitudes were chosen to cover the same range of pulse amplitudes produced by the beams.

A collimated beam of ^{19}F was then scattered at 180° from four spots on the bare target. These spots were spaced at 0.100" intervals. Following these runs, the detector was raised to its uppermost position so that the beam passed through the lower set of collimators and scattered back up into the detector (see figure 2j). The backscattering angles subtended by the detector in this latter position ranged from 145° to 163°. A 1.5 MeV ^{4}He beam was then obtained and scattered from the bare target using the same manipulator settings as the F beam. Recall that the bare target was a thick disk of Be with a thin Au marker evaporated onto its surface.

The purpose of these bare target runs was to measure the number of particles backscattered from the Au layer for a given preset charge. These numbers were used later to calculate charge collected on target during the sputtering runs, and to check the beam integration procedure. The positions of the Be edge and Au peaks from these bare target spectra were used to calculate the energy calibration of the amplifier system. A pulser peak of fixed amplitude was recorded in these and all subsequent spectra. Its position was monitered to check gain stability.

The detector was repositioned so that beam incident on target passed through the hole in the annular detector (see figure 2j). Beams of 1.0, 1.5, and 2.0 MeV ^{4}He were scattered at 180° from the bare Be-Au target. The position of the Au peak was used as a second check (in addition to the pulser method) on system linearity.

At this point bias was removed from the detector and an ice target was formed. Details on this procedure will be given later.

When the vacuum in the experimental chamber recovered after ice target formation, bias was again applied to the detector. The 1.5MeV ^{4}He beam was scattered at 180° from seven spots on the ice target which were spaced at 0.050" intervals. Four of these spots coincided with the locations of the bare target He spectra. Ice thicknesses were calculated by comparing these two sets of spectra. These four spots were also the same target locations used in the sputtering runs. The other three ice target measurements were spaced to fall evenly between the four sputtering locations. These intermediate spots were used later to monitor stability of the unsputtered ice layer in the vacuum chamber. One measurement of the ice target was made with the detector in its uppermost position. This spectrum was used later to cross-check the beam

integration procedure.

Before the sputtering runs, the target temperature was brought to the desired value by adjusting the flow of liquid He to the tip, and, if necessary, simultaneously introducing heat from the resistance heater described in chapter II. During the sputtering runs, one at each of the four spots mentioned above, a predetermined number of F particles were deposited on the ice target.

If the target temperature had been changed for the sputtering runs it was now returned to liquid He temperature. The 1.5MeV ^{4}He beam was brought back to measure the same seven spots as those measured on the fresh ice target. Four of these spectra were used to calculate the amount of ice removed during the sputtering runs. The other three were used to calculate how much ice, if any, had been deposited or sublimed from the unsputtered part of the target.

After finishing the measurements, detector bias was removed, and the target temperature returned to $\geq 273^{\circ}$ using the tip heater.

It is now necessary to give a more detailed account of parts of this experimental procedure. Consider first the formation of the ice layer. Ice films were deposited in a fairly reproducible way using the following procedure. The target substrate was lowered to $\sim 10^{\circ}$ K. A roughing pump (isolated by a LN_2 coil) was used to evacuate the water line and water vessel (see figure 2h). The leak valve was opened fully and the fore pump allowed to pump on the liquid H_2O for 10 min. At this time, the leak valve was adjusted to a nearly closed position. Finally, the ice layer was deposited by opening the valve isolating the water line from the UHV chamber for a time on the order of 70 sec. During this time pressure in the chamber rose to $\sim 85\mu a$ ($\sim 2.5 \times 10^{-7}$). Upon closing the isolation valve, the

pressure dropped almost immediately to <10μa, and was down to <1μa (~1 $\times 10^{-9}$torr) within a few minutes. (Pressure in torr ~3×10^{-8} $\times$ current in ion pump.)

One method of calculating the sputtering yield relied on knowing the absolute areas of the peaks formed when 1.5MeV He scattered from the ice layer. This required that the number of ^{4}He particles impinging on the target during the analysis runs be accurately known. Since this was a particularly difficult problem, some time will be spent describing the procedure here.

Recall that the detector holder supported two distinct sets of collimators (see figure IIi). In one configuration (see chapter 2, section B-8, also see figure 2j). beam passed first through a 0.041" diameter Ta collimator, biased to +300V. The maximum energy which can be transferred in a head on collision, with mass M at energy E incident on mass m, is (4m/M)E. For a ^{19}F ion incident on an electron, this maximum transferred energy is 1.15×10^{-5} E. Therefore, a 20MeV ^{19}F could transfer up to a few hundred eV to a target electron. It was assumed that +300V was sufficient to trap most of these electrons produced when beam struck the Ta collimator.

The beam next encountered a grounded 0.080" collimator and a 0.081" I.D. tube extending through the detector. If this collimator and tube were properly aligned with the first collimator, beam scattered at the 0.041" aperture was blocked by the 0.080" aperture, and well collimated beam passed through the 0.080" aperture and tube without scattering or producing any electrons. There was, however, the possibility that some high energy e^- had escaped the +300V bias and travelled down to the target with the beam. Any such e^- would presumably be

turned away by the -2000V bias on the target suppression cage (see figure 2j). Once the beam struck the target, it produced secondary e^-, and backscattered ions and neutrals. The e^- were largely trapped by the voltage drop of +2300V from the cage to the target. Some of the high energy backscattered ions and neutrals, however, were able to reach the radiation shield and chamber walls where they produced tertiary e^-. (Matteson et al. 1979) The -2000V bias on the suppression cage prevented these e^- from returning to the positively biased target.

Suppose, now, that the .041" collimator was not well aligned with the .080" collimator and tube, and beam was able to strike to walls of the tube were it could make e^-. Recall that by using the second configuration of collimators, beam could reach the target without ever having to pass through the detector (see figures 2i and 2j).

In this configuration, the beam first encountered a +300V, 0.062" by 0.161" collimator. Again, the +300V was to trap secondary e^- produced by the beam. The beam then travelled directly between the pole faces of a 750-800 Gauss horseshoe magnet. Any e^- that had escaped the +300V were deflected by this magnetic field (the radius of curvature of the trajectory of a 1 keV e^- in a 750 gauss field is 0.14 cm). Finally, the beam passed through a 0.250" by 0.250" collimator biased at -600V. Presumably, any e^- deflected towards the target by the B field were stopped by this -600V. The integration of the beam upon reaching the target was the same for this configuration of collimators as for the first one.

Even with the precautions taken to integrate the beams accurately, this technique could not be relied upon to be accurate during the sputtering runs with high energy ^{19}F. Additional problems arose because of very high sputtering yields. As many as 1500 H_2O molecules were

removed per incident beam particle. If 1% of the sputtered particles were positively ionized, 15 positive ions would leave the target for every F that arrived. Furthermore, these positive ions would have been accelerated by the +300V on the target and the -2000V on the cage. If any of these ions, or sputtered neutrals, struck the suppression cage itself and produced e^-, these e^- would have been collected back on the target. These problems ruled out the possibility of using a standard current integrator. For the sputtering runs, integrated doses of F particles were calculated from the number of ^{19}F ions backscattered from the Au on the target.

Another problem arose during the final 1.5MeV ^4He analysis runs. To make these measurements, the detector had to be positioned precisely over the sputtered crater on the ice target. Uncertainties associated with moving the detector meant that the ice target was not always being measured at the same spot where it had been sputtered. One contribution to this problem was backlash in the 2" vertical motion feedthrough. To minimize this effect, the detector was always lowered to a point below the desired position, and then raised back up to the correct position. This did not, however, remove the problem entirely. There were still occasional unexplained shifts in the detector's position. This made it necessary to scan the analysis beam across the vicinity of each of the sputtered spots on the target. Recall that the aperture defining the beam was 0.041". For the analysis of a given spot, the detector was lowered ~0.015" below the expected location of the sputtered crater. Sequential analysis runs were taken raising the detector .005" each time. The number of runs taken was determined by the shape of the sputtered spot. It was evident from the backscattering spectra which runs

corresponded to the location of the sputtered crater. These runs were used in calculating the sputtering yields.

B. Analysis

All measurements of ice thicknesses, before and after sputtering, were made by scattering He beams from the ice target. Therefore, no information was obtained on the molecular structure of the sputtered material. It was assumed in the following outline of the data analysis that H and O were removed stoichiometrically from the target. The validity of this assumption will be discussed further in chapter IV.

Before outlining the analysis of the data, a brief review of Rutherford backscattering will be given. (Chu et al. 1978) The laboratory differential scattering cross section, $d\sigma/d\Omega$, is given by

$$\frac{d\sigma}{d\Omega} = \left\{\frac{Z_1 Z_2 e^2}{4E}\right\}^2 \frac{4}{\sin^4\Theta} \frac{\{[1-((M_1/M_2)\sin\Theta)^2]^{1/2} + \cos\Theta\}^2}{[1-((M_1/M_2)\sin\Theta)^2]^{1/2}}$$

where

Z_1 = atomic number of the projectile

M_1 = atomic mass of the projectile

Z_2 = atomic number of the target atom

M_2 = atomic mass of the target atom

e = charge on the electron = 4.8×10^{-10} esu

Θ = laboratory scattering angle

E = energy of the projectile immediately before scattering

For $M_1 << M_2$

$$\frac{d\sigma}{d\Omega} \approx \left\{\frac{Z_1 Z_2 e^2}{4E}\right\}^2 [\sin^{-4}(\Theta/2) - 2(M_1/M_2)^2 + \ldots]$$

Another useful quantity is the kinematic factor $K=E'/E$ where E is the projectile energy immediately before scattering, and E' is the projectile energy immediately after scattering.

$$K = \left\{ \frac{[1 - (M_1/M_2)^2 \sin^2\Theta]^{1/2} + (M_1/M_2)\cos\Theta}{1 + (M_1/M_2)} \right\}^2$$

For $\Theta = 180°$

$$K(180°) = \left[\frac{M_1 - M_2}{M_2 + M_2}\right]^2$$

For experimental conditions in which a uniform beam impinges at normal incidence on a uniform target that is larger than the area of the beam

$$A = \sigma \Omega Q Nt$$

where

A = the total number of detected particles

σ = $(1/\Omega) \int_\Omega (d\sigma/d\Omega)\, d\Omega$

Q = total number of incident particles

Nt = number of target atoms per unit area

for small Ω, $\sigma \rightarrow d\sigma/d\Omega$

There are two independent ways to calculate the sputtering yield from the spectra obtained by backscattering 1.5MeV ^{4}He from the ice target before and after the sputtering runs. One is to monitor the position of the Au centroid, which will vary as a function of ice thickness. The other is to monitor the number of counts in the O peak. In order to calculate these yields, several quantities of interest must be extracted from

the data (see figure 3a).

The position of the Au peak will depend on the energy calibration of the backscattering spectrum, β = keV/channel. The value of β is determined using the position of the Au centroid from the bare target runs, and the leading edge of the thick O peak from the fresh ice target runs. Possible sources of error in these numbers arise from the difficulty of finding the edge or centroid of a peak from a target which is not quite a thick target, and not exactly a delta function (see chapter IV, section C-12).

$$\beta = \frac{[\,K(He-Au) - K(He-O)\,]\,E(He)}{ch(AuC) - ch(Oedge)} \quad \frac{keV}{ch}$$

where

$E(He)$ = incident energy of the He beam

$K(He-Au)$= kinematic factor for scattering He from Au at 180°

$K(He-O)$= kinematic factor for scattering He from O at 180°

$ch(AuC)$= channel number of Au centroid

$ch(Oedge)$= channel number of the half height of the high energy edge of the O peak

Another way to calculate β is to use the spectra obtained from scattering 1.0, 1.5, and 2.0 MeV ^{4}He from the Be-Au target.

$$\beta = \frac{E_1K(He-Au) - E_2K(He-Au)}{ch_1(AuC) - ch_2(AuC)}$$

where

E_1, E_2 = energy of incident ^{4}He

$K(He-Au)$= kinematic factor for backscattering He from Au at 180°

$ch_1(AuC), ch_2(AuC)$= channel number of Au centroid obtained by scattering E_1, E_2 He from Au.

Another quantity of interest for the analysis is the effective stopping power for backscattering ^{4}He particles from the Au layer through a thin film of ice. The formula used here is referred to by Chu et al. (1978) as the "thin film approximation". In chapter IV, section C-4, the validity of using this approximation will be discussed.

$$E_{out\,1} = [\, E_{in\,1} - (dE/dx)_{Ein}\, \delta_1]K - (dE/dx)_{KE}\, \delta_1$$

$$E_{out\,2} = [\, E_{in\,2} - (dE/dx)_{Ein}\, \delta_2]K - (dE/dx)_{KE}\, \delta_2$$

where

δ_1 = thickness of initial ice layer

δ_2 = thickness of final ice layer

K = kinematic factor for scattering He from Au at 180°

$E_{in\,1}=E_{in\,2}$= incident energy of He

$E_{out\,1}$ = energy of He after scattering from the Au through an ice layer of thickness δ_1

$E_{out\,2}$ = energy of He after scattering from the Au through an ice layer of thickness δ_2

$(dE/dx)_{Ea}$= stopping power for ^{4}He of energy E_a in H_2O

The effective stopping power, ε, for He backscattering from Au through a thin ice layer is given by

$$\varepsilon = (E_{out\,2} - E_{out\,1})/(\delta_2 - \delta_1)$$

$$\varepsilon = -(dE/dx)_{Ein} K - (dE/dx)_{KE}$$

Since the sputtering yield is defined as $(\#H_2O\ removed/\#F\ incident)$, the number of F incident on the target during the sputtering run must be calculated. If the beam integration was done correctly, accurate Au peak areas were are obtained upon scattering a known number of F atoms Q_{bare} (measured using the current integrator) from the bare Be-Au target. Then the integrated dose of F, Q_{sputt}, accumulated during the sputtering runs, may be calculated using the formula

$$Q_{sputt} = \frac{(\sum Au)_{sputt}\ Q_{bare}}{(\sum Au)_{bare}\ q} \frac{1}{\alpha}$$

where

$(\Sigma Au)_{sputt}$ = area of the peak from scattering ^{19}F at 180° from the ice covered Au target

$(\Sigma Au)_{bare}$ = area of the peak from scattering ^{19}F at 180° from the bare Au target

Q_{bare} = integrated ^{19}F charge deposited on the bare Au target, measured using the current integrator

q = charge state of the incident ^{19}F on the bare Au layer

α represents the correction to the peak area caused by the change in $d\sigma/d\Omega$ as the F lost energy passing through the ice layer. This quantity is approximated by

$$\alpha = \frac{1}{2}\left\{\left[\frac{E}{E_1}\right]^2 + \left[\frac{E}{E_2}\right]^2\right\}$$

where

E = energy of incident ^{19}F beam

E_1 = energy of ^{19}F after passing through initial ice thickness δ_1

E_2 = energy of ^{19}F after passing through the final ice thickness after sputtering, δ_2

and

$$E_1 = E - (dE/dx)_F \delta_1$$

$$E_2 = E - (dE/dx)_F \delta_2$$

$(dE/dx)_F$ is the stopping power of ^{19}F at energy E in ice. Peak areas, (ΣAu) and (ΣO), are calculated from the backscattering spectra by

$$A = \left[\sum_b^c n_i\right] - \tfrac{1}{2}\left[c_1 \sum_a^{b-1} n_i + c_2 \sum_{c+1}^{d} n_i\right]$$

The standard deviation, σ, is given by

$$\sigma = \left[\sum_b^c n_i + \frac{1}{4}\left[c_1^2 \sum_a^{b-1} n_i + c_2^2 \sum_{c+1}^{d} n_i\right]\right]^{\frac{1}{2}}$$

where

n_i = number of counts in channel i

b, c = channel numbers bracketing peak

$a, b-1$ = channel numbers bracketing background below peak

$c+1, d$ = channel numbers bracketing background above peak

c_1 = $(c-b)/(b-1-a)$

$c_2 = (c-b)/(d-c-1)$

Now the formulae for calculating the sputtering yields may be written down. First, using the position of the Au centroid (see figure 3a, also, see Appendix A)

$$S = \frac{(\Delta AuC)\,(\beta)\,(1/\varepsilon)\,(A)}{(Q_{sputt}/q)\,(1/e)}$$

ΔAuC = shift in Au centroid before and after sputtering, channels

β = energy calibration, eV/ch

$1/\varepsilon$ = 10^{15} (H_2O/ cm^2)/111 eV

A = area of beam defining collimators, cm^2

Q_{sputt} = integrated charge of ^{19}F during sputtering, Coulombs

q = charge state of ^{19}F used in sputtering

e = electronic charge = 1.6×10^{-19} Coulombs

The biggest uncertainty in this method is the accuracy with which dE/dx for He in H_2O ice is known. This problem is discussed in chapter IV, section C-2.

The second method for calculating the sputtering yield is to compare the areas of the O peaks from the ice layers before and after sputtering (see figure 3a). For this calculation, it is necessary to relate the O peak areas to ice thicknesses. See figure j for spectra before and after sputtering runs and with the bare target.

$$\frac{(Nt)_O}{(\sum O)} = \frac{1}{(d\sigma/d\Omega)_O\,\Omega\,Q}$$

where

$(Nt)_O$ = #O atoms / cm^2 in the ice layer

(ΣO) = peak area of He scattered from the O in the ice layer

$(d\sigma/d\Omega)_O$= partial differential cross section for 180° scattering of He from O, cm^2 /sr

Ω = solid angle of detection

Q = integrated charge of $^4He^+$

Then the sputtering yield, S, is given by

$$S = \frac{(\Delta\sum O)\,(Nt_O)/\sum O)\,(A)}{(Q_{sputt}/q)\,(1/e)}$$

$(\Delta\Sigma O)$ = change in area of O peak before and after sputtering

$(Nt_O/\Sigma O)$= # H_2O/ cm^2

A = area of sputtering beam collimators, cm^2

Q_{sputt} = integrated charge of ^{19}F sputtering beam

q = charge state of ^{19}F used in sputtering

e = electronic charge = 1.6×10^{-19} Coulombs

The biggest uncertainty in this technique is that it is difficult to know the solid angle, Ω, of the detector accurately. The detector's acceptance area is large, and the detector is relatively close to the target. An estimate of the errors made in calculating Ω will be given in chapter IV, section C-9.

IV. Experimental Results

The results of several experiments designed to measure the sputtering yields of frozen water ice by ^{19}F beams are presented in this chapter. The discussion is divided into four sections. In section A, general considerations pertaining to all of the experiments are discussed. The sputtering yield of ice with ^{19}F beams was measured as a function of the beam energy, incident charge state, beam current density, substrate temperature, and target thickness. In section B, the data are presented in such a way as to show how the yields vary as a function of these parameters. One measurement of the sputtering of ice by 1.5 MeV ^4He was taken. This result is also presented in section B. Care was taken to account for sources of error in both the execution of the experiment and the analysis of the results. These problems are discussed in section C. Finally, section D briefly presents results of other experiments which are important to consider in comparison and contrast with the ^{19}F on H_2O (solid) results. All of the sections will refer to table A, which is a general presentation of the results and experimental parameters of the F on ice sputtering runs.

A. General Experimental Results

An important step in all of the experiments was the formation of the ice targets. Typical ice layers were $\sim 6\times10^{17}$ H_2O/cm^2 (~1800 angstroms). Typical deposition rates were $\sim 8.7\times10^{15}$ H_2O/cm^2sec = 9.4×10^{-4} g/cm^2hr. According to Olander and Rice (1972), water vapor deposited at temperatures below 55°K and at rates $\leq 10^{-2} g/cm^2hr$, will form amorphous ice layers.

The thirteen different ice targets used in these experiments were measured to determine their thicknesses. A profile of any individual ice

film showed that it was not uniform across the surface of the Be-Au disk where the sputtering measurements were made. Typical thicknesses were found to range from $5.2\times10^{17} H_2O/cm^2$ at the lowest detector position, to $6.8\times10^{17} H_2O/cm^2$ at the uppermost position. The variation in thickness was about 25% of the average depth across the film (see figure 4a).

B. Results of ^{19}F and ^{4}He Erosion Measurements of H_2O(solid) Films

The sputtering yields of ice films were measured as a function of several experimental parameters. This section is divided into six parts, each of which shows the dependence of S on a given parameter.

1. Sputtering yield vs ^{19}F incident energy

These experiments on the sputtering of ice were undertaken, in large part, to investigate the role of the electronic stopping power on ion beam sputtering of insulating targets. In a series of experiments, the energy of the ^{19}F beam was varied across a wide enough range of energies to incorporate the maximum possible variation of the electronic stopping power for ^{19}F in H_2O (solid). The energies chosen for the ^{19}F beams were 1.6, 5.0, 6.0, 7.5, 10.0, 15.0, 20.0, and 25.0 MeV. The sputtering yields measured in these experiments are given in figure 4b. Also shown in the figure is a curve of dE/dx for ^{19}F on H_2O solid which was obtained from the Zeigler (1980) compilation of heavy ion stopping powers.

The incident charge states of the F beams used for these runs were, in order, +2, +2, +3, +3, +3, +4, +4, and +5. These particular charge states were chosen since they were readily available in normal operation of the tandem. The relationship of these charge states to the equilibrium charge states of ^{19}F on H_2O (Ziegler 1980) is shown in figure 4c.

At any given energy, the points shown in figure 4b represent the mean value of all the measurements taken with a given set of

experimental parameters. The error bars indicate experimental reproducibility. Let S_{avg} be the mean of a set of individual sputtering measurements, S_i. If N is the number of measurements taken,

$$S_{avg} = \frac{1}{N}\Sigma S_i \pm \left[\frac{1}{N-1}\Sigma(S_i - S_{avg})^2\right]^{1/2}$$

Recall that in any given experiment, S is calculated by two different methods described in chapter III (monitoring the position of a gold marker, and summing the counts in the oxygen peak). The values of S obtained by these two methods are shown separately in figure 4b. Comments on why they differ from one another are given in section C of this chapter.

S_{avg} was obtained for each energy by averaging the runs listed in table A as follows: 1.6 MeV (a), 5.0 MeV (b), 6.0 MeV (c), 7.5 MeV (d), 10.0 MeV (e,g, first two of i--.760 .860 first two of h--.760 .860), 15.0 MeV (j), 20.0 MeV (first two of k--.760 .860), 25.0 MeV (l).

2. Sputtering yield vs incident charge state of the F ions

The sputtering yields were measured as a function of the incident charge state of the F beam for a given energy. As a means of comparison, we calculated the equilibrium charge state of the F ions in H_2O(solid) for the same energy. Figure 4c shows this calculation of equilibrium charge states (see section C-2 of this chapter). The solid curve is calculated from a formula given by Ziegler (1980).

The charge states for the runs listed in part 1 above are all well below this equilibrium curve. There were three runs in which the F charge state was increased to a value that exceeded the equilibrium value. These were at 10.0 MeV (+3, +4, +6), 20.0 MeV (+4, +8), and 25.0 MeV (+5, +8). The

two +8 runs at 20.0 MeV are lower limits on the sputtering yield. The analysis runs on these points showed that the ice was completely eroded away from parts of the Be-Au target surface.

The data, including charge state information, are plotted in figure 4d which is identical to 4b except that the variations in charge states of the F beam are included. Also shown in this plot are the equilibrium charge states (taken from the solid curve in figure 4c) at each ^{19}F energy used in the sputtering runs.

3. Sputtering yield vs substrate temperature

The sputtering yield was measured as a function of the substrate temperature. This was done, as described in chapter II, by introducing a heat flow to the cold tip using a resistance heater. The heat flow was balanced with the liquid He flow to achieve a given temperature, which was monitored using the thermocouple, also mentioned in chapter II.

All of the temperature dependent runs were done with 10.0 MeV $^{19}F^{+8}$ at 2-3 na of current. The results are shown in figure 4e. There seems to be no significant effect up to ~60°K. There are no error bars shown because each of the points was only taken once. The points shown are from runs f and h of table A. A run was attempted at 78°K, but there were problems with the analysis runs because the sputtered crater was not a well defined spot. The center seemed to be spread out over a much larger area than expected, which may have been due to the elevated temperature of the substrate, or to an unidentified experimental problem. This point is not shown in figure 4e because we do not understand the result yet.

Since all of our other data were taken at temperatures well below 60°K, these results indicate that there will be a negligible effect on the

data from small temperature differences.

4. Sputtering yield vs beam current intensity

In several of the sets of sputtering runs, the beam current density was varied to determine whether the target was being macroscopically heated by the F beam. Beam current densities ranged from 0.15 - 4.7 particle nanoamps/mm^2 where the term particle nanoamps is defined by (beam current in nanoamps)/(charge state of the incident ion). The beam currents used are listed in table A.

The data show no convincing evidence of a beam current heating effect over the range of current densities chosen. Only run g (see table A) shows a noticeable effect, the magnitude of which is comparable to the standard deviation of the data.

5. Sputtering yield vs ice thickness

As has been mentioned in section A of this chapter (see figure 4a), the ice layers deposited on the Be-Au substrate were not of uniform depth across their width. The magnitude of the effect was about 25% of the total thickness of the ice layer. There are no significant trends in the data which would indicate that there is a dependence of S from a 25% variation in the initial ice layer thickness.

There were two sets of measurements taken at the same F energy and charge state, but for an initial ice thickness that differed by a factor of ~2 (see run g in table A, to be compared with run e).

For an average initial ice thickness of 67.77×10^{16} H_2O/cm^2, run e gives S(AuC) = 978 (σ=191), S(Σ O) = 904 (σ = 183), and run g gives S(AuC) = 888 (σ=116), S(ΣO)= 777 (σ = 170) for an average initial ice thickness of 28.98×10^{16} H_2O/cm^2. Within the reproducibility of the measurements, no

significant effect can be claimed.

6. Measurement of 1.5 MeV ^{4}He sputtering of H_2O

Upon completion of the F sputtering measurements in run f (see table A), we measured the sputtering yield of the ice at detector position .910 with 1.5MeV ^{4}He ions. The sputtering beam current was 8 na. The yield measured by the gold centroid method was 8.1, and with the oxygen peak method, 9.1.

C. Analysis of Uncertainties

There were many potential sources of error to be considered, both in the execution and analysis of the experiments. These will be discussed in some detail in this section. Most of them turned out to be insignificant at the level of 10% or better. The data were actually very reproducible. Our experimental reproducibility was usually well below ±10% (see section 16).

1. Stability of ice films

One obvious potential source of error in the experiment is instability of the ice film in the vacuum chamber. One must consider the rate of deposition of material from the vacuum onto the ice surface, and the rate of loss, due to sublimation, from the ice surface to the vacuum.

The base pressure in the chamber was $\sim 1\times10^{-9}$ torr or lower during the course of the runs. This pressure was achieved upon cooling the cold finger to liquid He temperatures. Using the ideal gas law, one can calculate the time required for monolayer formation at these pressures. According to Roth (1976), at 10^{-9} torr this time is ~ 1 hr. The pressure in the immediate vicinity of the target is probably less than this because of the radiation shield surrounding the ice target (see chapter II). Only particles with a direct line of sight to the target are able to condense out on

its surface. Consider the worst case, however, where the monolayer formation time is one hour. If the elapsed time between ice deposition and the final analysis runs is 10 hr, 10 monolayers will have deposited on the target surface from the vacuum. This would correspond to a shift of approximately 0.5 channels of the gold centroid. Typical shifts due to sputtering were on the order of 10-15 channels, with reproducibility of a few tenths of a channel. Therefore, deposition from the vacuum of $\sim 10^{-9}$ torr is a small effect (<<5%).

Now consider the question of sublimation of the ice film in the vacuum. The rate of sublimation, $\varphi_{th} = H_2O/cm^2sec$, was calculated using (Kelly 1979)

$$\varphi_{th} = \alpha p \frac{1}{(2\pi m k T)^{1/2}}$$

α = 1= sticking coefficient

p = equilibrium vapor pressure

m = $3.01 \times 10^{-23} g$

T = $^{\circ}K$

k = $1.381 \times 10^{-6} erg/^{\circ}K$

The vapor pressure curve for H_2O was obtained from Roth (1976).

The results of a calculation of φ_{th} vs T is given in table B. To get an idea of the effect of sublimation on the ice films, assume that the target was raised to 90°K for 10 hr. At 90°K, $\varphi_{th} = 0.122\ H_2O/cm^2sec$. The loss of H_2O from the area of the analysis beam ($8.33 \times 10^{-3} cm^2$) is $(0.122\ H_2O/cm^2sec)(3.6 \times 10^4\ sec)(8.33 \times 10^{-3}\ cm^2) = 37\ H_2O$. For a sputtering yield of 200 and a F dose of 2×10^{12}, the loss of H_2O over the same area, due to sputtering, would be $(200\ H_2O)(2 \times 10^{12} F) = 4 \times 10^{14}\ H_2O$. Clearly, according

to these calculations, sublimation of the ice film at these temperatures is not a problem. All of the sputtering experiments were performed at temperatures well below 90°*K*. Most of the measurements were made at 10°*K*. Even during the temperature dependent runs, all analysis was done ~10°*K*. The target temperature was elevated only for the actual sputtering runs, which lasted approximately one hour.

During the course of every experiment, unsputtered spots on the target were monitered to keep track of ice stability experimentally. Typical shifts of the gold centroids at the unsputtered spots were on the order of 1-5% of the centroid shift measured due to sputtering, which confirms our estimates that buildup and sublimation are unimportant in these experiments.

2. Electronic stopping power of F in H_2O, He in H_2O

Two curves which are crucial in the analysis of the data and interpretation of the results are the electronic stopping power, dE/dx, of ^{19}F and ^{4}He in H_2O. Finding reliable curves for the quantities has proved to be something of a problem.

First consider the stopping of ^{4}He in H_2O. There are several compilations of stopping power data in the literature. In figure 4f, five of these curves are shown. The crosses are taken from Northcliffe and Schilling (1970) where data are given explicitly for He incident on H_2O. Two of the other curves are calculated from the Ziegler compilation of He stopping power data (Ziegler 1977). These latter curves in figure 4f are calculated using Bragg's rule on data for gas and solid H and O targets bombarded with He beams. The other two curves in figure 4f are from experimental data for He on H_2O ice and vapor given by Matteson et al. (1977). The value of dE/dx used in analyzing the data were taken from the Matteson

curve for solid H_2O. These values differ by ~ 10% from the values of dE/dx on H_2O(solid) calculated using the Ziegler tables.

One might try to compare compilations of stopping power data with theoretical calculations. However, the physics of energy loss at intermediate energies (.2 MeV-3MeV He) is very complicated. At higher energies, the impulse approximation calculations predict stopping cross sections to within a few percent. For very low energies, the adiabatic approximation has been applied with varied success. In the region where ion velocities are similar to orbital electron velocities (near the peak of the electronic stopping power ~0.5MeV/amu), the physics of the stopping power problem is less simple to approximate in calculations.

Another problem in using dE/dx tables arises when one is required to use Bragg's rule to compute the energy loss in a material composed of several different elements. (Bragg's rule says that the stopping power of a compound A_nC_m is equal to, $dE/dx(A_nC_m) = n[dE/dx(A)] + m[dE/dx(B)]$ where dE/dx is expressed in units of $eV/H_2O/cm^2$). According to Chu et al. (1978), for high velocity protons ($v >> v_o$, the velocity of the electron in a Bohr orbit), Bragg's rule is valid to 1%. For 1-2 MeV He, while Bragg's rule gives good agreement in metallic alloys and compounds, departures on the order of 10% arise in using Bragg's rule on oxides, and nitrides, or other compounds in which one element is gaseous in elemental form where dE/dx is measured (Ziegler et al. 1975). Gas solid differences are higher for low Z elements than high Z ones.

The Ziegler compilations have drawn together all existing measurements of dE/dx in various elements. Where data are not available, extrapolations from nearby values of Z were performed. Ziegler and coworkers first calculated master stopping curves valid for all ions in a single target

element. They constructed master effective charge curves by least squares fitting to fractional effective charges of nearest neighbors which had experimentally determined stopping powers. The procedure was done independently for two different theoretical models (local oscillator model, free-electron gas model). These results were compared with experimental data. The effective charge was calculated, using both H and He experimentally determined data for its evaluation. The stopping power was then calculated from these effective charge curves (Ziegler 1977).

Ziegler (1977) and coworkers calculated master stopping curves for ion energies between 10 keV - 10 MeV for gas and solid targets separately. They caution that for low atomic number targets we cannot expect these values to be very accurate. It has been shown by Matteson et al. (1976) that various forms of solid carbon can have quite different stopping powers. A further caution is that while separate curves for solid and gaseous O targets are shown, the predicted solid curve is expected to be less accurate than the gaseous O_2 experimental curve (Ziegler 1977). All of these points must be remembered when calculating dE/dx for H_2O from H and O (solid) curves.

The problem of determining dE/dx for heavy ions is also not a simple problem. Figure 4g shows two different curves of ^{19}F on H_2O (Northcliffe et al. 1970, Ziegler 1980). Again, Ziegler (1980) and coworkers use theoretical models to calculate the stopping cross sections. Effective charges are calculated by comparing theoretical curves to actual experimental ion stopping data. They use the following formula to calculate the equilibrium charge states, $Z_{HI}^{\bullet}$, of heavy ions with energy E, mass M, in matter. $Z_H^{\bullet}$ is the equilibrium charge state of a proton at the same

velocity (Ziegler 1980).

$$\frac{Z_{HI}^{*}}{Z_{H}^{*}} = 1 - e^{-A}\left[1.034 - .1777exp\left(-.08114Z_{1}\right)\right]$$

$$A = B + .0378\sin(\pi B/2)$$

$$B = \frac{.886\left(E/\left(25M_{1}^{1/2}\right)\right)}{Z_{1}^{2/3}}$$

where E is in keV, and M_1 is amu. This equation is considered to be good to 5% for ions with Z=6-92 in solids with Z=4-79 for E >0.2 MeV/amu.

$$Z_{H}^{*} = 1 - \exp-\left[0.2\left(\frac{E}{M_1}\right)^{1/2} + .0012\left(\frac{E}{M_1}\right) 1.443\times10^{-5}\left(\frac{E}{M_1}\right)^{2}\right]$$

where E is in keV and M_1 is in amu.

The curve obtained by applying Bragg's rule to Ziegler's stopping curves for F on H (solid) and O (solid) is the one used in the analysis and interpretation of the data.

3. Angular acceptance of the detector

The collimators placed in front of the detector define the solid angle into which the beam is scattered (see chapter II). Because of the inner collimator and hole through the annular detector, none of the beam is scattered exactly at 180°. However, suppose it is assumed that all beam scatters at 180°. The most widely deflected particles which can scatter into the detector are at 174.7°. In order to estimate the errors made by assuming 180° deflection, compare the Rutherford differential scattering cross sections for these two angles.

$$\frac{d\sigma}{d\Omega} = 14.37\times10^{-24} cm^{2}/sr$$

for 1.5 MeV He on Au scattered at 180°.

$$\frac{d\sigma}{d\Omega} = 14.43\times10^{-24} cm^2/sr$$

for 1.5 MeV He on Au scattered at 174.7°. These differ by 0.4%.

$$\frac{d\sigma}{d\Omega} = 0.1290\times10^{-24} cm^2/sr$$

for 1.5MeV He on O scattered at 180°

$$\frac{d\sigma}{d\Omega} = 0.1297\times10^{-24} cm^2/sr$$

for 1.5MeV He on O scattered at 174.7°. These differ by 0.5%. Thus the approximation of 180° scattering is a good one.

4. Validity of the thin film approximation

The thin film approximation (Chu et al. 1978) is only valid for small enough ice film thicknesses (see chapter III) such that dE/dx is essentially constant during the entire passage of the ion through the ice. This requires that $(dE/dx)\ \delta << E_{initial}$, where δ is the thickness of the ice layer, and $E_{initial}$ is the energy of the incident beam.

To see if this is true, assume an ice thickness of 60×10^{16} H_2O/cm^2. Use the value of dE/dx for He on H_2O obtained from Matteson (1976) experimental values. Recall that in calculating the effective stopping power, ε, for the thin film approximation (see chapter III), the energy of the He beam going into the ice layer was assumed to be 1.5 MeV, and after scattering from the gold marker, this energy was assumed to be constant at 1.383 MeV (the incident energy of the beam times the kinematic factor for He scattering from gold at 180°). dE/dx (1.5MeV He on H_2O)= 56.8 eV/ $10^{15}H_2O/cm^2$. The He ion loses 34 keV passing through

such an ice film. dE/dx for 1.466 MeV He on H_2O is approximately 57.2 This is an 0.7% change from the value of dE/dx at 1.5 MeV. For 1.383 MeV He, dE/dx in H_2O is 58.5 eV/ $10^{15}H_2O/cm^2$. Going through the ice layer, the He loses 35 keV. dE/dx for 1.348 MeV He on H_2O is about 59. This is an 0.8% change. This tells us that the thin film approximation is a very good approximation for ice films of the thicknesses we have used in these experiments.

5. Deviations from Rutherford scattering of 1.5 MeV He on oxygen

The assumption was made, in analyzing the data, that the cross section for scattering 1.5MeV ^4He at 180° from oxygen was purely Rutherford. This was checked by scattering ^4He at energies of 1.3, 1.4, 1.5, 1.6, and 1.7 MeV at 180° from an ice film. If the scattering is indeed Rutherford, the area of the oxygen peaks should scale as $1/E^2$. The results of these runs are shown in figure 4h. Deviations from a straight line are on the order of a few percent, thus there is no evidence of deviations from Coulomb scattering.

6. The contribution to sputtering by the He analysis beam

The sputtering yield of 1.5 MeV ^4He was measured, and found to be S(AuC)=8.1 , and S(ΣO)=9.1. During a typical analysis run, the He dose on target was 3.75×10^{12} He. This represents a total number of H_2O removed of (8.1) $\times(3.75\times10^{12})=3.04\times10^{13}$ H_2O. These were removed from the area of the analysis beam which was 0.85 mm^2. The removed layer is then $3.04\times10^{13}H_2O/0.85mm^2 = 3.58\times10^{13}H_2O/mm^2 = 3.58\times10^{15}H_2O/cm^2$. This represents a shift in the gold centroid of approximately 0.4keV which corresponds to a shift of 0.2 channels. Typical shifts due to F sputtering were one the order of 15 channels. Thus, even when the sputtered crater was scanned by several analysis beams, the contribution to sputtering by

the He analysis beam was fairly small.

7. Statistical uncertainties

The formula for calculating the error and standard deviation of the peak areas was given in chapter II.

$$A = \sum_{c}^{b} n_i - \tfrac{1}{2}\left[c_1 \sum_{a}^{b-1} n_i + c_2 \sum_{c+1}^{d} n_i\right]$$

where n_i is the number of counts in channel i of the spectrum. The first term in this equation represents the number of counts in the peak between channels b and c. The second and third term are the low and high energy backgrounds summed between channels a and (b-1), and (c+1) and d. The constants c_1 and c_2 weight the backgrounds according to the width of the spectrum over which the backgrounds were measured. [$c_1=(c-b)/(b-1-a)$, and $c_2=(c-b)/(d-c-1)$] The standard deviation of the peak area, A, is given by σ.

$$\sigma = \left[\sum_{b}^{c} n_i + \frac{1}{4}\left(c_1^2 \sum_{a}^{b-1} n_i + c_2^2 \sum_{c+1}^{d} n_i\right)\right]^{\frac{1}{2}}$$

Typical ice layers in the runs before and after sputtering have 2000-8000 counts in the oxygen peak. Backgrounds vary from 300 to 900 counts. This means that σ is a few percent of the area of the peak, which is much smaller than the experimental reproducibility in measuring the area of a given peak.

The quantity we have been referring to as the centroid of the gold peak is also known as the mean of the peak. Statistically the uncertainty in the mean is (Bevington 1969)

$$\sigma_\mu = \frac{\sigma}{N^{\frac{1}{2}}}$$

where

σ_μ = uncertainty of the mean

σ = standard deviation in the mean

N = total number of counts in the peak

There are corrections to this calculation when background subtractions are required. The number of counts in the backgrounds around the gold peak are 2-3% of the area of the peak. To estimate uncertainties in the mean, we will ignore background corrections.

The standard deviation σ is equal to $\Gamma/2.354$ where Γ is the full width at half maximun of the peak. The gold peak typically had ~30,000 counts. Γ was in some cases as large as 50 channels. This gives a maximum value of σ = 21 channels. Therefore, σ_μ =0.12 channels. This, again, is much smaller than the experimental reproducibility in measuring the gold centroid position, which was on the order of 0.5-1 channel. We do not understand the source of this irreproducibility. However, a 0.5-1 channel shift represents less that 5% of the typical shifts of the gold marker during the sputtering runs.

8. Beam related problems

We must know the beam energy for the analysis of the results of the scattering experiments. The accuracy with which the energy of the He beam is known, as determined by the tandem accelerator, is ~ 1 keV. Since the energies of the beams were all on the order of 1-10 MeV, we are not concerned with a ~1keV uncertainty.

Another point to check is whether or not we are heating the target by putting too much beam on target during the sputtering runs. Macroscopic heating of the target by the beam is presumably not occurring

since for some of the sputtering runs the current density was increased by a factor of 4-6 with no significant increase in the sputtering yield. We would expect the sputtering yield to increase with an increase in temperature of the ice film if the sputtering were due to evaporation.

9. Solid angle of detection

The area between the collimators defining the angular acceptance of the detector may be calculated fairly accurately since these collimators are easily measured. This area is $0.518 cm^2$. It is a more difficult problem to know the distance from the target to these collimators accurately (~2.055"). The solid angle is estimated to be 1.90×10^{-2} sr. However, an error of 1/16" in the distance of the detector from the target (which is not an unreasonable error in this number) changes the value of the solid angle by 6%. The calculated sputtering yield is proportional to $1/\Omega$.

10. Check on the beam integration

As has been mentioned in chapters II and III, integration of the beam was something of a problem.

The first step in the beam integration procedure was to scatter 3.75×10^{12} He particles (1.5MeV) from the gold marker with no ice on target. The gold was deposited by evaporation onto the Be target. According to the quartz oscillator used during the evaporation, the gold layer was $2.41 \times 10^{16} Au/cm^2$ (a number which is probably accurate to about 5%). Since the Be disk was oriented at 30° from the direction of the beam, this number must be divided by 0.866 to give the thickness of the gold seen by the beam. This number is $2.78 \times 10^{16} Au/cm^2$. Using the differential scattering cross section for He on Au at 180° , and the calculated solid angle of detection, the number of counts expected in the gold peak may be calculated. This number was then compared to the areas of the Au

peaks found experimentally. The experimental values vary around the expected value, the typical deviations being a fraction of a percent up to ~ 3%. Using the area of the gold peak from the bare target, the area expected upon scattering ^{19}F from this target may be calculated. This was compared to the areas found by scattering the ^{19}F sputtering beam from the bare target at 180°. The difference between the expected and experimental areas in a few cases was as high as 10 %, but was usually 3% or better.

A further check on the beam integration was performed after the deposition of the ice layer. The ice thickness was measured using the shift in the gold centroid, or the number of counts in the oxygen peak for He scattered at 180° from the O in the H_2O layer. The detector was then moved up so that the He beam passed through the lower set of collimators(see chapter II). This method had the advantage that, at no time, did the He beam pass through the annular surface barrier detector. Furthermore, this lower set of collimators had magnetic as well as electronic suppression for secondary electrons. In this position, beam scattered from the ice target at angles ranging from 145°–163° up into the detector. For a given integrated dose of He (3.75×10^{12} He), the area expected in the oxygen peak could be calculated and compared to the number obtained experimentally. This method is less reliable than the one using the gold peak because of the larger aperture through which the He beam passed (.062" × .161"). This meant that the beam sampled an uneven ice layer, and that the angle of deflection into the detector varied depending on where the He actually passed through the collimator. The differential scattering cross section for He on O is $15.02\times10^{-24}cm^2/sr$ at 163°, and $17.37\times10^{-24}cm^2/sr$ at 145°. These differ by ~15%. However, when

this beam integration check was performed, the difference between the calculated and experimental oxyen peaks was usually ~ 5-12%, with one run at 16%. We estimate that the beam integration was accurate, in most cases, to better than 5%.

11. The effect of the ice thickness on determining Q and Σ O

As has been discussed above and in chapter III, the ^{19}F sputtering beam was integrated by scattering the F at 180° from the Au peak during the sputtering run. The size of this peak was then compared to the gold peak obtained by scattering F from the bare Be-Au target. In making this comparison, one must remember that during the sputtering run, the F is losing energy in the ice layer before it scatters from the gold marker, which degrades the energy of the F particles. (Also, during the sputtering runs, the thickness of the ice layer was continually decreasing) This energy loss must be taken into account when calculating the integrated charge of the sputtering beam. As described in chapter II, the following approximation was made to account for this effect. First the initial ice thickness before sputtering, and the final ice thickness after sputtering, were calculated. Using dE/dx, the energy loss of the F beam in the ice layer was calculated. By subtracting these energy losses from the intial energy of the F beam, one obtains the quantities $E_{initial}$ and E_{final}, which are the energies of the F beam immediately before scattering from the gold after having passed through the initial and final ice layers. The changes in the Rutherford differential scattering cross sections, $d\sigma/d\Omega$, were then calculated by the $1/E^2$ dependence of $d\sigma/d\Omega$. For an incident F beam of energy E_{inc}, these ratios were $(E_{inc}/E_{initial})^2$ and $(E_{inc}/E_{final})^2$. These two ratios were averaged to give

$$\alpha = \tfrac{1}{2}\left[\left(\frac{E_{inc}}{E_{initial}}\right)^2 + \left(\frac{E_{inc}}{E_{final}}\right)^2\right]$$

The sputtering dose was found by

$$Q_{sputt} = \left[\Sigma Au(F)]_{sputt} \frac{Q_{bare}}{[\Sigma Au(F)]_{bare}}\right] \frac{1}{\alpha}$$

where $[\Sigma Au(F)]_{bare}$ is the sum in the gold peak after scattering Q_{bare} (collected charge measured by the current integrator) from the bare Be-Au target. $[\Sigma Au(F)]_{sputt}$ is the number of counts in the gold peak collected during the sputtering run(both at 180°). For the sputtering runs listed in table A, at 1.6MeV, α = 1.15, at 5.0MeV, α = 1.05, 6.0MeV, α=1.07, 7.5MeV, α = 1.06, 10.0MeV, α = 1.02-1.05, and 15.0, 20.0, and 25.0MeV, α = 1.02.

A similar effect must be considered in the measurement of the ice thicknesses before and after sputtering with the 1.5 MeV He beam scattered at 180°. As calculated in section 4, for an ice thickness of $60\times10^{16} H_2O/cm^2$, a 1.5MeV ^4He ion loses 34 keV passing through the ice layer. This changes $d\sigma/d\Omega$ for Rutherford scattering by a factor of $1/E^2$. $(1.500/1.466)^2 = 1.047$. If this is averaged with 1.000 which corresponds to scattering from the front surface of the H_2O target, the α factor is ~ 1.03. This was not corrected for in the analysis of the data.

12. Energy calibration of the system

The energy calibration of each spectrum was calculated by using three *reference points*: the position of the gold peak, the leading edge of the oxygen peak from the initial ice layer, and the leading edge of the Be signal.

The position of the gold peak was determined by taking the centroid of the peak obtained by scattering 1.5MeV He from the bare gold on the Be-Au target. According to Ziegler (1977), the energy loss of 1.5MeV ^4He in Au is $\sim 118 eV/10^{15} Au/cm^2$. The Au marker is $2.78\times10^{16} Au/cm^2$. The He

loses ~ 3 keV passing through the gold layer. The calibration for all the spectra was ~ 2 keV/ch. This means that, due to the energy loss of the He in the gold layer, the width of the gold peak may be 2-3 channels after scattering from the front and back surfaces of the gold marker. The leading edge of the Be was also affected by this same amount since the He passed through the gold before it scatters from the surface of the Be. The surface of the oxygen, however, was not covered by any other layers, so we may expect that the half height of the oxygen peak accurately revealed the energy of the 1.5MeV scattered from O. However, the He peaks scattered from the oxygen in the ice layers were usually not flat topped peaks, which made it difficult to accurately locate the half height of the leading edge of the O signal.

To estimate the errors introduced by these uncertainties, assume that the gold centroid was misplaced by 5 channels, certainly an overestimate of the real errors in the experiment. This would change the energy calibration by 1%. The differences between the calibrations calculated using different combinations of the gold centroid and oxygen and Be edges was again on the order of 1-2%.

13. Gain stability and dead time of the electronics

The measurement of the dead time of the ADC was described in chapter II. During the analysis runs these dead times were <1%. No correction was made for this effect. Also mentioned in chapter II was the fact that the gain of the amplifier system was monitored during all the runs by using a pulser signal of fixed amplitude. It was found that the stability of the system was not better than ≤ 1 channel. The cause of this instability is not known. Occasionally there were gain shifts on the order of several channels. When it could be determined that these shifts were

in fact due to gain changes, the data were corrected. This was determined not only by the position of the pulser peak in the spectrum, but also by the position of the leading edge of the oxygen peak on the target locations where no sputtering had occurred.

14. Determination of the profile of the sputtered crater

The technique used to measure and sputter the ice films required that the detector position be changed between the sputtering and analysis runs of a given spot on the target (see chapter III). As has been discussed, these were problems with positioning the detector accurately during the analysis runs so that the ice was being measured in precisely the same location as the location where the sputtering was done. To alleviate this problem, the ice was scanned with the .041" diameter analysis beam at .005" intervals. It is difficult to estimate the error made in conducting the analysis in this fashion. The peak shapes on the analysis runs are likely to be oddly shaped due to uneven ice layers from the sputtering run. It is assumed that the analysis run with the most displaced centroid represented the position of the sputtered crater. Typically there were two adjacent runs which seemed to be at the deepest point, with nearly equal gold centroid positions. This provides some evidence that the scanning was providing a good measure of the sputtered ice thickness.

Moving the analysis beam at .005" intervals meant that, at worst, the analysis beam could be displaced .0025" from the correct position to measure the crater This of course, assumed that there was no motion of the detector in the horizontal direction between the sputtering and analysis runs. As the detector was moved up and down, its horizontal alignment was kept constant by a stainless steel rod fixed to the top of

the chamber (see chapter II). We have assumed that the horizontal position of the detector was constant, although we have no way to scan the ice in this direction.

15. Discrepancy between the Σ O and gold centroid methods of determining the sputtering yields--stoichiometry

In most cases, the two methods of calculating the sputtering yields agree to within errors on the data points themselves. The agreement was fairly good for all the points except those at 7.5MeV and 10.0MeV. At 10.0MeV the errors on the points themselves are ~ 20% and the two determinations differ by 13%. At 7.5MeV, the errors on the points are about 4%, the two values differ by 18%. This irreproducibility is not understood.

By comparing the two values for S obtained from the gold centroid shift and oxygen sums, we should be able to say something about the stoichiometry of the sputtering. Suppose, for example, that H is preferentially removed from the ice film by the sputtering process. We would expect, then, that the gold centroid would begin to move before the number of counts in the oxygen peak began to change. If any such effect was occurring, it was not large enough to be seen with our present resolution.

It is true that in all but one case (5.0MeV), where there is a difference between the two S values, the gold centroid gives the larger value of S. This may indicate that the values of dE/dx we are using for He on H_2O are too small, the value of the solid angle we use in calculating S by ΣO is too large, or it could be a systematic experimental error as yet unidentified.

16. Experimental reproducibility

In all but one set of runs, the reproducibility was better than ±10%. For most of the runs it was better than ±10%. (Here we have defined the

reproducibility to be σ / S_{avg}). However, for the 10.0MeV runs, the reproducibility was as large as 18%. The reason for this is unknown.

17. Energy straggling of the beam

We must consider the effects of energy straggling on the spectra we took by scattering ^{4}He and ^{19}F from the ice targets.

To do this we use the expression for Bohr energy straggling for particles in the electronic stopping power regime (Chu et al 1978). This expression is derived by calculating the statistical variance in the number of collisions, with a given energy transfer, that an ion of charge Z_1 suffers travelling through a given depth, t, of the target.

For a compound target $A_m C_n$, this expression for Bohr straggling is

$$\Omega_B^2 = 4\pi(Z_1 e^2)^2 N^{A_m C_n}(mZ_A + nZ_C)t$$

where

Ω_B^2 = the square of the Bohr straggling = $(eV)^2$

Z_1 = atomic number of the projectile

e^2 = 14.4 eV angstroms

$N^{A_m C_n}$ = number density of molecules $A_m C_n$ in the target

Z_A = atomic number of element A of the target

Z_C = atomic number of element C of the target

t = target thickness in angstroms

For ^{4}He incident on H_2O (assume a density of 1gm/cm^2), N=3.32×10^{22} H_2O/cm^3), giving Ω_B^2=3.46×10^3 t $eV^2/Å$. For ^{19}F incident on H_2O, Ω_B^2=7.01×10^4$te V^2/Å$. For a typical ice layer of 1800 angstroms, this gives us Ω_B(He on H_2O) = 2.5 keV, and Ω_B(F on H_2O) = 11 keV. Since the straggling goes as the square root of the target thickness, for a target

sputtered halfway through, these numbers become 1.8 keV (for 900 angstroms), and 7.9 keV.

We must see whether energy straggling is a problem in the analysis of our results. For a He beam passing in and out of an 1800 angstrom ice layer, the spread in energy due to straggling is on the order of 1-2 channels in the backscattering spectrum. The width of the gold peaks are typically 15-20 channels, so energy straggling is not a major contribution to the energy resolution of the system. Also, the distribution obtained from straggling is Gaussian so that the centroids of the peaks should not be affected. The straggling widens the peak, but does not change the total number of counts in the peak, thus the sizes of the oxygen peaks should remain unchanged.

As for the F backscattered particles, at no time do we rely on the position of the F peak scattered from the gold marker. Rather, we care only about the number of counts in the peak, a number which we need to calculate the sputtering beam dose, Q_{sputt}. We are concerned whether the Rutherford cross section for 180° scattering of F from Au is changed significantly by energy straggling in the ice film. With an 11 keV spread in the beam energy, for 5 MeV F, this represents $(5.000/4.989)^2 = 1.004$ = 0.4% change in $d\sigma/d\Omega$. This is clearly not a problem.

18. Target angle

When we performed our sputtering experiments, the normal to the ice target was oriented 30° from the direction of the beam. This orientation was chosen so that the Be target substrate was perpendicular to the target formation line. This, of course, meant that an actual ice layer was (1800 angstroms) times cos30° = 1559 angstroms. Our analysis procedure is unaffected by the tilt of the target because both the analysis beam and

sputtering beam were oriented at 30° to the target normal.

It may be true, however, that S is larger for this configuration than it would be for perpendicular irradiation, since more energy (1/0.866 = 1.15) was being deposited in the near surface region of the target.

D. Related Data from the Literature

In the discussion of the experimental results in chapter V, we will want to compare the ice data with results of other experiments.

1. H and He Sputtering of H_2O (solid)

In a series of experiments performed at Bell Laboratories, the erosion of H_2O ice was measured for H and He ions between 6keV and 1.8MeV. These data have been published (Brown et al. 1980a). Two graphs taken from this paper are shown in figures 4i and 4j. These graphs show that the sputtering yield curves of ice by H and He ions are clearly related to the electronic stopping power curves for these ions in ice. Brown et al. claim that a good fit to the proton data is given by $S \propto dE/dx)_e^2$. The dE/dx curve was obtained by using Bragg's rule on dE/dx data from Anderson and Ziegler (1977) tables. The relationship between the sputtering yield and the stopping power for He ions is less clear. The curve for the sputtering yield peaks at a lower energy than that for the stopping power. They claim that this discrepancy is minimized by correcting the stopping power curve to account for that fact that the ions are not entering the target in their equilibrium charge states. This effect would tend to move the peak of the electronic stopping power curve to a lower energy. The stopping powers used by Brown and coworkers were calculated using graphs from Ziegler (1977) and Bragg's rule. The dE/dx values in figure 4j are H_2O(solid) experimental values from Matteson (1977).

The Bell group has also measured the sputtering yield of ice with H_2^+ and H_3^+ beams at various energies (Brown et al. 1980a). They find that the erosion yield is nonlinear for these molecular ions. That is, the yields for H_2^+ and H_3^+ ions, when divided by 2 and 3 respectively, do not lie on the same curve as the erosion yield for H ions.

They report that the sputtering occurs stoichiometrically within the accuracy of the measurements. They confirmed this result by eroding D_2O films with ^3He ions. By using the ^3He, D reaction, they were able to measure both the D and O in the target. The film stoichiometry stayed 2:1 within ±2% over a major change in film thickness. The temperature of the target substrate was examined from 7°*K* to 155°*K*. Below about 100°*K* no temperature dependence of the yield was observed (Brown et al. 1980a).

Another paper from the same laboratory (Brown et al. 1980b) shows results of the temperature dependence of H and He sputtering of H_2O ice. The temperature was varied between 7 and 155°*K*. For the ion fluxes used, sublimation competes with erosion of the films at temperatures above ~130°*K*. The yields were measured with 1.5MeV He^+ and 900 keV H^+ ions. Both cases show a clear temperature independent region below ~100°*K* (in contrast to data on condensed xenon or alkali halides). The erosion yield for both ions increased sharply with increasing temperature for higher temperatures. In the temperature independent region, the yields varied approximately as $(dE/dx)_e^2$, and in the temperature dependent region, as dE/dx. The transition sets in at a temperature of ~120°*K* for 1.5MeV He, and ~80°*K* for 900 keV H. Brown and coworkers suggest that a Coulomb repulsion mechanism is operative at the lower temperatures, and a temperature dependent mechanism involving migration of

defects sets in at higher temperatures.

2. ^{19}F on UF_4

It is also of interest to compare the results the ^{19}F sputtering of ice with results obtained in Kellogg Lab by Griffith *et al.* (1980) on ^{19}F sputtering of UF_4, which is also an insulator. The data chosen for the comparison are taken from table 10a of Griffith (1979). These data are shown in table C and plotted in figure 4k. He has measured the sputtering yield of ^{235}U from UF_4 by ^{19}F for F energies ranging from 1.19-28.5MeV. Note that there is a dependence on the yield of ^{235}U as a function of the charge state of the incident F ions. This same sort of dependence was also seen in ice.

Also plotted in figure 4k are the results of the experiments with ^{19}F on H_2O where the yields for H_2O are divided by 200. Points are included only when the sputtering was done on both targets with the same incident F charge states. Error bars indicate experimental reproducibility. Also shown are curves for dE/dx on H_2O, and 1/4(dE/dx) for F on UF_4, both calculated using Bragg's rule and stopping powers given by Ziegler (1980). (In this same paper, Griffith *et al.* (1980) show energy spectra of sputtered U atoms after bombardment by 4.74MeV $^{19}F^{+2}$ and 80 keV ^{20}Ne beams.)

Meins (1981a) has recently performed extensive measurements of the charge state dependence of the sputtering of UF_4 with F ions. These results are discussed in relation to the ice results in chapter V.

3. Sputtering of alkali halides

Biersack and Santner (1976) have measured the sputtering yield of KCl under bombardment by 70-300 keV H^+,He^+,andAr^+ ions from 20–400°C. They found that the sputtering yield was much higher than expected from

collision cascade sputtering, followed $(dE/dx)_e$, and showed a temperature dependence of the form $S \propto e^{-mB/t}$. From experiments of the yield as a function of the thickness of the film, they conclude that depths greater than 2600Å contribute to the sputtering.

4. Heavy ion induced desorption (HIID)

Macfarlane and Torgerson (1976a) have studied desorption of Cs^+ and Br^- from CsBr films under bombardment by ^{252}Cf sources. They detected the charged fragments coming off the target using time-of-flight (TOF) mass spectroscopy.

Macfarlane and Torgerson (1976b) have also used ^{252}Cf sources to desorb biologically important molecules which are non-volatile and thermally unstable; such as Pt-thymine complex, vitamin B-12, and gramicidin. The ^{252}Cf source produces ion fragments with masses around 106 and 142, with energies of 104 MeV and 79 MeV. Molecular fragments with weights up to 3500 amu have been detected coming from the target. The spectra contain intense peaks which correspond to the whole molecule having been desorbed. Macfarlane and Torgerson (1976a) claim that the spectra obtained using TOF mass spectrometry were Maxwell-Boltzman distributions characteristic of thermal spectra for elevated temperatures.

Duck et al. (1980a, 1980b) have studied the desorption of organics with heavy ion beams obtained from a tandem accelerator. They, too, have used TOF mass spectroscopy, and were sensitive only to the charged fraction of the desorbed ions. They have assumed that the charge/neutral fraction remained constant as different parameters of the experiment were varied.

Oxygen and sulphur beams with energies ranging from 8-40MeV were used to bombard thin (30-70 $\mu g/cm^2$) samples of valine deposited on Ni foils. Valine is a non-volatile biomolecule, with a molecular weight of 117.15 amu ($(CH_3)_2CHCH(NH_2)COOH$). The fragments most commonly seen in the mass spectra were $[valine+H]^+$, $[valine+Na]^+$, $[valine-COOH]^+$, NH_4^+, H^+, H_2^+, H_3^+, Na^+, and K^+. The mass spectra were very similar to those obtained by fission fragment induced spectra.

They also investigated the energy distributions of the desorbed ions parallel to the axis of the TOF specrometer. They found that the H^+ distrubution was relatively broad with a half width $\Delta\varepsilon$ of 6eV, and a median energy ε of 5-6eV. For the Na^+ fraction, $\Delta\varepsilon$ = 2-4eV, ε = 1-2eV, and for the desorbed organics, like $[valine-COOH]^+$, $\Delta\varepsilon<1eV$, and $\varepsilon<1eV$. These widths and mean energies were studied as a function of the LET (linear energy transfer, also stopping power) by varying the energy of the incident ^{32}S beam. The widths, $\Delta\varepsilon$, of the distributions for H^+, Na^+, and the organics were constant for different ^{32}S energies. ε for H^+ increased slightly with increasing LET, less so for Na^+, and was constant for the organics.

They also studied the relative yields of the peaks $[valine+H]^+$, $[valine-COOH]^+$, Na^+, and H^+ as a function of the energy of the ^{32}S and ^{16}O beams. Their results were as follows. The yields increased with increasing LET. The yield curves displayed double branching when plotted as Y vs dE/dx; this indicates that the yields were not the same for equivalent values of dE/dx on either side of the peak of dE/dx. The yield ratios of Na^+, $[valine-COOH]^+$, $[valine+H]^+$ desorbed from the same sample surface were independent of the LET and the primary ion used. With different targets, the ratio of $[valine+H]^+$ to $[valine-COOH]^+$ remained unchanged.

Another set of measurements using TOF mass spectroscopy was made at Uppsala by Hakansson and coworkers (Hakansson et al. 1981a, 1981b, 1981c). They studied desorption of ergosterol ($C_{28}H_{44}O$ m=396.1 amu, looking at $M^+$and$(M+H)^-$ peaks), glycylglycine ($C_4H_8O_3N_2$ m=132.1 amu, looking at $(M+H)^+(M-H)^-(M+Na)^+(2M+H)^+$ peaks, and CsI looking at $(Cs_{n+1}I_n)^+$ n=1 0,1,2 with Cs^+ dominating the spectrum. The Uppsala measurements were performed as a function of the velocity, angle of incidence, and charge state of the incident beam.

Ergosterol, CsI, and glycylglycine were bombarded with a variety of beams at different velocities (^7Li, ^{12}C, ^{16}O, ^{32}S, ^{63}Cu, and ^{127}I) The beams were said to have equilibrium charge state distributions (Hakansson et al. 1981a).

For the CsI targets, the yield curves have peaks as do the curves for dE/dx. The yield curves show no particular evidence for a $(dE/dx)^2$ or $(dE/dx)^4$ dependence. The yield curves are double branched, similar to the effect seen by Duck et al. (1980a, 1980b). (They found discrepancies in the tabulated dE/dx tables, however, which could be a cause for the double branch effect.) The yields do increase with increasing Z of the incident ion.

The ergosterol M^+ peak shows a $(dE/dx)^2$ dependence. When the shapes of the yield curves for Cs^+, glycylglycine, and ergosterol are plotted vs the velocity of Cu ions for high and low velocities, the curves are very similar in shape. There is a threshold velocity around the Bohr velocity where the yield increases rapidly with increasing ion velocity.

The yields of ergosterol vs Cs^+, for the ratios Y(I)/Y(S), Y(I)/Y(O), and Y(I)/Y(Cu) do not scale with dE/dx.

The sputtering yields of CsI, ergosterol, and glycylglycine were measured with ^{16}O, ^{32}S, ^{63}Cu, and ^{127}I beams at MeV energies as a function of the incident angle ϑ of the beam (Hakansson et 1981b). 20 MeV O on Cs^+ gave $1/\cos\vartheta$, 16 MeV S, Cu on glycylglycine gave $1/\cos\vartheta$, 16 MeV S on ergosterol gave $1/\cos^2\vartheta$, and high dE/dx ions on ergosterol gave $1/\cos\vartheta$. Transmission yields of Cs^+ ions with 42 MeV ^{16}O showed almost the same angular dependence as backward sputtering.

A final set of experiments reported on by the Uppsala group was the incident charge state dependence of the yields of CsI, glycylglycine, and ergosterol (Hakansson et al. 1981c). The beams used were 20 MeV oxygen, for charge states +2-+8. The charge state dependence of the yield was quite pronounced. These results are discussed in chapter V in relation to charge state effects in H_2O and UF_4.

5. Other frozen volatiles

Ollerhead et al. (1980) have studied sputtering of frozen xenon at Chalk River. On metal substrates they saw a thickness dependence of the yield (the yield increased as the thickness increased) for xenon layers up to $250\times10^{15}/cm^2$. At that point, S levels off. It was also noticed that there was lateral transport of the xenon (the sputtered xenon layers were uneven). When SF_6 was used as a substrate instead of a metal, the yield decreased with increasing target thickness.

There was also a strong temperature dependence of the sputtering yield. Rather peculiar results were found for the dependence of the yield on the stopping power. For He erosion, $Y \propto dE/dx)_e$, for N^+, $Y \propto dE/dx)_n$, and for Ar^+, $Y \propto dE/dx)_n$ at lower energies. The angular dependence was stronger that $1/\cos\vartheta$. The yield was also measured with 250 eV e^- (S=0.03), 0.5 MeV H^+ (S=0.3), and 1 MeV ^4He (S=2).

Besenbacher et (1981) at Aarhus have studied the sputtering of argon with He beams as a function of target thickness, deposition rate, substrate temperature, current density, specific energy loss, and ionization density.

They found that the yield increased with increasing target thickness up to $2\times10^{17}Ar/cm^2$. From 6-24K the yield was independent of T, but showed a sharp increase for $T\geq25°K$. The yields agree for ^4He and ^3He at the same velocities. $Y(He^{++}) > Y(He^{+})$. They also find that for He on argon, the sputtering yield was proportional to the square of the electronic stopping power.

6. Sputtering of other insulating materials

Recent results were obtained by Qiu et al. (1981) in the Kellogg Radiation Lab on the sputtering of Al_2O_3 and $LiNbO_3$ with high energy Cl atoms. These targets were chosen to test the dependence of the sputtering yield on the thermal diffusivity of the target. Al_2O_3 is known to have a high thermal diffusivity and low electrical conductivity. $LiNbO_3$ was chosen for comparison to the Al_2O_3 because it has a relatively low thermal diffusivity. Al_2O_3 does not register tracks for $dE/dx \leq 40MeV/mg/cm^2$, whereas $LiNbO_3$ has a track registration threshold at 18.5 $MeV/mg/cm^2$ (Sigrist and Balzer 1977). The thermal diffusivities for Al_2O_3 and $LiNbO_3$ are $145\times10^{-3}cm^2/sec$ and $15\times10^{-3}cm^2/sec$ (25°C), respectively.

Both targets showed enhanced yields that were associated with the electronic stopping power for the incident chlorine (chlorine energies used were between 3 and 25 MeV). A remarkable result was that the aluminum and niobium yields from the two targets were approximately equal. This was unexpected since the two materials are very different in their thermal properties, and $LiNbO_3$ is a much softer material than Al_2O_3.

Experiments are also being done on amorphous and crystalline SiO_2 targets. These were chosen because the thermal diffusivities of these two forms of SiO_2 differ by at least one order of magnitude. The sputtering yields for both types of SiO_2 were nearly equal and were approximtely ten times larger than for Al_2O_3 (Qiu 1981).

V. Discussion of Results

This chapter is devoted to a discussion of the data presented in chapter IV. The discussion is divided into three sections. In section A we compare the data to theoretical models presented in chapter I. In section B we present general features of the data, and finally, in section C we discuss how our heavy ion sputtering data compare to other experimental data on sputtering and ion induced desorption.

A. A Closer Look at the Models

Recall that in the thermal spike model of sputtering (Sigmund and Claussen 1980, Macfarlane *et al.* 1976a, Ollerhead *et al.* 1980), and the thermalized ion explosion model (Seiberling *et al.* 1980), there are three time scales we must consider. These are t_{ea}, t_{hc}, and t_{aa}. t_{ea} is the time it takes an electron which has been freed by the passage of the high energy incident ion to transfer its energy to the atoms in the solid via collisions. t_{aa} is the time for neighboring ions created along the particle track to recoil under mutual Coulomb repulsion, and collide with their neighboring atoms in the solid. t_{hc} is the characteristic time it takes for the undisturbed solid to conduct heat away from a hot cylindrical region.

The thermal spike model of sputtering requires that the electrons freed by the incident ion undergo a sufficient number of collisions with atoms in the hot spike region that they are able to transfer their energy to the atoms. In order for the thermal spike model to work, $t_{ea} < t_{hc}$. In the thermalized ion explosion model, on the other hand, recall that the relevant time scale is whether the ions created by the incident beam have sufficient time to collide with neighboring atoms, as they recoil under mutual Coulomb repulsion, to create a hot region in the target. This would require that $\sim 10 t_{aa} < t_{hc}$.

Seiberling et al. calculated these numbers for F incident of UF_4. For the sake of comparison, we discuss the calculations for UF_4 in parallel with the related calculations for H_2O.

For a mass m, the maximum energy that can be transferred in a head on collision with mass M (m<<M) is (4m/M)E where E is the initial energy of mass m. For a 1 eV electron in H_2O, in any one collision, the maximum energy transferred by the electron to an O atom is 4m/M(1eV)= = 1.36×10^{-4}eV. The time required for the electron to transfer 1eV of energy is t_{ea} = (M/4m)d/v where d is the interatomic spacing in ice and v is the velocity of a 1eV electron. v = 6×10^{7} cm/sec. For ice, d = 3.7×10^{-8} cm = 3.7 angstroms. Therefore d/v = 6.2×10^{-16} sec. This gives us t_{ea} = $(6.2\times10^{-16}\text{sec})/(1.36\times10^{-4})$ = 4.6×10^{-12} sec. In UF_4 t_{ea} = 7.5×10^{-11} sec, and represents the transfer of energy from an e^- to a ^{235}U atom. t_{ea} calculated in this way, of course, gives a lower limit on the time required for this transfer of energy, since one assumes a head on collision with maximum energy transfer at every lattice spacing. Note that in any individual collision, an arbitrarily small amount of energy cannot be transferred.

The heat diffusion equation solved for cylindrical geometry with constant thermal conductivity κ and heat capacity C, and a line source of energy density ε per unit length at r=0 and t=0 gives the solution (Vineyard 1976)

$$T(r,t)=\left[\frac{\varepsilon}{4\pi\kappa t}\right]\exp\left[-\frac{C\rho r^2}{4\kappa t}\right]$$

where T is the target temperature, and ρ is the target mass density. The characteristic time for conducting heat from this cylinder is

$$t = \frac{C\rho r^2}{4\kappa} = \frac{r^2}{4K}$$

where K is the thermal diffusivity of the undisturbed solid. A graph of the thermal diffusivity, K, of amorphous ice is given in figure 5a. K was calculated by taking (κ/ Cρ) where ρ was chosen as 1 gm/ cm^3, and the values of the thermal conductivity, κ, were those given by Fletcher (1970) for polycrystalline ice. Values of the heat capacity, C, are from measurements by Sugisaki et al. (1968) for amorphous, polycrystalline, and cubic ice. At 10°K, K = 0.24cm^2/ sec and at 30°K, it reaches a peak value of K = 1.39cm^2/ sec. To calculate $t_{hc} = r^2/4K$, we use r=20 angstroms as the spike radius (as a comparison with Seiberling et al. who chose r=20 angstroms as the hot spike radius in UF_4, an experimentally determined number). r^2 = 4×10^{-14}cm^2. Therefore, t_{hc} = 4×10^{-14} sec for 10°K ice, and 7×10^{-15} sec for 30°K . t_{hc} for UF_4 at 60°K, and a spike radius of 20 angstroms, is given by Seiberling et al , to be 1.3×10^{-12} sec. In either case, $t_{hc} < t_{ea}$ which bodes ill for the thermal spike model.

Now, examine the thermalized ion explosion model. Recall that in this model the important time scale is t_{aa}, the time it takes a pair of neighboring ions to recoil one lattice spacing and collide with neighboring atoms of the solid. Seiberling et al. calculate that if two adjacent molecules are triply ionized, and recoil from one to three lattice spacings, they will gain a kinetic energy V = 1/2 $(3e)^2$ [1/d-1/3d] = 10.2 eV for d= 4.3 angstroms in UF_4. The claim is that in each collision these recoiling atoms transfer half of their energy. They then calculate the time it takes a 1eV U atom to travel one lattice spacing - this time is 4.8×10^{-13} sec. This is to be compared with $1.3\times^{-12}$ sec they get by calculating t_{hc} for UF_4. They argue that after the passage of the high energy ion, the U

atoms have time to undergo several collisions and create a region of local thermal equilibrium before thermal conduction quenches the hot spike. Here we do this same calculation for H_2O. For an interatomic spacing of 3.7 angstroms, a pair of triply ionized (this would take on the order of 35 eV) molecules recoiling from one to three lattice spacings gain 8.5eV in kinetic energy. It takes a 1eV O atom 1.13×10^{-13} sec to travel one lattice spacing. The thermal quenching time for H_2O , t_{hc} was calculated to be 4×10^{-14} sec for 10°K amorphous ice. These time scales cast some doubt on the applicability of the thermalized ion explosion model to ice sputtering. Another point to note is that the thermal diffusivity of ice peaks at ~30°K, and is almost an order of magnitude larger here than at 10°K. The thermalized ion explosion model predicts that $S\propto 1/K$. We saw no correlation between S and 1/K as we varied the substrate temperature in the 10.0 MeV F runs (see figure 4e).

There were several assumptions made in estimating these times. The values we used for the heat capacity were for amorphous ice, but the values of the thermal conductivity were for polycrystalline ice. The assumption of the thermalized ion explosion model is that we have a hot cylinder surrounded by undisturbed material, and that heat is conducted out of the cylinder by the undisturbed solid. No such well defined boundary really exists between the "hot" cylinder and the undisturbed solid. Perhaps we would do better to use thermal diffusivities of ideal gases. In any case,it is clear that the equilibrium of the area around the passage of the ion is disturbed, and we cannot expect its thermodynamic properties to remain unchanged. It is not clear, however, what crystalline form we actually have after the target has been bombarded by the sputtering beam. In experiments performed at Bell Labs we were able to cbserve

the ice layers deposited before and after sputtering. Before sputtering, the layer was transparent, after sputtering it appeared frosty. The interpretation of this is that the ice goes down amorphous (see chapter IV) and turns polycrystalline under bombardment by the beam.

Assume for now that the hot spike radius is equal to 20 angstroms. This represents an area of $\pi r^2 = 1.3 \times 10^3$ Å^2. Typical sputtering F doses are $\sim 3 \times 10^{12} - 10^{13} F/mm^2$. For $3 \times 10^{12} F/mm^2 = 3 \times 10^{12} F/10^{14} Å^2$. This gives us 33Å^2/F. On the average, each r=20 Å cylinder sees [1.3×10^3Å^2/33Å^2/F]~40F. If in fact the ice goes polycrystalline under irradiation by the incident beam, then it may not be such a bad estimate to use the thermal conductivity of polycrystalline ice in calculating the thermal diffusivity of the ice.

Because we are not sure what crystalline form of ice we have, let us examine how the thermodynamic properties vary as the structure of the ice is changed. Sugisaki et al. (1968) measured the heat capacity of amorphous, cubic, and hexagonal ice. They found that at 20°K , the value of C in amorphous ice was about a factor of 2 larger than in cubic ice, by 40°K the values of C were the same to within 10%, and by 60°K the values of C for amorphous, cubic, and hexagonal ice differed by only a few percent.

Now consider the thermal conductivity, κ, of ice. At 0°K the magnitude of the thermal conductivity of ice is 2.2 W/m deg (Hobbs 1974, Fletcher 1970). This is ~4 times greater than that for H_2O (liquid) at 0°K. Down to −180°K, the thermal conductivity coefficient of ice increases with decreasing temperature. Landauer and Plumb (1956) found no significant differences in the thermal conductivity coefficients of laboratory grown single crystals , glacial single crystals, and polycrystalline commercial ice. It is easy to imagine that there would be significant differences in

the thermal conductivity of polycrystalline and amorphous ice. We were, however, unable to find a reference for the thermal conductivity of amorphous ice.

To illustrate how dependent the thermal conductivity is on the crystalline structure of a material, compare the thermal conductivities of amorphous and crystalline quartz (White 1959). The thermal conductivity of a dielectric quartz crystal peaks at ~10°K, with a maximum value of 10 W/cm deg. The value for amorphous quartz at 10°K is 0.001 W/cm deg. As the temperature increases, the thermal conductivity of the crystalline form is decreasing, and has a value of 0.2 W/cm deg at 100°K. The thermal conductivity for glassy quartz increases with temperature, and at 100°K is 0.004 W/cm deg.

As a note of interest, it may be possible to perform experiments with ice targets that have been doped to change their thermal conductivity. This kind of doping has been done for crystalline ice. It is not clear what the effect would be in amorphous ice. J. Klinger (1972) has measured the thermal conductivity of monocrystalline ice between 2 and 90°K. The maximum is situated between 7 and 8K and has a value of 1.5 $Wcm^{-1}K^{-1}$. The same sample was doped with hydrofluoric acid by diffusion, and the maximum in the thermal conductivity was found to be 1.4 $Wcm^{-1}K^{-1}$ at 7-8K (one month after doping). Thirty two months after doping, the maximum was at 15K and had a value of 0.15 W/cm K. This latter curve resembled those obtained for polycrystalline substances. The level of doping was ~10^{-6} mole/l after several months.

A calculation of the t_{hc} depends not only on the thermodynamic properties of the target, but on the choice of r, the radius of the hot cylinder. Seiberling et al. (1980) chose the value of 20 angstroms for UF_4,

based on experimental results. This value is similar to the radii of latent tracks in dielectrics (for fission fragment induced tracks in mica, diameters of up to 50Å have been seen (Fleischer et al. 1975)). Suppose we calculate the value of r required to give us values of t_{hc} and t_{aa} that support the use of the thermalized ion explosion mode. For a 1eV O atom H_2O, t_{aa} is 1.13×10^{-13} sec. If we want to allow 10 recoil collisions of the O atoms, we need 10 x $t_{aa} \sim 10^{-12}$ sec. $(10x t_{aa})/(t_{hc})$ is $(10^{-12}\text{sec}/4\times10^{-14}\text{sec}) = 25$. Therefore, our choice of r must be five times larger than the 20Å value we chose above. Thus, our cylinder must have a radius of 100Å. A cylindrical region of ice 100Å in radius, and one monolayer deep contains ~ 2300 H_2O. By the assumptions of the thermal spike model, this tells us that all the sputtering must occur from the first monolayer of the ice. It is difficult to imagine how this might occur.

Suppose, for now, that we ignore these difficulties involving the time scales since there there are so many uncertainties associated with the calculation. Let us proceed to the functional forms predicted for S in the thermalized ion explosion model, and see how well we can fit these forms to our data.

From chapter I we see that the functional dependence of S on the primary ionization rate, dJ/dx, may be predicted. Recall that there are two cases, depending on how one couples the spike radius, r_o, to dJ/dx. Case I predicts

$$S \propto \left(\frac{dJ}{dx}\right)^4$$

Case II predicts

$$S \propto \frac{dJ}{dx}\exp-[E_b r_o^2 / C(dJ/dx)^2]$$

where E_b is the surface binding energy of the target, and D is the normalization factor for dJ/dx.

The expression for dJ/dx used by Seiberling and coworkers, was

$$\frac{dJ}{dx} = Z_e^2\left(\frac{A}{\beta^2}\right)\ln\left(B\beta^2\right)$$

where

$$Z_e = Z\left[1-10^{-(1/3)(137\beta/Z^{0.55})}\right]$$

β =v/c and Z_e is the effective charge of the ion travelling through the solid. This expression for Z_e is from a paper by Heckman et al. (1963). This expression for dJ/dx was derived by Bethe (1930). The constants A and B depend on the material through which the ion passes. According to Mott and Massey (1965), the constant B is related to 1/I, where I is proportional to the ionization energy of the atoms in the material.

Fleischer et al. (1975) give the following formula for dJ/dx.

$$\frac{dJ}{dx} = \frac{C_1 C_2 Z^{*2}}{I_o}\beta^2\left[\ln\left(\frac{W_{max}}{I_o}\right)-\beta^2-\delta+K\right]$$

C_1 = $2\ (2\pi n_3 e^{4)/mc^2}$

n_e = # e^-/cm^3 in the solid

m = electron mass

W_{max}= $2mc^2\beta^2\gamma^2=p^2/2m$

γ = $(1-\beta^2)^{-1/2}$

δ = relativistic polarization effect

K = constant that depends on stopping medium

I_o = ionization potential of the most loosely bound e^- in the solid

C_2 = the effective fraction of e^- in the solid in the most loosely bound state

Z^* = effective charge of the ion in the solid

For high enough velocties, dJ/dx should scale as Z^2_{eff} for incident ions and electrons of the same velocity. Seiberling et al. (1980) have chosen B=45 MeV/amu which they obtained by fitting ionization data taken from scattering protons and electrons on argon gas (Schram et al. 1965, DeHeer et al. 1966). A is an overall normalization which is arbitrarily adjusted.

The position of the peak of dJ/dx as a function of energy will depend on our choice of B. Since B is related to the ionization energy of the solid, let us examine the lowest ionization energies for a number of atoms and molecules. H_2O (12.6 eV), Ar (15.8 eV), U (6.08 eV), F (17.4 eV), H (13.6 eV), O (13.6 eV) (from CRC)(Weast 1968) It is not clear from these values whether it makes sense to use the B value of argon to calculate dJ/dx for UF_4. The values look somewhat better for H_2O.

Values for B have also been measured by Schram et al. (1965) for electrons incident on various gases. If the energy dependence of dJ/dx is

$$\frac{dJ}{dx}(E) = \frac{A(Z^*(E))^2}{E}\ln(BE)$$

They list experimentally determines values of B

B(Ar)= 0.049 eV^{-1}±0.002

B(H_2)= 0.281

B(O_2)= 0.053

It is difficult to justify the choosing B for H_2O from Ar data, or data obtained from Schram et al. Notice, however, that B chosen by fitting the Ar data (Seiberling et al. 1980) gives a peak energy for dJ/dx that seems to correspond well to the peak in the sputtering data.

Meins and colleagues have performed a series of experiments in which they measured transmission sputtering and stripped charge state sputtering of F on UF_4 (Meins 1981a). They do a least squares fit to the data of $(dJ/dx)^4$, where Z_{eff} is the Heckman (1963) value for the equilibrium charge state of F. Transmission data and stripped data give approximately the same result, B=35 amu/MeV. For the case of stripped Cl and F ions, the value of A=1.2×10^{-8} for both Cl and F, and for the transmission sputtering A(Cl)= 3.5×10^{-8} and A(F)= 1.7×10^{-8}.

We compare the F on H_2O data to curves of $(dJ/dx)^4$ for B =45 amu/MeV and 35 amu/MeV (see figure 5b). The peak energy of the sputtering yield seems to coincide more closely with the choice of B=45amu/MeV.

It is clear that before we can make detailed comparisons of the models to our data, we must improve our understanding of dJ/dx. As a final note, C.C. Watson (1981) points out that the Bethe calculations (see above) of dJ/dx may not be appropriate in the case of a heavily ionizing incident ion. The previous calculations of dJ/dx have been performed assuming individual interparticle interactions between the incident ion and the target atoms. The energy appearing in the constant B is related to the ionization potential of the individual target atoms. However, if the

track of ionization left by the incident ion is very dense, then more energy than just the ionization potential is required to remove e^- and keep them away. In addition to overcoming the ionization potential, enough energy must be supplied for the electron to escape the track of ionization which appears like a line charge to the freed electrons.

B. General Features of the Data

1. Compare S curves to (dE/dx), $(dE/dx)^2$, $(dE/dx)^4$.

An obvious quantity with which to try to fit the sputtering data is the electronic stopping power. This raises the question of which dE/dx curves to use for this comparison. This problem is discussed in chapter IV, section C-2 (see figures 4f and 4g). We have chosen to use Anderson and Ziegler (1977) values for H ions, Matteson (1977)(solid) experimental values for He, and Ziegler (1980) values for F (see figures 4i, 4j, and 5c).

Compare $S \propto (dE/dx)^n$ for H_2O ice bombarded with H, He, and F beams. We see from the figure 4i that S bears a strong resemblance to an arbitrarily normalized curve of $(dE/dx)^2$. Here the S values were taken at H energies from 6 keV - 1.5 MeV (Brown et al. 1980a). The dE/dx values chosen were from the tables of Anderson and Ziegler (1977). The same thing was done with the He data from Brown et al. (see figure 4j). In this case, the fit of $(dE/dx)^n$ to S is less convincing, primarily because the curves for S and dE/dx do not peak at the same He energy. For F incident on H_2O, it is not clear that any power of dE/dx (up to 4) will fit the data. These problems may, however, lie in the difference between the equilibrium charge state (reflected in tables of measured or calculated dE/dx values) and the incident charge state of the beam (see figure 4c). Comparing figure 5c to figure 5b, it is difficult to tell whether $(dJ/dx)^4$ or $(dE/dx)^4$ provides a better fit to the data.

It is also instructive to combine values of S for H, He, and F on one graph of S vs dE/dx (see figure 5d). The data show no obvious dependence on $(dE/dx)^n$ although n=2 seems to do better than n=4.

There are, perhaps, different regimes in dE/dx which have different sputtering mechanisms. For example, the thermalized ion explosion model requires a sufficient density of ionization along the path of the incident particle, so that there will be several target atoms repelling one another and contributing to the local thermal equilibrium around the track of the ion. According to Fletcher (1970) in ice the smallest ionization potential is approximately 12.5 eV. The value of dE/dx for protons on ice ranges from $16.4eV/10^{15}H_2O/cm^2$ at 10 keV to $29.4eV/10^{15}/cm^2$ at 80 keV. A monolayer of ice represents $1.03\times10^{15}H_2O/cm^2$. There is marginally enough energy available to ionize two atoms per lattice spacing for the highest dE/dx values, and this assumes that all of dE/dx goes into ionization of the target, which is not actually the case.

Again, in the case of F incident on the ice, the curve for S peaks at lower energy than that for dE/dx, but it is not clear to what extent this represents our lack of knowledge about dE/dx. The resulting "hairpin" shape of the (dE/dx) vs S curve is shown in figure 4d. The direction of the arrow represents encreasing energy.

2. General remarks on energy available for sputtering

Here we list some very general observations about energy scales involved in the sputtering of ice targets by ^{19}F beams.

Assume for now that the radius of the cylinder from which sputtering occurs is 20Å. The cross-sectional area of this cylinder is then, $1.26\times10^{-13}cm^2$. There are $7.3\times10^{14}H_2O/cm^2$ in ice with a density of $1gm/cm^3$. Suppose that in the sputtering process, atoms are removed

uniformly from the area where the cylinder intersects the surface of the solid (a reasonable assumption from the thermalized ion explosion model which says the hot spike is a gas at elevated temperatures). This means that for a 20Å radius cylinder, 92 H_2O molecules are removed from a monolayer of the ice. To sputter 1000 water molecules, ~11 monolayers of the cylinder must be removed. This represents a depth of ≥40 angstroms. For the sake of calculation, take dE/dx for a $^{19}F^{3+}$ = $395.5 eV/10^{15} H_2O/cm^2$. In a depth of 40Å, there are $1.33 \times 10^{16} H_2O/cm^2$. Therefore, the energy deposited by the 10 MeV F ions will be $[395.5 eV/10^{15} H_2O/cm^2] \times [1.33 \times 10^{16} H_2O/cm^2]$ = 5.26 keV. This represents ~480 eV per monolayer of the ice.

To melt ice at 0°C takes $0.06 eV/H_2O$, to vaporize it at 100°C takes $0.39 eV/H_2O$. The sublimation energy of ice 1h at 0°C is 0.49eV (Hobbs 1974). To melt a volume of ice containing 1000 H_2O molecules requires 60 eV. To vaporize the same 1000 H_2O takes 390 eV, to sublimate them would require 490 eV. It is a reasonable assumption in the thermalized ion explosion model to assume that atoms are removed uniformly from the surface of the solid where the hot cylinder intersects the surface. The assumption made by Seiberling et al. (1980) was that local thermal equilibrium is reached inside the cylinder and thermal evaporation continues until the spike is quenched. Suppose we also assume that there is little transfer of energy vertically in the hot spike. Suppose, for now, that the 5.26 keV of energy deposited in the top 40 angstroms of the ice is all that is available for the sputtering. Some fraction of this energy will go toward imparting kinetic energy to the atoms of the solid. Without knowing what fraction of dE/dx contributes to the sputtering process, it is easy to imagine that there is ample energy available for melting,

vaporizing, or sublimating H_2O molecules (or clusters) from the surface.

Now suppose we consider the molecular bond energies of the water molecules. To remove the first H from an H_2O molecule requires 5.11 eV. To break the remaining OH apart takes 4.40 eV (Hobbs 1974). If it is true that we have a maximum of 5260 eV at our disposal, it is clear that the sputtered H_2O molecules cannot all be removed as sputtered atoms. There is not enough energy available to remove all the observed sputtered material and break molecular bonds in the same process.

3. Sputtering as a function of incident charge state

We made some sputtering experiments as a function of the incident charge state of the ^{19}F beam. These were done at (10.0 MeV, (+3, +4, +6; eq= +5.8), 20.0 MeV (+4, +8; eq = +6.8), and 25.0 MeV (+5, +8; eq = +7.1). In all cases, the sputtering yield increased with increasing charge state. At 25 MeV the yield went from S(AuC)= 289 to 817 in going from +5 to +8. This is a factor of 2.8. The increase at 20 MeV was from 348 to 752 in going from +4 to +8, a factor of 2.2. Caution should be exercised in using these sputtering yields for 20 MeV, however. For the +8 charge state, the ice had eroded away to the gold marker in some places. Therefore, the yield at 20 MeV (charge state +8) is a lower limit on the real sputtering yield. The same trend, although less severe, was found at 10 MeV. For charge states of +3, +4, and +6, the yields were 1263, 1484 (+4/+3= a factor of 1.2), and 1499 (+6/+3=a factor of 1.2). (S=1263 is the sputtering yield obtained by averaging the two +3 runs at detector positions 0.760 and 0.860 of run (i) (see table A). This number is larger than the average of all the other runs taken with 10 MeV $^{19}F^{3+}$ of which there are 12. This average gives S = 1021 (see set (e), (g), first two of (h), first two of (i) in table A). These S values were obtained from the gold centroid

method. For the sum in the oxygen peak, the points at 0.760 and 0.860 or run (i) give S=986 (+3), S=1238 (+4) (+4/+3 =a factor of 1.3), and S=1505 (+6) (+6/+3= a factor of 1.5). Averaging all 12 of the +3 runs gives S=896.

The electronic stopping power is proportional to the square of the effective charge of the ion at a given depth in the target. The effective charge represents the charge seen by the atoms of the solid, and at a point deep enough into the solid, this effective charge will equal the equilibrium charge state of the ion. Because we observed such a marked effect when we increased the incident charge state, the sputtering yield data tell us that this equilibrium is not reached on a length scale that is smaller than the depth from which the sputtering occurs. Were the charge state to equilibrate in the first few monolayers of the solid, we would not expect to see S vary much with a change in the incident charge state of the beam. This also implies that the values we use for dE/dx are not actually representative of the energy loss experienced by the ion in the region of the target from which sputtering occurs. dE/dx tables are given for energy loss in thick targets where presumably the charge state has reached equilibrium.

Meins and coworkers have recently performed a series of experiments (Meins 1981a) in which they varied the incident charge states of F and Cl ions incident on UF_4. They put a series of stripped charge states into the target and measured the sputtering yield as a function of the charge state.

Griffith (Seiberling et al. 1981) has derived an expression which can be used to fit the charge state data as a function of a ratio of depth scales in the target. Let Z_i be the initial charge state of the beam, and Z_e the

equilibrated charge state for that beam. λ_z is the charge equilibration length, and λ_s the sputtering depth. Griffith assumes

$$Z(x) = [Z_i + (Z_e - Z_i)(1 - e^{-x/\lambda_z})]$$

where x represents the depth the ion has travelled into the target ($x=0$ is the surface of the target). The sputtering yield, S, is proportional to the integral

$$I = 1/\lambda_s \int_0^\infty Z(x)^n e^{-x/\lambda_s} dx$$

$$= 1/\lambda_s \int_0^\infty [Z_i + (Z_e - Z_i)(1 - e^{-x/\lambda_z})]^n e^{-x/\lambda_s} dx$$

$$= Z_e \sum_{k=0}^{n} (-1)^k \frac{n!}{k!(n-k)!} \frac{1}{1+(\lambda_z/\lambda_s)k} \left[\frac{Z_e - Z_i}{Z_e}\right]^k$$

We can fit this expression to our data. For Z_e we use the values calculated from Ziegler's (1980) expression for the equilibrium charge state (see chapter IV, section C-2). We have only two points at which to do the fitting. Neverthless, it is interesting to compare our results for H_2O with those obtained by Meins for UF_4 (Meins 1981a).

Choosing n=8, we find that at 25 MeV, λ_z/λ_s = 1.7. We do not fit the 20 MeV points because the +8 point represents only a lower limit on the yield. At 10 MeV, +3 and +4 points give λ_z/λ_s=1.4 for S(+3)=1263, and λ_z/λ_s=1 for S(+3)=1021. Using λ_z/λ_s of 1.4, we calculate the ratio we expect for the sputtering yield of the +6 and +4 points at 10.0 MeV F. If we use S(+4)=1484, we expect a yield for S(+6) =3500 (a factor of 2.4 times larger than the +4 point). We do not see this large an increase in the data. Note also, that the charge state effect on S is much more severe at the higher energies (20 and 25 MeV) where the yields are much

smaller. Perhaps we are seeing a saturation effect at the higher yields (10MeV) and only so much of an increase in S can be supported by the energy deposited by the incident ion. Perhaps this could give us some handle on what fraction of the electronic stopping power goes into sputtering.

Meins (1981a) has a much more complete set of charge state data for UF_4. He finds that at 9.5 MeV, $\lambda_z / \lambda_s = 5$ and at 19 MeV, $\lambda_z / \lambda_s = 2.5$. For 28.5 MeV, $\lambda_z / \lambda_s = 1.5$. This latter value agrees fairly well with the ratio of 1.7 obtained for 25 MeV F on ice. The value at 10 MeV does not agree so well with the ice results, but remember that in the ice, we are not seeing the expected rise in the yield extrapolating from charge states of +3 to +4 and +6, which we have said may be a saturation effect. They find that the choice of n=8 fits their data well. This would support a $(dE/dx)^4$ or $(dJ/dx)^4$ interpretation of the data, although it is not clear how sensitive we are to the value of n. Meins (1981b) has tried fitting the data with a value of n=6. This produces the same effect of the shape of the curve as changing the ratio λ_z / λ_s.

To summarize, all our results are consistent with the statement that the incident charge state does not equilibrate in the solid until a depth that is comparable to or larger than the depth which contributes to sputtering.

This is perhaps not surprising. Sofield and coworkers (1980) have performed a set of experiments with 40 MeV ^{16}O ions incident on thin C and Al targets. They used incident charge states of +6, +7, and +8 and studied the charge equilibration as a function of target thickness. They found that the beams equilibrated after passing through 600-800 Å of the C and Al targets. If we assume a hot spike radius of 20 Å for the ice, 1000

H_2O molecules are obtained in a cylinder of radius 20 angstroms, and a depth of ~25 angstroms.

It is clearly desirable to perform a more extensive set of measurements on the erosion yield of ice as a function of the incident charge state of the F ions at (relatively) high and low sputtering yields. It would also be interesting to perform a series of measurements of the sputtering of ice with charge equilibrated beams. This could be done by putting a foil stripper upstream of the target. Data of this sort would make comparisons of the erosion yield to $(dE/dx)^n$ and $(dJ/dx)^n$ more meaningful.

C. Other Dielectric Sputtering Data from the Literature

1. Erosion of ice by H and He beams

In the previous two sections, A and B, we have made several comparisons with H and He sputtering of ice, to F sputtering of ice. It would also be interesting to sputter with yet a heavier beam, such as Cl, which has a higher dE/dx. More work should be done with the incident charge state effects on the yields. The temperature dependence of the yield should be investigated until the threshold temperature for the heavy ions is found.

A final comparison that can be made between the H, He (Brown et al. 1980a), and F results is to see at what energies the sputtering yield curves peak for the different ions. The peak in the sputtering yield curve for F on H_2O is between 6 and 8 MeV. For He it is ~250 keV, and for H ~70 keV. These correspond to, respectively, 370 keV/amu, and 63 keV/amu, and 70 keV/amu.

2. Comparison with F on UF_4 data

It is interesting to compare data taken with ^{19}F incident on UF_4

(Griffith et al. 1980) to that taken on ice. Several comparisons have already been made in previous sections of this chapter. The yields vs F energy are compared in figure 4k. It is interesting to note that the two curves for S not only peak at the same incident F energy, but that they are remarkably similar in shape when normalized to the same peak values ($S(H_2O)/200$). The curves for dE/dx, however, do not peak at the same energy for F on H_2O and F on UF_4. Also, the magnitude of dE/dx for F on UF_4 is about 5-6 times larger than F on H_2O. The peak value of dE/dx for F on H_2O is about 7.5 MeV. For F on UF_4 it is ~12.5 MeV.

3. Alkali halides

The results of Biersack and Santner (1976) on the sputtering of KCl by H, He, and Ar beams have led to an interpretation of alkali-halide sputtering as a thermally activated process. The fact that the yield depends on a power of $(dE/dx)_e^n$, shows a depth dependence up to 2600Å, and has a temperature dependence of the form $S \propto e^{-mB/t}$ leads to the following conclusions. It has been suggested that excitons (bound electron-hole pairs) migrate to the surface of the sample where they de-excite and eject halogen atoms. Alternatively, it has also been suggested that H-centers (halogen atom interstitials) migrate thermally until they annihilate with F centers or reach the surface where they create an unstable excess of halogen atoms which are subsequently released from the surface. Once the Cl is gone, the remaining K evaporates from the surface (potassium has a low m.p., 63.7°C, and a high vapor pressure). This mechanism is not applicable to the ice data, at least in the temperature independent regime. It has been suggested by Brown, et al, that ice sputters by defect migration for temperatures in excess of ~100°K where the yield becomes temperature dependent and $\propto$ dE/dx.

4. Heavy ion induced desorption (HIID)

Macfarlane and Torgerson (1976a, 1976b) have studied the desorption of biomolecules by ^{252}Cf sources. Based on their results, they propose a thermal mechanism for the desorption of organic molecules from fission fragment bombardment.

They argue that the passage of the heavy ion creates a hot cylinder from which atoms of the solid evaporate. They are, however, vague about the details of how this heating occurs. That is, how heat is coupled from the excited electrons to the solid's atoms. They hypothesize a hot core around the track of the incident ion that is 20Å in radius. The heating, they claim, is done by short range secondary electrons, which create a heat pulse that lasts 10^{-11} sec.

The main results to keep in mind from these experiments are that the CsBr targets give spectra that look thermal for the desorbed Cs^+ and Br^-. Using ^{252}Cf sources, there is a high probability for desorbing $[M+1]^+$ and $[M-1]^+$ where M>3400 amu. Even though with fission fragments deposit 100-800 eV/Å, large fragile molecules are desorbed non-destructively. The spectra do not show peaks corresponding to C, O, N, etc. The fragmentation of the molecules follows specific patterns for each type of target.

The thermal model proposed by Macfarlane and Torgerson suffers from the same problems as the hot spike model of sputtering discussed in chapter I and earlier in this chapter.

Duck *et al.* (1980a, 1980b) have also studied the desorption of large biomolecules by ion beams. They have bombarded valine targets by ^{16}O and ^{32}S beams ranging in energy from 8-40MeV. Their desorption spectra show similar fragmentation patterns for ^{252}Cf, ^{16}O, and ^{32}S. The energy

distributions were relatively independent of the primary ion, and depended mostly on the secondary ion. Recall that they measured the energy distributions of the desorbed ions parallel to the axis of the TOF spectrometer, and found that the width of these distributions, at least for the organic species, was independent of the LET of the incident ion. This led them to favor the high frequency perturbation model proposed by Krueger (1977) rather than a thermal pulse model (Sigmund and Claussen 1980). They argue that a thermal pulse model would predict that $\Delta\varepsilon \propto$ LET, which is in contradiction with the experimental results.

Regarding their double branching on the plots of yield vs dE/dx, they argue that this effect may be explained by restricting the fraction of the LET that contributes to sputtering by a function f. They argue that they have found a universal function $f(\xi)=1.72e(-2.32\xi)$ where $\xi=v/v_0Z$. v is the velocity of the incident ion, v_0Z is the Bohr velocity of the primary ion's K electrons. They propose that $Y=C_{si}\times LET^*$, where C_{si} is a constant which depends on the secondary ion being desorbed, and $LET^*=f\times LET$ (Duck et al. 1980b).

The function f tells us that the portion of the LET that contributes to sputtering decreases with increasing projectile velocity. This, they claim, agrees with the high frequency plasma desorption model, which should favor the desorption of polar bound species. The efficiency of the desorbing perturbation is determined by the strength (determined by Z_{eff}) and duration (velocity and linear dimensions of the surface potential). The efficiency should decrease with increasing ion velocity, due to a larger probability for recapture after a shorter perturbation. When they plot $Y \propto LET^*$, the double branching disappears. It is interesting to note that $f(\xi)$ is very similar to an expression used by Northcliffe (1960) to

describe the effective charge of an incident ion, $1-(Z_{eff}/Z)^2 = 1.85exp(-2\xi)$. We have also seen double branching in the ice under bombardment by He and F ions. Caution must be exercised due to the problems of finding reliable curves for dE/dx. However, it is interesting to note that our double branching is similar to that seen in the valine data. That is, the yield curve peaks at a lower energy than dE/dx. Hakansson et al. (1981a) have suggested a plasmon oscillation mechanism that could cause desorption.

In an attempt to test predictions of the electron plasma desorption model, Krueger and Wien (1978) have studied desorption of different molecules from clean metal surfaces. They argue that plasma desorption favors polar bound species. They have adsorbed H_2O_2, N_2, CO, C_2H_4, C_2H_6, C_3H_7OH onto Al, Ni, and Cu surfaces, and studied the desorption of these molecules with ^{252}Cf fission fragments. The yields of the metal atoms and ions may be understood by collision cascade sputtering, while the yields of the ion species H^+, H^-, Na^+, and K^+ (polar bound) were high, and presumably due to plasma desorption. The CO yield from CO-Ni was low, presumably due to the chemical bolding between the CO and Ni surface.

Krueger et al. (1978) suggest that the desorption process be studied via ultra- short pulsed lasers which could provide electronic excitation without heating of the target. If enhanced desorption were observed following the laser pulses, this would provide support for the plasma desorption model. There are some enticing similarities between the HIID results and the enhanced sputtering yields of ice. In both cases the yields are related to the electronic stopping power, and increase with increasing Z of the incident ion. Both sets of data show double branching when the yield is plotted vs the stopping power.

More data on heavy ion induced desorption has been taken at Uppsala by Hakansson et al. (1981a, 1981b, 1981c). They have measured the yields of ergosterol, CsI, and glycylglycine after bombardment by energetic ions. Uppsala data have been found to be in disagreement with the Krueger (1977) model of electron plasma desorption which should favor desorption of polar bound species. They have found large yields of radical ions from ergosterol and retinoic acid targets. Instead of plasma desorption, they advocate the use of a thermal spike model.

One model which must be discussed briefly is a thermal pulse model suggested by Sigmund and Claussen (1980). In this model the thermal diffusivity of the target goes as $T^{\frac{1}{2}}$, and the yield Y is given by

$$Y \propto \frac{F_D^2}{U^2} g\left(\frac{U}{kT_o}\right)$$

T_o = initial core temperature

$g(U/kT_o)$= function similar to exponential

U = surface potential

F_D = kinetic energy/unit track length available for kinetic energy of sample atoms related to dE/dx

$$kT_o = \frac{F_D}{2\pi N \langle r_o^2 \rangle}$$

n = number of target atoms/unit volume

r_o = track radius

If one assumes (as do Besenbacher and coworkers 1981) that $\langle r_o^2 \rangle \propto F_D$ (which is the assumption of a fixed spike temperature), one gets

$$Y \propto F_D^2 \propto \left(\frac{dE}{dx}\right)^2$$

if F_D is some fixed fraction of (dE/dx).

This model could explain the $(dE/dx)^2$ dependence of the ergosterol M^+ yields, but not the Cs^+ data, which are rather well explained by the thermalized ion explosion model (Seiberling et al. 1981). The thermalized ion explosion model, case I $S \propto (dJ/dx)^4$ fits the $Y(Cs^+$ by ^{16}O ions) very well. It also fit $Y(Cs^+)$ with ^{32}S, ^{63}Cu, and ^{127}I. However, it does not correctly fit the yield ratios for Y(I)/Y(Cu), Y(I)/Y(S), and Y(I)/Y(O). Case II of the thermalized ion explosion gives good predictions for these yield ratios for ergosterol and CsI, but does not fit the velocity dependence as well as $(dJ/dx)^4$. The case II gives a sputtering spike temperature of 9.6×10^4K. Thus we have a similarity between the Cs data and the UF_4 data, both of which seem to do well when plotted vs $(dJ/dx)^4$.

Hakansson and coworkers (1981b) have also measured the yields of these biomolecules as a function of the angle of incidence of the beam. Suppose we assume that for a tilted beam arrangement, the surface energy goes as $1/\cos\vartheta$. Recall that the results were a $1/\cos\vartheta$ dependence for Cs, glycylglycine, and high dE/dx ions on ergosterol. Less heavily ionizing particles on ergosterol gave a $1/\cos^2\vartheta$ dependence. The $1/\cos\vartheta$ dependence for the yield could be explained by case II of the thermalized ion explosion model. The $1/\cos^2\vartheta$ distribution applies to the Coulomb explosion and the thermal pulse model of Sigmund and Claussen.

The only model that incorporates both the ergosterol and CsI data is case II of the thermalized ion explosion model where T is allowed to increase with dJ/dx. This leads to high spike temperatures which, we must remember, contradicts the results of Duck et al. (1980a, 1980b), who find energy distributions of the desorbed particles which are independent of LET. It may be that the mechanism for CsI and ergosterol

are different. The remarkable result is the difference between the angular dependences for ergosterol and glycylglycine.

The charge state dependence of the yields of CsI, glycylglycine, and ergosterol with 20 MeV (+2-+8) beams was quite pronounced. They claim that the results on ergosterol are not in disagreement with $(dE/dx)^2 \rightarrow q^4$ dependence. Meins (1981b) has applied the formula of Griffith (Seiberling et al. 1981) to these results and gets a good fit with $\lambda_s/\lambda_z = 2$ (for 20 MeV ^{16}O ions. The Ziegler value for the equilibrium charge state of these ions is 6.46.)

5. Frozen volatiles

Other groups have measured the erosion of frozen volatiles with high energy ion beams. The Chalk River group has looked at xenon sputtering with He, N, and Ar beams (Ollerhead et al. 1980). They claim that a Coulomb explosion model cannot explain the observed temperature and thickness dependence. Rather, they invoke a thermal spike model to explain their data, but the details of how the energy is transferred from the electrons to the atoms are vague.

Besenbacher et al. (1981) have measured the yield for He ions on frozen argon. They see a $(dE/dx)_e^2$ dependence on the yield. Even though the ion explosion model predicts a $(dE/dx)^2$ dependence for the sputtering yield (Haff 1976, Brown et al. 1980a), they argue that the ion explosion model is not applcable to argon sputtering. They calculate, using the electron mobility of argon, the time it takes for an electron to neutralize the ions along the initial track. They also calculate the time, t_{Coul}, the time it takes for an ion to recoil under mutual Coulomb repulsion from a neighboring ion. They find that $t_{neut} \sim t_{Coul}$, which makes the ion explosion model seem less attractive. They also argue that the ion explosion model

will not account for the observed thickness dependence and the fact that there were no high ion yields observed in the sputtering.

They seem to prefer the thermal pulse model of sputtering (Sigmund and Claussen 1980). This model also predicts that $Y \propto F_D^2$, where F_D is related to dE/dx, and represents the energy available for the kinetic energy of the atoms around the track. They do acknowledge, however, that there are still problems associated with explaining how the heat is transferred from the electrons to the atoms. They assume that $\langle r_o^2 \rangle \propto F_D$, so that the radius of the spike changes to maintain a constant T.

$$kT_o = \frac{F_D}{2\pi N \langle r_o^2 \rangle}$$

They assume an initial radial distribution of deposited electronic energy with a time delay before the energy is available as heat and evaporation can occur. (This is similar to an assumption made by Van Vechten (1980a, 1980b) relating to laser annealing).

Besenbacher and coworkers argue that the thermalized ion explosion model (Seiberling et al. 1980) will not work because of difficulties associated with the time scales (see above). Nor will a collisional heating mechanism by excited e^- work, again because of time scales. They conclude by saying that the main question is to evaluate F_D, both to understand what fraction of $dE/dx)_e$ contributes to sputtering, and the mechanism of transfer of the energy from the electrons to the atomic system.

6. Other insulating materials

Qiu et al. (1981) have studied sputtering by high energy Cl ions incident on Al_2O_3 and $LiNbO_3$ targets and find a clear dependence on the

electronic stopping power. The recent results of Qiu et al. on the sputtering of Al_2O_3 and $LiNbO_3$ with Cl ions are surprising in that the yields of Al and Nb atoms are nearly equal. Offhand, these two materials are very different. $LiNbO_3$ is a much softer material than Al_2O_3, and has a thermal diffusivity that is nearly 10 times smaller than that for Al_2O_3. One would expect that the sputtering yield of $LiNbO_3$ would be much larger. This is also a prediction of the thermalized ion explosion model. ($LiNbO_3$ is also known to have a track registration threshold whereas Al_2O_3 does not.) Recall that we had some difficulties earlier in this chapter trying to make the relevant time scales for the thermalized ion explosion model work for ice.

A further interesting test of the dependence of the yield on the thermal diffusivity would be to sputter amorphous and crystalline quartz targets. They have thermal diffusivities which differ by a factor of 9 at room temperature, and a factor of 5 at 150°C. With 20 MeV Cl (equilibrated before the target to a charge state of ~ 9.9), they saw no significant difference between the yields from amorphous and crystalline samples. These yields were about ten times larger than those observed on Al_2O_3 (Qiu 1981).

VI. Conclusion

As we have seen in chapters IV and V, several authors have proposed models to explain the mechanism for dielectric sputtering. One of the main unsolved problems is how to account for the fact that energy deposited by the high energy ion into the electronic system of the solid is transferred to kinetic energy of the target atoms.

One would like to design experiments that can help distinguish between the different models. Ideally, experiments shoud be able to vary one parameter at a time. For example, the electrical conductivity of ice can be changed by doping with chemicals like HF and HCl. This has been demonstrated to be true for crystalline ice (Klinger 1972), which would be difficult to work with in the present experimental arrangement. It is not clear what effect doping would have on the properties of amorphous ice.

Other sorts of measurements would also be very useful in trying to sort out the mechanism of enhanced sputtering. Certainly, experiments to measure the energy spectra of the sputtered ice particles would be very informative. Again, these experiments are difficult to perform. H_2O is a fairly light molecule which makes TOF spectroscopy difficult.

A. Related Fields of Research

It is also useful to examine experiments from other fields which may help to shed light on different aspects of the sputtering process. An area that comes immediately to mind is to study electron and photon bombardment of ice or another dielectric target. Electrons and photons would excite the electrons of the solid without also suffering collisions with the solid atoms themselves and creating structural changes in the solid via the nuclear collisions, which at present do not interest us. Both Chalk River (Ollerhead *et al.* 1980) and Bell Labs have used electrons to

sputter ice and xenon respectively, but no extensive studies have been made. They both found that the yields from the electron bombardment were very small.

It may also be useful to examine the process from another point of view. Insead of observing the particles that leave the surface of the target, perhaps useful information may be gained from studying the detailed structure of the material left behind after the sputtering has occurred. Areas of research that are concerned with the detailed structure of the material left behind after damage by radiation fields include laser and electron induced annealing, and the formation of tracks in dielectric materials. The relationship between track formation and sputtering is has been speculated about by many people (Haff 1976, Griffith 1979). One can only guess what the connections between annealing and sputtering are, if indeed they exist.

It is known that electrons produce annealing similar to laser beams. It is believed by many that the annealing processes induced by electrons and lasers resemble one another in that, ultimately, they both produce heat (von Allmen 1980). However, the coupling mechansims for electrons and photons to the solid differ. Electrons undergo two types of collisions, nuclear and electronic. If they are energetic enough, they can displace atoms from their lattice sites; otherwise, the nuclear collisions only cause a change in direction of the e^-. In collisions with other electrons, presumably they excite these electrons which subsequently thermalize and recombine in similar processes to those following light absorption.

Let us examine the effect of intense photon irradiation of materials. Several authors attribute laser annealing of amorphous Si to a mechanism involving nothing more than simple thermal melting, rapid

crystallization, and quench (STMR model). Van Vechten and Soviet authors claim that there is ample evidence in acoustic, optical, elastic and structural data from laser annealing of Si to support the idea of a non-thermal annealing process, plasma annealing, PA. For example, Si wafers may be fractured by μs or 100 μs laser pulses that do not raise the surface temperature higher than 200°C (mp ~1685 K). The proponents of the non-thermal model must explain how the annealing occurs and how the energy stays in the electronic system (without converting to heat) long enough for a non-thermal process to occur (Van Vechten 1980a, 1980b).

The covalent bonding of both amorphous and crystalline Si is due to electrons near the top of the valence band. If these are excited across the gap, the covalent bonds are weakened. If a high enough density of carriers ($>2\times10^{19}/cm^2$) are excited across the gap, the lattice will become unstable and the material will become fluid. In this configuration, the temperature of the electrons will be greater than the temperature of the lattice, thus making the PA fluid state very different from a normal fluid. Van Vechten claims that this difference may account for experimental results which are in contradiction to a theory of normal melting. Recrystallization occurs when the plasma density falls slowly (if it falls too quickly, the final phase will be amorphous) (Van Vechten 1980a, 1980b). These ideas are not unlike the ones C.C. Watson (1981) is considering related to enhanced sputtering of dielectrics after electronic excitation by ion beams. We do have some evidence that the ice undergoes a major structural change, after bombardment by ion beams. At Bell Labs, transparent films of ice have been observed to turn frosty after ion beam bombardment. This presumably is a change from amorphous structure

to polycrystalline.

Enhanced migration of interstitials and vacancies would contribute to the nonfluid annealing. Van Vechten (1981a) asserts that a sufficiently hot dense electron hole plasma would minimize Coulomb trapping of vacancies and interstitial diffusion.

Lasers have been used to induce desorption of biomolecules. Kistemacker and coworkers at FOM (Posthumus et al. 1978) used CO_2 lasers and neodymium glass lasers and got spectra similar to SIMS and HIID. In desorbing large molecules, a short laser pulse is important. They claim this is a confirmation of rapid sample heating. The mechanism for this desorption is not understood. More work is being done at Frankfurt. They have published comparisons of mass spectra obtained by lasers, low energy ions, and high energy ions (Krueger and Schueler 1979, Schueler and Krueger 1979).

We also know that in the production of tracks in solids, there is a rearrangement of crystal structure along the track. After bombardment of insulating materials by sufficiently highly ionizing particles, these materials can be etched, with the result that material is preferentially removed from the track of the incident ion. This is evidence of a structural change along the track. Presumably, the process of track production is related to enhanced sputtering of dielectrics. This connection has been seen in $LiNbO_3$, which is known to register tracks for $(dE/dx)_e >$ 18.5MeV/(mg/cm^2) (Qiu et al. 1981), and in SiO_2. Tracks have been searched for in ice and not seen (Macarthur 1979). It is not clear that this is due to the absence of tracks or to the difficulties in working with ice samples that have made them difficult to detect. Tracks have also been looked for in Al_2O_3 and UF_4 (Griffith 1981) and not seen. Again, it is

not known whether these materials form tracks or whether the problem is that the appropriate etching material has not been found.

Fleischer *et al.* (1965) proposed the ion explosion model of track formation which prompted Haff (1976) to suggest the ion explosion model of dielectric sputtering.

Dartyge *et al.* (1981) have proposed a new model for track formation in dielectrics. Previous models (reviewed by Fleischer 1980) were based on the necessity of sufficiently high concentrations of defects produced near the end of the particle's range, or with sufficiently high primary ionization or rate of energy loss (above a critical level). This critical level depends on the mineral being bombarded. The latent track is much more chemically active than the surrounding material. However, such models do not account for certain features of the experiments, such as complex shapes of track length distributions. All tracks formed at a given energy should have the same length. A model of track formation has been proposed which depends on the detailed distribution of defects produced by the ion travelling through the dielectric material. Dartyge and coworkers (1981) claim that latent tracks are composed of extended defects separated by gap zones loaded with point defects. The variation of the concentration of extended defects along the path of the ion does not vary with functions such as the primary rate of ionization. These two regions of defects (extended and point) do not behave the same under annealing and etching. The extended defects dominate the etching and annealing behavior of tracks. For a given incident ion, the concentration of extended defects appears to be similar in all silicates. This idea has been successfully applied to data to explain phenomena such as the observed distributions of etched track lengths.

The size of the extended defects is constant for incident ion energies varying from ~0.2MeV/amu to 10 MeV/amu. The size increases with Z of the incident ion. The production of point defects fits closely with dE/dx and dJ/dx variations. The distribution of extended defects does not. An interesting point to note is that in one of their graphs (Dartyge et al. 1981), the variation in the linear density of extended defects (derived from x-ray observations) of mica irradiated by Fe ions, scales approximately as the fourth power of dJ/dx.

The implication of this model is that it removes the restrictions of threshold dJ/dx or dE/dx on track formation. Rather, track formation will be dependent on the density of extended defects at the surface of the sample, which will, in turn, depend on the mechanism of their formation and statistical distribution along the track. If enhanced sputtering also depends on the formation of these extended defects, any calculation of the expected sputtering yield requires that we be able to calculate how energy is distributed to the atoms of the solid at the time of formation of the defects. While it is enticing to consider what parallels exist between the formation of tracks by high energy ions is solids, laser annealing, and enhanced sputtering, much work must be done before it can be said that the mechanisms involved in these processes are actually the same.

B. Applications of Enhanced Sputtering of Dielectrics

We proceed now to a brief discussion of the applications of enhanced sputtering in dielectric materials. The process may be important in astrophysical enviornments where frozen gas surfaces are bombarded by ions and electrons from the solar wind, cosmic rays, and planetary magnetospheres (Tombrello 1981). It is important whenever one has cryopumping in radiation fluxes, storage rings (Grobner and Calder 1973,

Fischer 1972), superconducting magnets and accelerators, and controlled thermonuclear research (Hinnov 1974)). Its uses extend to biology, as well. As we have seen, whatever the mechanism for HIID is, it desorbs large biomolecules non-destructively from the surfaces of the targets, which is difficult to do by other methods, and consequently is of importance to biological researchers (Macfarlane et al. 1976b, Hakansson et al. 1981a, 1981b, 1981c, Duck et al. 1981a, 1981b, Furstenau et al. 1977).

Since the ice sputtering results are most directly applicable to understanding astrophysical enviornments, we will elaborate somewhat on some of these calculations to illustrate the variety of phenomena in which enhanced sputtering plays a role. Astrophysical enviornments where ice sputtering is important include planetary surfaces, ring systems, comets, and interstellar grains.

As an illustration of these processes, consider the Jovian satellite system. Io (5.90 R_J=Jovian radii) is covered with SO_2 frost, Europa (9.40 R_J)has H_2O frost on the trailing side, Ganymede (14.99 R_J) is 65% H_2O frost on the leading side, and Callisto (26.33 R_J) has 20-30% H_2O frost on the leading side (Stone and Lane 1979). The Jovian magnetosphere extends 50 R_J on the dayside of the planet and 2 AU on the nightside. This means that the satellites are imbedded in the radiation flux trapped in Jupiter's magnetosphere. They are in synchronous orbit around Jupiter, which rotates faster than the satellites. This says that the trailing sides of the satellites will be bombarded by particle fluxes (Cowly 1980).

On Io, sputtering may contribute to the creation of an atmosphere. The neutral sputtered particles leave the surface of the planet with an energy distribution that depends on details of the sputtering process. If they are energetic enough, they will leave the surface of the planet

altogether. Less energetic particles will have ballistic trajectories, spending some of their time in the atmosphere, and redistributing material on the surface of the planet. Particles that escape the surface contribute to the concentration of molecules and ions in the magnetosphere (Haff et al. 1981, Matson et al. 1974).

Europa has a relatively featureless surface. It has been estimated that up to 10's of m to a km of ice may have been sputtered from its surface, demonstrating that sputtering may be important in developing the surface topography of a planet (Lanzerotti et al. 1978b, Smith et al. 1979).

Ganymede has a peculiar distribution of craters with a concentration of dark-rayed craters on the trailing side of the planet (Conca 1981). Callisto has a very low surface albedo, although it is believed to be covered with ice. Both of these phenomena may be due to sputtering of a surface which consists of an ice matrix in which silicate (or other material) particles are imbedded (Haff et al. 1979, Haff 1980). If the ice sputters off preferentially, the surface of the planet will become "armor coated" with a layer of silicate which has a relatively low albedo. This, in turn, could alter the surface temperature of the planet, which has consequences for atmosphere production.

Sputtering of ice will also be of importance in ring systems, such as that around the planet Saturn. Saturn's rings are composed of ice particles ranging from 10's of cm's to meters. Sputtering may limit the lifetime of the outer particles of the rings, redistribution of material in the rings, and the production of an atmosphere around the rings (Cheng and Lanzerotti 1978). The observed hydrogen atmosphere may be H that is sputtered directly from the rings, or formed by photodissociation of

sputtered H_2O (Carlson 1980).

Interstellar grains are believed to be one of the major sites of molecule formation in the interstellar medium. There are several proposed mechanisms for ejecting molecules formed on their surfaces, the dominant one being UV desorption, except on pure ice grains (Watson 1972). For these grains, and for grains located inside clouds where the UV is shielded out, cosmic ray sputtering may be an important ejection or destruction method (Draine 1977). Similar effects may be expected on the ice grains that make up comets (Johnson 1981). Sputtering by solar wind and solar flare particles determines the lifetime of grains that have entered the solar system from comets or from the local interstellar medium (Lanzerotti et al. 1978a, Johnson et al. 1981).

In conclusion, the principal reason for undertaking these sputtering measurements was to understand the mechanism involved in the sputtering of dielectrics. Many models have been proposed to explain results found from sputtering different kinds of insulating targets. These models have met with varying degrees of success when applied to different subsets of the experimental data. Ultimately, it becomes a problem of understanding the transfer of energy from the electrons to the atoms of a solid after the passage of a high energy ion that excites the electrons.

Apart from the mechanism, there are several areas of applications for the results. It would be of obvious importance to calcuations in these areas were we to understand the mechanism responsible for the enhanced sputtering. Understanding the mechanism of enhanced sputtering may also have implications for the understanding of track formation and defect production by ions in solids, and for laser and electron induced annealing of solids.

Appendix A

The sputtering yield may be calculated using the formula

$$S = \frac{(\Delta AuC)(\beta)(1/\varepsilon)(A)}{(Q_{sputt}/q)(1/e)}$$

(see chapter III, section B) This formula is certainly valid when the depth profile of the sputtered crater is regular; that is, the ice layer remaining on the target is of uniform thickness. The following derivation justifies the use of this formula to calculate S fpr the case when the sputtered ice layer is uneven, as it most probably is.

Examine the numerator of this equation. Assuming uniform irradiation of the whole crater by the analysis beam, the number of water molecules removed from the ice layer is given by

$$(\Delta AuC)(\beta)(1/\varepsilon)(A)$$

ΔAuC= channels (the shift in the gold centroid before and after sputtering)

β = eV/channel

$1/\varepsilon$ = $(10^{15} H_2O/cm^2)/eV$

A = cm^2

Now suppose that the ice crater has an uneven bottom. Divide the cross-sectional area of the crater into several smaller areas, such that each of these smaller pieces is of uniform depth. This is equivalent to irradiating each small area of the target, a_i, and summing up the spectra to give a complete profile of the whole area, A, of the crater.

$$A = a_1 + a_2 + \ldots\ldots\ldots + a_n$$

If C_o is the centroid of the gold peak before sputtering, then

$$C_o = \frac{\sum_a^b c_i n_{oi}}{\sum_a^b n_{oi}}$$

where

c_i = channel number i

n_{oi} = number of counts in channel i of initial ice spuctrum

The centroid after sputtering, C_f,

$$C_f = \frac{\sum_a^b c_i n_{fi}}{\sum_a^b n_{fi}}$$

The number of water molecules removed from area A is the sum of the number removed from each of the smaller areas, a_i. Therefore, we want to show that

$$(\Delta AuC)A = (\Delta AuC)_1 a_1 + (\Delta AuC)_2 a_2 + \ldots\ldots\ldots + (\Delta AuC)_n a_n$$

where $(\Delta AuC)_i$ = (centroid after sputtering) - (centroid before sputtering) measured on a_i of the target.

$$(\Delta AuC)_1 a_1 + (\Delta AuC)_2 a_2 + \ldots\ldots + (\Delta AuC)_n a_n$$

$$= \left[\frac{\sum_a^b n_{1i} c_i}{\sum_a^b n_{1i}} - \frac{\sum_a^b n_o c_o}{\sum_a^b n_o} \right] a_1 + \ldots\ldots \left[\frac{\sum_a^b n_{ni} c_i}{\sum_a^b n_{ni}} - \frac{\sum_a^b n_o c_o}{\sum_a^b n_o} \right] a_n$$

where n_{ki} = number of count in channel i from irradiation of area k of the target

We have assumed uniform irradiation of the target by the beam. For uniform irradiation of the target by the analysis beam (ignoring changes in $d\sigma/d\Omega$ due to differing ice thicknesses - a small effect for ^4He particles)

$$\sum_a^b n_{ki} = \frac{a_k}{A}\sum_a^b n_i$$

Therefore,

$$(\Delta Au C)_1 a_1 + (\Delta Au C)_2 a_2 + \ldots + (\Delta Au C)_n a_n$$

$$= \left[\frac{\sum_a^b n_{1i} c_i}{a_1 / A \sum_a^b n_{fi}} a_1 + \frac{\sum c_i}{n_{2i} \quad a_2 / A \sum_a^b n_{fi}} a_2 + \ldots\ldots + \frac{\sum_a^b n_{ni} c_i}{a_n / A \sum_a^b n_{fi}} a_n \right]$$

$$- \left[\frac{\sum_a^b n_o c_i}{\sum_a^b n_o} \right] (a_1 + a_2 + \ldots\ldots + a_n)$$

$$= \left[\sum_a^b \frac{\sum_a^b n_{1i} c_i + \sum_a^b n_{2i} c_i + \ldots\ldots + \sum_a^b n_{ni} c_i}{\sum_a^b n_{fi}} \right] A - \left[\frac{\sum_a^b n_o c_i}{\sum_a^b n_o} \right] A$$

$$= \left[\frac{\sum_a^b n_{fi} c_i}{\sum_a^b n_{fi}} - \frac{\sum_a^b n_o c_i}{\sum_a^b n_o} \right] A$$

$$= (\Delta Au C) A$$

We conclude that, even in the case of an irregularly shaped crater in the ice, we can find the number of H_2O molecules sputtered from the

target by measuring the shift in the gold centroid by using uniform irradiation of the sputtered crater with the He analysis beam.

Appendix B

Here we give some useful physical properties of H_2O.

mass of a H_2O molecule = 3.01×10^{-23}gm

enthalpy of formation (0°K) = 9.510 eVu

enthalpy of formation (25°C) = 9.606 eV

sublimation of ice at 0°K = 0.49 eV

hydrogen bond energy = 0.29 eV

latent heat of melting = 0.06 eV

latent heat of vaporization = 0.39 eV

H-O-H to H + O-H = 5.11 eV

O-H to O + H = 4.40 eV

These data were taken from Hobbs (1974).

A density of 1 gm/cm^3 corresponds 3.32×10^{22} molecules/cm^3. The lattice spacing for amorphous ice of this density is 3.7Å.

Here we list the ground state energies of H_2O molecules as given by Fletcher (1970). The numbers listed here are the results of calculations; experimental values are listed in parentheses next to the calculated values.

-11.79 (-12.6 ±0.1); -13.20 (-14.5 ±0.3); -18.55 (-16.2 ±0.3); -37.19; -557.3 eV.

Graphs of the thermal conductivity of polycrystalline ice may by found in Fletcher (1970, p. 144); the heat capacity of polycrystalline, crystalline, and amorphous ice is given in Sugisaki (1968); the thermal dffusivity has been calculated from these data and is shown in figure 5a.

REFERENCES

Anderson, H. H. and Ziegler, J. F., 1977, **Hydrogen Stopping Powers and Ranges in All Elements** (Pergamon Press, New York).

Besenbacher, F., Bottiger, J., Graversen, O. and Sorensen, H., 1981, to be published.

Bethe, H., 1930, Ann. Physik. **4,** 443.

Bevington, P. R., 1969, **Data Reduction and Error Analysis for the Physical Sciences** (McGraw-Hill Book Company, New York).

Biersack, J. P. and Santner, E., 1976, Nucl. Instr. and Meth. **132,** 229.

Brown, W. L., Augustyniak, W. M., Brody, E., Cooper, B., Lanzerotti, L. J., Ramirez, A., Evatt, R. and Johnson, R. E., 1980a, Nucl. Instr. and Meth. **170,** 321.

Brown, W. L., Augustyniak, W. M., Lanzerotti, L. J., Johnson, R. E. and Evatt, R., 1980b, Phys. Rev. Lett. **45,** No 20, 1632.

Carlson, R. W., 1980, Nature **283,** 461.

Cheng, A. F. and Lanzerotti, L. J., 1978, J. Geophys. Res. **83,** 2597.

Chu, W. K., Mayer, J. W. and Nicolet, M.-A., 1978, **Backscattering Spectrometry** (Academic Press, New York).

Conca, J., 1981, Proc. Lunar Planet. Sci. Conf. **12,** in press.

Cowly, S. W. H., 1980, Nature **287,** 775.

Dartyge, E., Duraud, J. P., Langevin, Y. and Maurette, M., 1978, Proc. Lunar Planet. Sci. Conf. **9,** p. 2375.

Dartyge, E., Duraud, J. P., Langevin, Y. and Maurette, M, 1981, submitted to Radiation Effects

De Heer, F. J., Schutten, J. and Moustafa, H., 1966, Physica **32,** 1766.

Duck, P., Treu, W., Galster, W., Frohlich, H. and Voit, H., 1980a, Nucl. Instr. and Meth. **168,** 601.

Duck, P., Treu, W., Frohlich, H., Galster, W. and Voit, H., 1980b, Surface Science **95,** 603.

Draine, B. T., 1977, CRSR 669 (Center for Radiophysics and Space Research, Cornell University, Ithaca, New York)

Fischer, E., 1972, J. Vac. Sci. Technol. **9,** 1203.

Fleischer, R. L., Price, P. B. and Walker, R. M., 1965, J. Appl. Phys. **36,** 3645.

Fleischer, R. L., Price, P. B. and Walker, R. M., 1975, **Nuclear Tracks in Solids** (University of California Press, Berkeley), pp. 11, 30-31.

Fleischer, R. L., 1980, in "Progress and material sciences", in press.

Fletcher, N. H., 1970, **The Chemical Physics of Ice,** (University Press, Cambridge).

Furstenau, N. H., Knippelberg, W., Krueger, F. R., Weiβ, G. and Wien, K., 1977, Z. Naturforsch. **32a,** 711.

Griffith, J. E., 1979, Ph.D. Thesis, California Institute of Technology

Griffith, J. E., Weller, R. A., Seiberling, L. E. and Tombrello, T. A.,

1980, Rad. Eff. **51,** p 223.

Griffith, J. E., 1981, private communication.

Grobner, O. and Calder, R. S., 1973, IEEE Trans. Nucl. Sci. **20,** 760.

Haff, P. K., 1976, Appl. Phys. Let. **29,** 443.

Haff, P. K., Watson, C. C. and Tombrello, T. A., 1979, Proc. Lunar Planet. Sci. Conf. **10,** 1685.

Haff, P. K., 1980, in J. E. E. Boglin and J. M. Poate (eds.) Proc. on Thin Film Interfaces and Interactions, The Electrochemical Society, Princeton, N. J., **80-82,** 21.

Haff, P. K., Watson, C. C. and Yung, Y. K., 1981, J. Geophys. Res. in press.

Hakansson, P. and Sundqvist, B., 1981a, TLU 77/80, Tandem Laboratory Report (Uppsala, Sweden).

Hakansson, P., Kamensky, I. and Sundqvist, B., 1981b, TLU 78/80, Tandem Laboratory Report (Uppsala, Sweden).

Hakansson, P., Jayasinghe, E., Johansson, A., Kamensky, I. and Sundqvist, B., 1981c, TLU 83/81, Tandem Laboratory Report (Uppsala, Sweden).

Heckman, H. H., Hubbard, E. L. and Simon, W. G., 1963, Phys. Rev. **129,** 1240.

Hinnov, E., 1974, Proc. Conf. on Surface Effects in Controlled Thermonuclear Devices and Reactors, Argonne, Ill., 1974.

Hobbs, P. V., 1974, **Ice Physics** (Clarendon Press, Oxford).

Kelly, R., 1979, Surface Science **90,** 280.

Klinger, J., 1972, in E. Whaller, S. J. Jones and L. W. Gold (eds.)

Physics and Chemistry of Ice, Symposium on the Physics and Chemsitry of Ice, Ottowa, 1972 (Royal Society of Canada, Ottowa, 1973), p. 711.

Krueger, F. R., 1977, Z. Naturforsch. **32a,** 1084.

Krueger, F. R. abd Wien, K., 1978, Z. Naturforsch. **33a,** 638.

Krueger, F. R. and Schueler, B., 1979, Proc. from 8th Int. Mass Spectra Conf., Oslo 1979.

Landauer, J. K. and Plumb, H., 1956, SIPRE Res. Rep. **16,** 4.

Lanzerotti, L. J., Brown, W. L., Poate, J. M. and Augustyniak, W. M., 1978a, Geophys. Res. Lett. **5,** 155.

Lanzerotti, L. J., Brown, W. L., Poate, J. M. and Augustyniak, W. M., 1978b, Nature, **272,** 431.

Lindhard, J., Nielson, V. and Scharff, M., 1968, Mat. Fys. Medd. Dan. Vid. Selsk. **36,** No. 10.

Macarthur, B., 1979, private communication.

Macfarlane, R. D. and Torgerson, D. F., 1976a, Phys. Rev. Lett. **36,** No. 9, 486.

Macfarlane, R. D. and Torgerson, D. F., 1976b, Intl. J. of Mass Spectrometry and Ion Physics **21,** 81.

Mann, F. M., 1975, Ph.D. Thesis, California Institute of Technology

Marion, J. B. and Young, F. C., 1968, **Nuclear Reaction Analysis**

(American Elsevier Publishing Company, Inc., New York), p. 34.

Matson, D. L., Johnson, T. V. and Fanale, F. P., 1974, Ap. J. **192** p. L43.

Matteson, S., Chau, E. K. L. and Powers, D., 1976, Phys. Rev. A **14,** No. 1, 169.

Matteson, S., Powers, D. and Chau, E. K. L., 1977, Phys. Rev. A **15,** No. 3, 856.

Matteson, S. and Nicolet, M.-A., 1979, Nucl. Instr. and Meth. **160,** 301.

Meins, C. K., 1981a, Ph.D. Thesis, California Institute of Technology.

Meins, C. K., 1981b, private communication.

Mott, N. F. and Massey, H. S. W., 1965, **The Theory of Atomic Collisions,** (Clarendon Press, Oxford).

Northcliffe, L. C., 1960, Phys. Rev. **120,** 1744.

Northcliffe, L. C. and Schilling, R. F., 1970, Nuclear Data Tables **A7,** pp. 233-463.

Olander, D. S. and Rice, S. A., 1972, Proc. Nat. Acad. Sci. USA, **69,** No. 1, 98.

Ollerhead, R. W., Bottiger, J., Davies, J. A., L'Ecuyer, Haugen, H. K. and Matsumani, N., 1980, Rad. Eff. **49,** p 203.

Posthumus, A., Kistemacker, P. G., Meuzelaar, H. L. C. and Ten Noeverde Braun, 1978, Anal. Chem. **50,** 7, 985.

Qiu, Y., Griffith, J. E. and Tombrello, T. A., 1981, submitted to

Radiation Effects.

Qiu, Y., 1981, private communication.

Roth, A., 1976, **Vacuum Technology** (North-Holland Publishing Company, Amsterdam).

Schram, B. L., De Heer, F. J., van der Wiel, M. J. and Kistemaker, J., 1965, Physica **31,** 94.

Schueler, B. and Krueger, F. R., 1979, Org. Mass Spectr. **14,** 8, 439.

Seiberling, L. E., Griffith, J. E. and Tombrello, T. A., 1980, Rad. Eff. **52,** 201.

Seiberling, L. E., Meins, C. K., Cooper, B. H., Griffith, J. E., Mendenhall, M. H. and Tombrello, T. A., 1981, submitted to Nucl. Instr. and Meth.

Sigmund, P., 1969, Phys. Rev. **184,** No. 2, 383.

Sigmund, P., 1972a, Rev. Roum. Phys, **17,** 823.

Sigmund, P., 1972b, Rev. Roum. Phys. **17,** 969.

Sigmund, P., 1977, in N. H. Tolk and J. C. Tully (eds.), **Inelastic Ion-Surface Collioions** (Academic Press, Inc., New York), p. 121.

Sigmund, P. and Claussen, C., 1980 in P. Varga, G. Betz and F. P. Viehbock (eds.), Proc. of the Symp. on Sputtering, April 1980, Perchtoldsdorf, Austria (Institut fur Allgemeine Physik, Technische Universitat, Wien, Austria).

Sigrist, A. and Balzer, R., 1977, Helv. Phys. Acta. **50,** 49.

Smith, B. A., Soderblom, L. A., Beebe, R., Boyce, J., Briggs, G., Carr, M.,

Collins, S. A., Cook II, A. F., Davidson, G. E., Davis, M. E., Hunt, G. E., Ingersoll, A., Johnson, T. V., Masursky, H., McCaulley, J., Morrison, P., Owen, T., Sagan, C., Shoemaker, E. M., Strom, R., Suomi, V. and Veverka, J., 1979, Science **206,** 927.

Sofield, C. J., Cowern, N. E. B., Draper, J., Bridwell, L., Freeman, J. M., Wood, C. J. and Spencer-Harper, M., 1980, Nucl. Instr. and Meth. **170,** 257.

Stiegler, J. and Noggle, T. S., 1962, J. Appl. Phys. **33,** 1984.

Stone, E. C. and Lane, A. L., 1979, Science **206,** 925.

Sugisaki, M., Suga, H. and Seki, S., 1968, Bull. of the Chem. Soc. of Jap. **41,** 2591.

Tombrello, T. A., 1981, submitted to Radiation Effects.

Van Vechten, J. A., 1980a, in C. W. White and P. S. Peercy (eds.) **Laser and Electron Beam Processing of Materials** (Academic Press, Inc., New York), p. 53.

Van Vechten, J. A., 1980b, Journal de Physique, Tome **41,** Colloque c4, supplement au n°5, p. c4-15.

Vineyard, G. H., 1976, Rad. Eff. **29,** 245.

von Allmen, M., 1980, in C. W. White and P. S. Peercy (eds.) **Laser and Electron Beam Processing of Materials,** (Academic Press, Inc., New York), p. 6.

Watson, W. D. and Salpeter, E. E., 1972, Ap. J. **174,** 321.

Watson, C. C., 1981, private communication.

Weast, R. C. (ed.), 1968, **Handbook of Chemistry and Physics** 49th

edition (The Chemical Rubber Co., Cleveland), p. E-71.

White, G. K., 1959, **Experimental Techniques in Low-Temperature** Physics (Clarendon Press, Oxford), p. 184.

Wittkower, A. B. and Betz, H. D., 1973, Atomic Data **5,** p. 113.

Ziegler, J. F., Chu, W. K. and Feng, J. S.-Y., 1975, Appl. Phys. Lett. **27,** No. 7, 387.

Ziegler, J. F., 1977, **Helium Stopping Powers and Ranges in All Elemental Matter** (Pergamon Press, New York).

Ziegler, J. F., 1980, **Handbook of Stopping Cross Sections for Energetic Ions in All Elements** (Pergamon Press, New York).

Table A

Here we present the experimental parameters used for each of the measurements of the erosion of H_2O(solid) by ^{19}F ions. In table A we have labelled the runs a-m. Each of these labels corresponds to a different ice target. On any given ice target, several measurements were made at different vertical positions of the detector. Table A is divided into four parts.

Ice Parameters: For each measurement we give the length of time the water line was open to the UHV chamber and the maximum pressure, in μa, achieved during target deposition as measured by the ion pump ($p=3\times10^{-8}$i). Also shown are the initial ice thicknesses at each spot, and the ice thickness removed during each sputtering run. The first four entries under each run, a-m, represent the four sputtered spots for that target, and the following entries under each run represent the unsputtered control spots for that target (chapter IV section C-1). All ice thicknesses are given in units of $10^{16}H_2O/cm^2$.

Beam Parameters: In this section, we give the ^{19}F beam current parameters used in the sputtering runs. The current is given in (nano-amps)/(incident charge state), and the F sputtering dose is given for each measurement. Also shown in this part of the table are the results of three checks on the beam integration. The first, ΣAu, gives the deviation (for each run a-m) between the calculated and measured sizes of the gold peak obtained by scattering the He beam from the bare target. The number shown under each run represents the maximum deviation measured for that target. Recall that several spots on a given target were measured. The second check, (He)/(F), compares the experimentally determined ratio of

the gold peaks, obtained by scattering He and F from the bare target, to the calculated ratio for this quantity. The last, ΣO, gives the agreement between the calculated and measured oxygen peaks of the new ice target (see chapter IV, section C-12).

Individual Sputtering Runs: All the sputtering measurements made, with ^{19}F incident on H_2O(solid), are listed as a function of the incident energy and charge state of the F beam, and the temperature of the target substrate. For the runs with no temperature listed, the target substrate was ~10K.

Averaged Sputtering Data: This part of the table gives the average value of S, calculated using the gold centroid and oxygen peaks, for all of the measurements taken with the same experimental conditions. See chapter IV, section B-1 for a list of which measurements were averaged together, and how the averaging was done. In parenthesis beside each of the average sputtering yield values, we give the experimental standard deviation for this set of measurements.

Run	Time(sec)	Ice Parameters Pressure (μa)	Initial Ice	Removed Ice
a	32	98	43.88(+16)	27.54(+16)
			49.94	30.01
			54.24	29.52
			56.20	27.32
				-2.77
				-1.26
				0
b	8,5	55,75	27.78(+16)	15.66(+16)
			33.41	16.58
			37.85	20.00
			37.43	18.25
				+0.28
				+0.17
				-0.22
c	59	82	56.24(+16)	31.29(+16)
			61.28	31.09
			66.34	37.40
			66.85	35.05
				-2.18
d	81	85	62.73(+16)	39.29(+16)
			71.11	37.30
			77.79	42.11
			79.59	42.38
				+2.02
				+2.02
				+2.02
e	65	86	57.29(+16)	25.65(+16)
			65.97	17.50
			72.63	28.66
			75.18	30.91
				+1.21
				+1.00
				+0.69
f	85	85	63.25(+16)	23.72(+16)
			71.64	23.77
			77.50	21.51
			81.88	?
				+0.45
				-0.16
				?
g	34	44	23.96(+16)	9.15(+16)
			28.32	10.89
			31.06	10.43
			32.56	13.56
				-0.28
				-0.36
				-0.69
h	105	90	51.62(+16)	28.16(+16)
			58.14	28.74
			64.73	31.88
			67.13	32.38
				+2.60

				-1.80
				-0.13
i	79	82	61.28(+16)	30.11(+16)
			71.98	30.52
			81.33	34.92
			84.52	34.92
				+0.05
				-0.70
				-2.79
j	81	83	63.68(+16)	50.63(+16)
			70.58	52.73
			78.05	59.37
			81.75	56.50
				-1.04
				-1.91
				-0.50
k	72	85	55.22(+16)	26.21(+16)
			65.59	27.38
			72.97	57.42
			75.69	50.58
				-2.72
				-1.17
				-2.16
l	61	86	55.38(+16)	33.49(+16)
			60.85	32.61
			68.68	42.53
			71.22	34.95
				+1.43
				+1.70
				+1.23
m	80	80	56.27(+16)	29.70(+16)
			64.64	31.60
			71.39	43.76
			74.66	43.26
				-0.90
				+0.13
				+0.99

Beam Parameters

Run	i_{sputt}	Q_{sputt}	ΣAu	(He)/(F)	ΣO
a	0.41	3.33(+12)	2%	9%	10%
	0.35	3.20		10%	
	0.35	3.10		10%	
	0.88	3.05		9%	
b	2.05	0.97(+12)	2%	0.7%	0
	0.59	0.98		0.4%	
	1.17	1.05		0.5%	
	1.2	1.05		0.2%	
c	1.6-2.7	1.96(+12)	2%	0.6%	12%
	1.2-1.6	1.91		0.5%	
	1.2-2.0	2.15		1%	
	1.2-1.6	2.03		1%	
d	0.78	2.27(+12)	2-5%	2%	12%
	1.6	2.20		2%	
	3.9-4.7	2.34		1%	
	1.6	2.29		3%	
e	1.6	2.97(+12)	0.7%	1%	2%
	1.6	1.41		1%	
	1.2	2.03		3%	
	1.6	2.62		0.4%	
f	1.2	1.68(+12)	2%	1.8%	16%
	0.78-1.2	1.71		0.4%	
	0.98	1.75		0.4%	
	0.98	1.76		2.7%	
g	0.39	0.99(+12)	3-6%	1.8%	4%
	1.2	1.02		2.7%	
	1.3	1.03		2.2%	
	3.1	1.08		1.4%	
h	1.2	2.10(+12)	4%	1.8%	7%
	1.2	2.08		0.9%	
	1.2	2.14		0.4%	
	1.2	2.22		0.4%	
i	0.98	1.98(+12)			
	0.98	2.02			
	0.59	1.96			
	0.29	1.94			
j	1.5	7.31(+12)	3%	1.4%	2%
	1.8-2.1	6.90		0.8%	
	1.8	7.02		1.4%	
	1.9	6.73		2.4%	
k	1.5	6.34(+12)	4%	10%	11%
	2.6	6.48		8%	
	0.15-0.29	6.21		7%	
	0.15-0.29	5.74		4%	
l	1.9-2.1	9.53(+12)	2%	6%	5%
	1.4	9.23		0.4%	
	1.6-2.1	11.20		5%	
	1.6-1.9	11.55		10%	
m	2.3-3.3	9.14(+12)			
	1.6-1.9	8.58			
	0.44	4.44			
	0.21	4.43			

Individual Sputtering Runs

Run	F energy (MeV)	Ch. state	T(°K)	S(AuC)	S(O)
a	1.6	+2		689	705
				781	764
				793	802
				746	735
b	5.0	+2		1343	1204
				1415	1393
				1590	1343
				1455	1251
c	6.0	+3		1330	1370
				1356	1481
				1449	1311
				1438	1483
d	7.5	+3		1441	1204
				1412	1219
				1499	1220
				1542	1293
e	10.0	+3		719	672
				1034	1010
				1176	1085
				983	848
f	10.0	+3	40	1176	985
			55	1158	882
			59	1018	927
			78	?	?
g	10.0	+3		771	741
				889	792
				844	581
				1046	993
h	10.0	+3	12	1117	990
			22	1151	1066
			40	1241	1121
			43	1215	932
i	10.0	+3		1267	1000
		+3		1259	972
		+4		1484	1238
		+6		1499	1505
j	15.0	+4		577	555
				637	642
				704	676
				699	680
k	20.0	+4		344	308
		+4		352	309
		+8		>770	>809
		+8		>734	>715
l	25.0	+5		293	276
				294	286
				316	279
				252	239
m	25.0	+5		271	230
		+5		307	284
		+8		821	721
		+8		813	808

Averaged Sputtering Data

F energy (MeV)	Ch. state	T(°K)	S_{avg} (AuC)	S_{avg} (O)	% Diff
1.6	+2	10	752(47)	752(41)	0
5.0	+2		1451(104)	1298(86)	11
6.0	+3		1393(59)	1411(85)	1.3
7.5	+3		1474(58)	1234(40)	18
10.0	+3	10	1021(183)	896(165)	13
10.0	+3	10-60	"	"	"
10.0	+4	10	1484	1238	
10.0	+6		1499	1505	
15.0	+4		654(60)	638(58)	2.5
20.0	+4		348(6)	309(1)	12
20.0	+8		>752(25)	>762(66)	1.3
25.0	+5		289(24)	265(25)	9
25.0	+8		817(6)	765(62)	

Table B

The rate of sublimation of ice is calculated using the following formula from Kelly (1979)

$$\varphi_{th} = \alpha p \frac{1}{(2\pi m k T)^{\frac{1}{2}}}$$

α = 1= sticking coefficient

p = equilibrium vapor pressure (Roth 1976)

m = 3.01×10^{-23}gm = mass of H_2O molecule

k = 1.381×10^{-16} erg/°K

T = °K

Rate of Sublimation of Ice

Temp(°K)	Vapor Pressure (torr)	φ_{th} [H_2O/(cm^{2}sec)]
90.15	1.4(-22)	0.122
123.15	7.4(-15)	5.5(+6)
133.15	2.9(-10)	2.07(+11)
143.15	7.0(-9)	4.81(+12)
153.15	1.1(-7)	7.53(+13)
163.15	1.3(-6)	8.07(+14)
173.15	1.1(-5)	6.89(+15)
183.15	7.5(-5)	4.54(+16)
193.15	4.1(-4)	2.43(+17)
203.15	2.0(-3)	1.15(+18)
213.15	8.1(-3)	4.58(+18)
223.15	2.9(-2)	1.60(+19)
233.15	9.7(-2)	5.24(+19)
243.15	2.9(-1)	1.53(+20)
253.15	7.8(-1)	4.04(+20)
263.15	2.0	9.91(+20)
273.15	4.6	2.29(+21)
283.15	9.2	4.51(+21)
293.15	1.8(+1)	8.45(+21)
323.15	9.3(+1)	4.24(+22)
373.15	7.6(+2)	3.24(+23)

Table C

Data on the sputtering yield S(U) of ^{235}U from UF_4 targets bombarded by energetic ^{19}F beams (table 10a from Griffith 1979).

Sputtering of UF_4 by ^{19}F ions

F Energy (MeV)	Charge state	S(U)	St dev
1.19	2	0.70	--
2.38	2	2.5	0.11
4.75	2	5.6	1.0
4.75	3	7.1	1.5
9.50	3	5.5	0.60
9.50	4	7.0	--
19.0	4	2.4	0.38
28.5	5	1.8	--

Figure 1a

Figure 1a shows the general dependence of the stopping power, dE/dx, as a function of the energy, E, of an ion travelling through matter. Sputtering phenomena are closely related to the stopping power; in particular, sputtering yields of different ion-target combinations tend to have maxima at the same energies as the nuclear and electronic stopping powers. Typically, the peak of the nuclear stopping occurs at an ion energy of approximately 1 keV/amu. The peak of the electronic stopping occurs at about 0.5MeV/amu. This schematic was taken from Sigmund (1977).

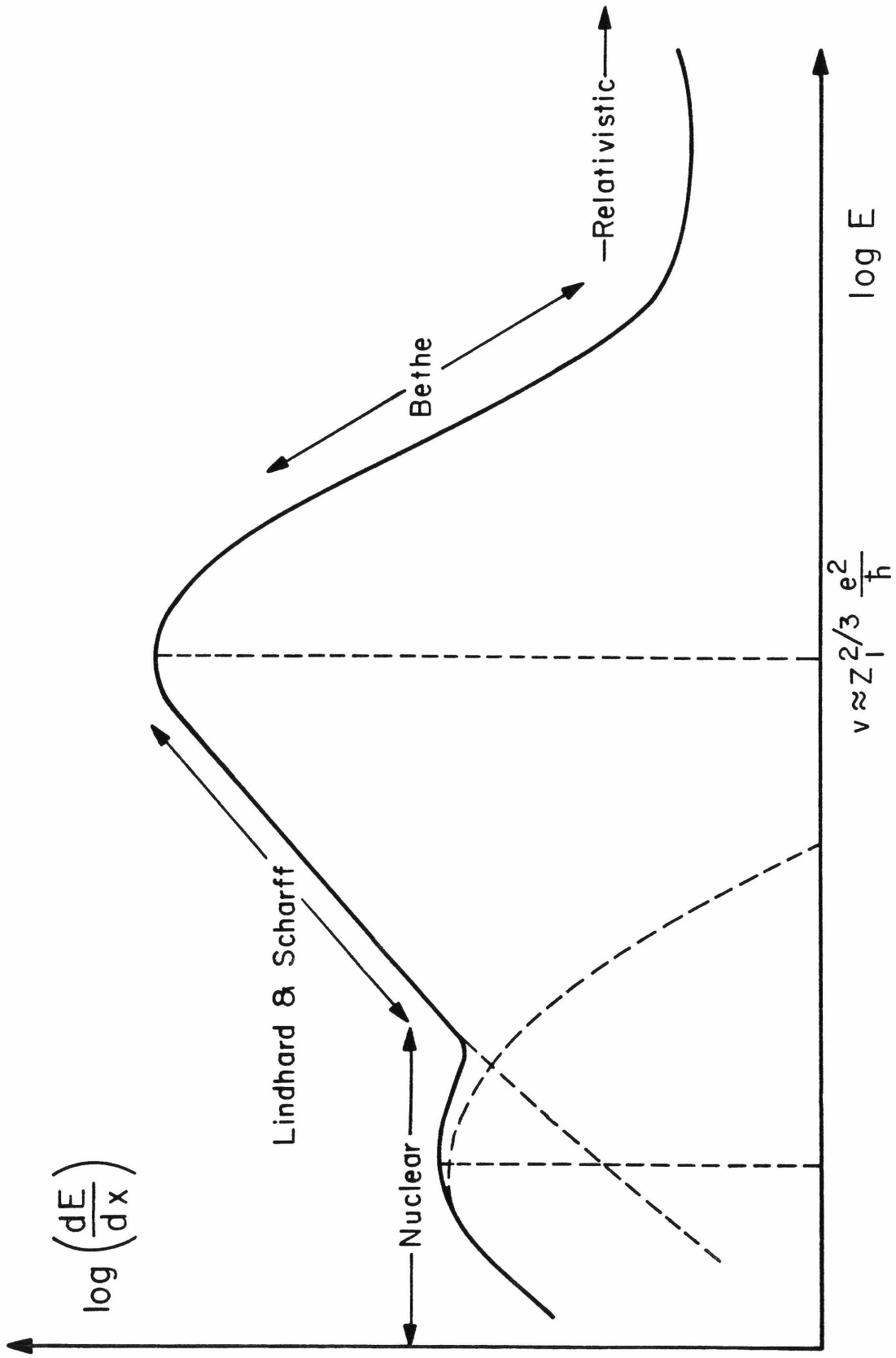
log (dE/dx)
Nuclear
Lindhard & Scharff
Bethe
Relativistic
log E
v ≈ Z1^2/3 e^2/ħ

Figure 2a

Figure 2a is a general schematic showing the layout of the accelerators. The ^{4}He beams were extracted from the JN, neutralized, injected into the tandem, stripped in the terminal, and energy selected with the 90° magnet. The ^{19}F beams were injected as negative ions into the tandem, stripped in the terminal, and energy analyzed with the 90° magnet. The electronics and magnetic focussing and steering elements of the accelerator are not shown.

After the 90° magnet, energy analyzed beams were deflected by the switching magnet into the beamline, which is equipped with magnetic quadrupoles and steerers. The UHV experimental chamber is isolated from the beamline by a liquid nitrogen cold trap.

For high charge state production, a foil stripper was used (just upstream of the 90° magnet).

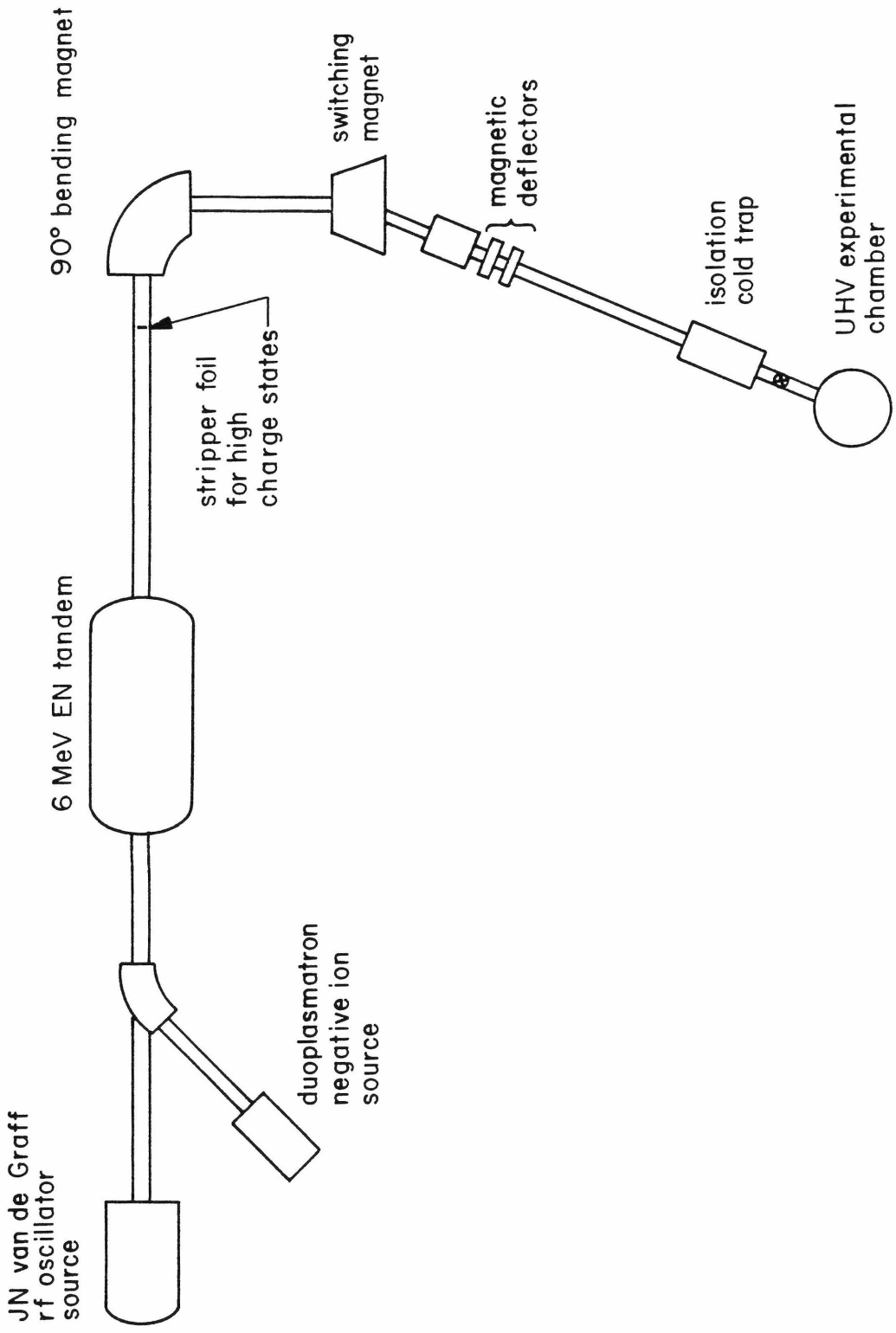
JN van de Graff
rf oscillator
source
duoplasmatron
negative ion
source
6 MeV EN tandem
stripper foil
for high
charge states
90° bending magnet
switching
magnet
magnetic
deflectors
isolation
cold trap
UHV experimental
chamber

Figure 2b

Figure 2b is a schematic view of the experimental chamber (looking north) showing the liquid nitrogen isolation trap, and the UHV chamber with all the external attachments.

The ports into the chamber include inlets for the target formation line, and the electrical feedthrough for the heater on the target formation line. The top flange supports the vernier feedthrough, which positions the detector and collimators. Electrical connections to the detector and beam collimators are made through an electrical feedthrough extending through the top flange.

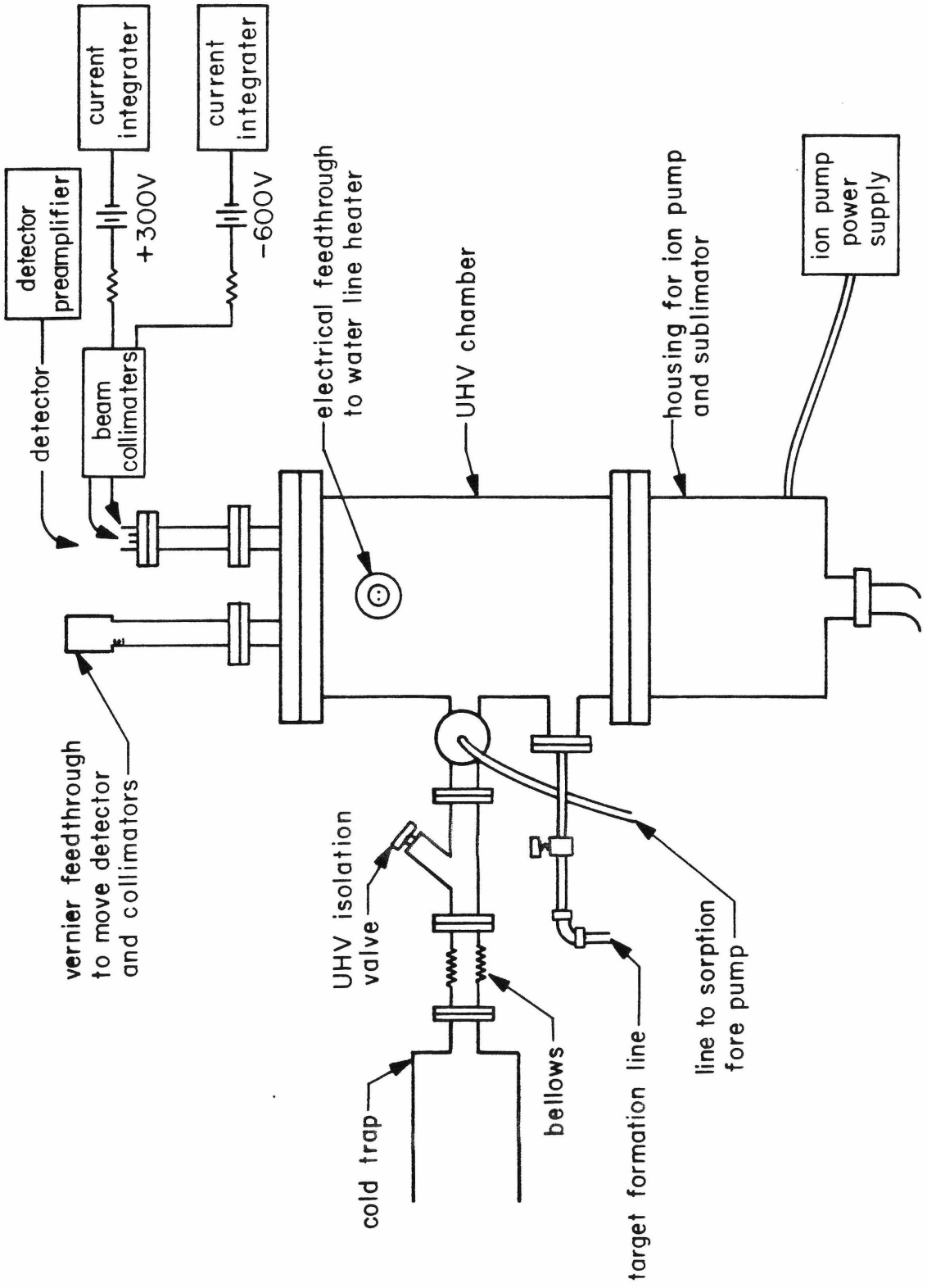
detector preamplifier
current integrater
current integrater
+300V
-600V
detector
beam collimaters
electrical feedthrough to water line heater
UHV chamber
housing for ion pump and sublimator
ion pump power supply
vernier feedthrough to move detector and collimators
UHV isolation valve
cold trap
bellows
target formation line
line to sorption fore pump

Figure 2c

Figure 2c shows a schematic view of the experimental chamber (looking west) showing the He cold finger and electrical attachments to the cold finger and target assembly.

The electrical feedthroughs on the cold finger go to the thermocouple, tip heater, cage bias, and target.

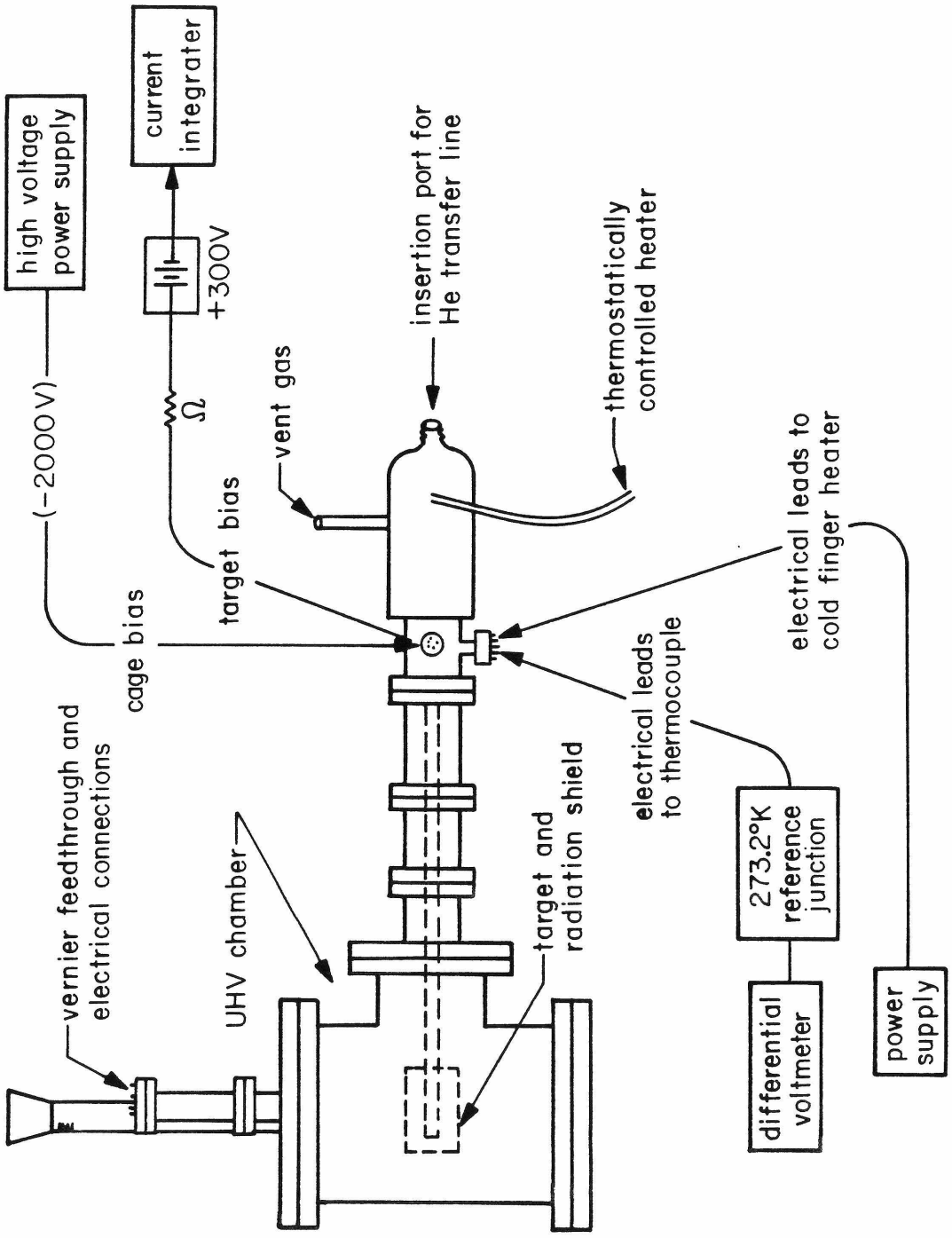
high voltage power supply
(-2000 V)
current integrater
+300V
Ω
target bias
cage bias
vent gas
insertion port for He transfer line
thermostatically controlled heater
electrical leads to cold finger heater
electrical leads to thermocouple
vernier feedthrough and electrical connections
UHV chamber
target and radiation shield
273.2°K reference junction
differential voltmeter
power supply

Figure 2d

Figure 2d shows the liquid He flow system. The liquid He dewar is pressurized to ~5 psi by a He gas cylinder. Liquid He flows through the transfer line onto the target end of the cold finger. He gas vents at the warm end of the cold finger and at the dewar end of the transfer line.

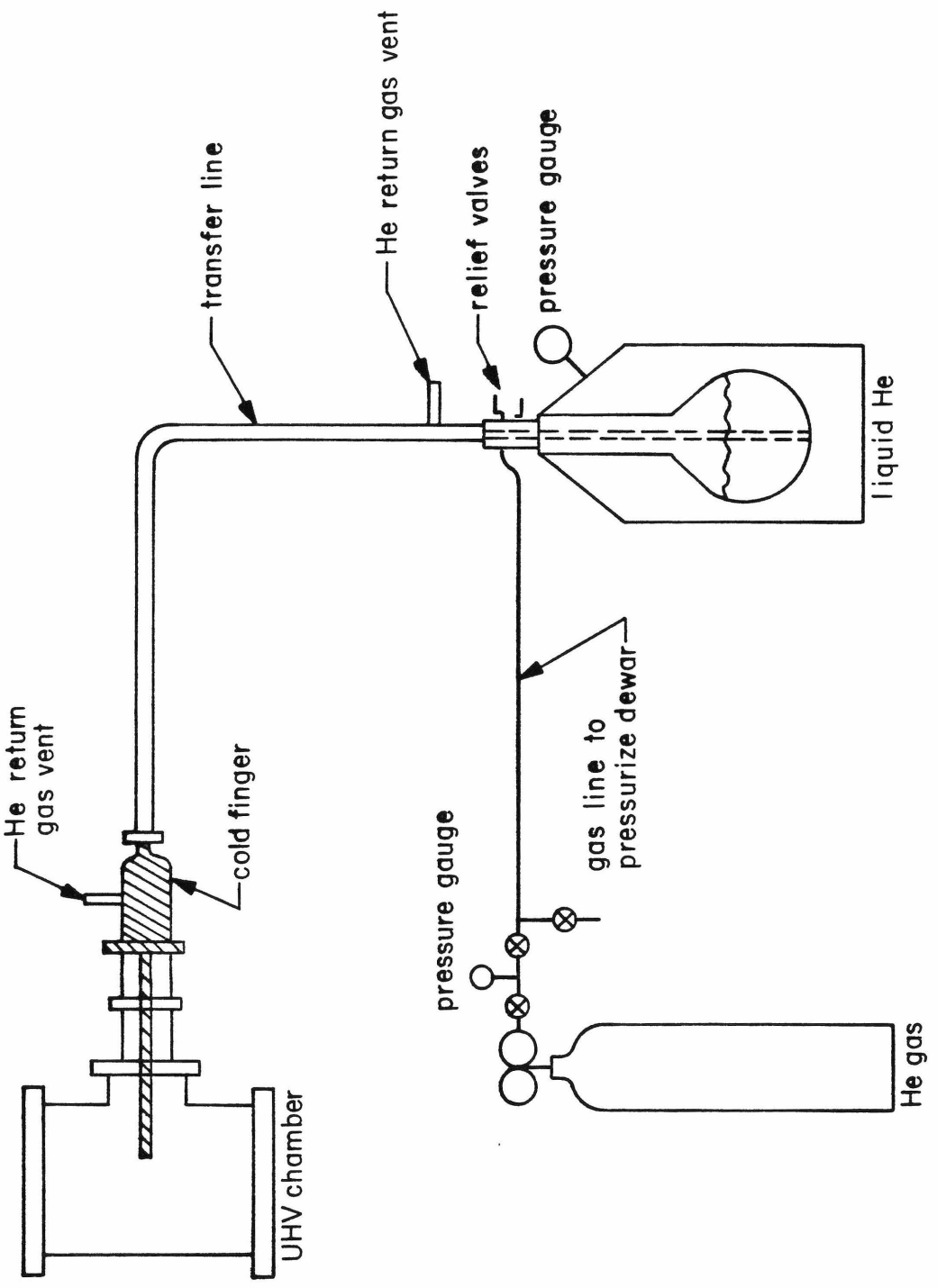
transfer line
He return gas vent
relief valves
pressure gauge
liquid He
He return gas vent
cold finger
gas line to pressurize dewar
pressure gauge
He gas
UHV chamber

Figure 2e

Figure 2e shows details of the target end of the cold finger.

Bottom diagram: This diagram shows the pyrex tube and resistance wire and insulating beads that make up the heater. The thermocouple leads are soldered into the cold finger and electrically insulated using pyrex beads. Also shown are the copper block, which supports the target assembly, and the electrical connections to the target and cage for beam integration and secondary electron supression. The radiation shield surrounds the target.

Top left: This view is a mirror image of the view through the radiation shield to the target, as seem by the beam. The large aperture in the radiation shield is 1/2" by 1 1/4".

Top right: This diagram is a detail of the target stack. There are indium gaskets between the Cu tip of the cold finger and the Cu target holder, to provide good thermal contact. There are other indium gaskets between the Cu block and the quartz, and the quartz and the Be. A stainless steel plate, tightened down by insulating screws, holds the target assembly in place. The gold marker is evaporated on the front surface of the Be disk.

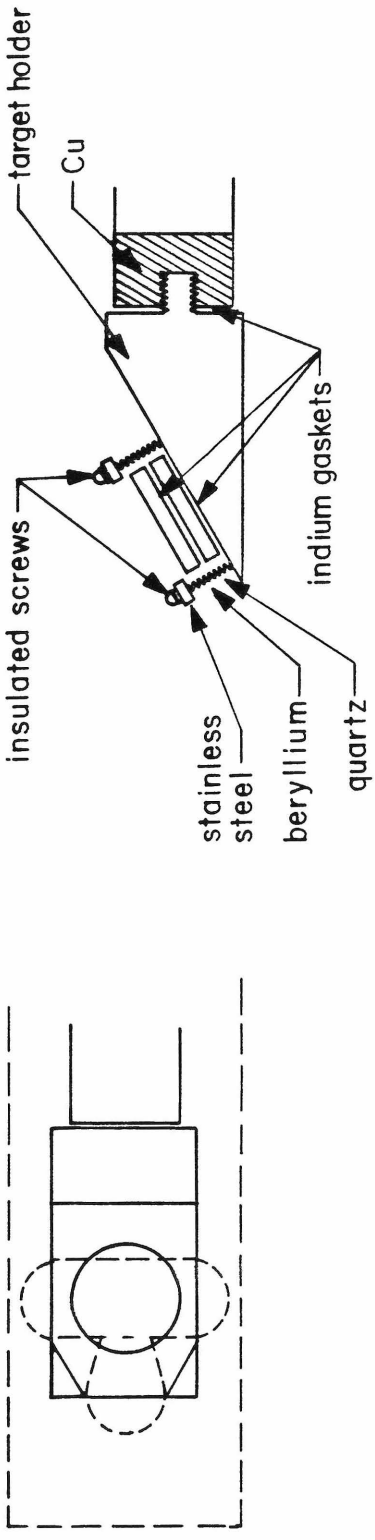
target holder
Cu
insulated screws
indium gaskets
stainless steel
beryllium
quartz

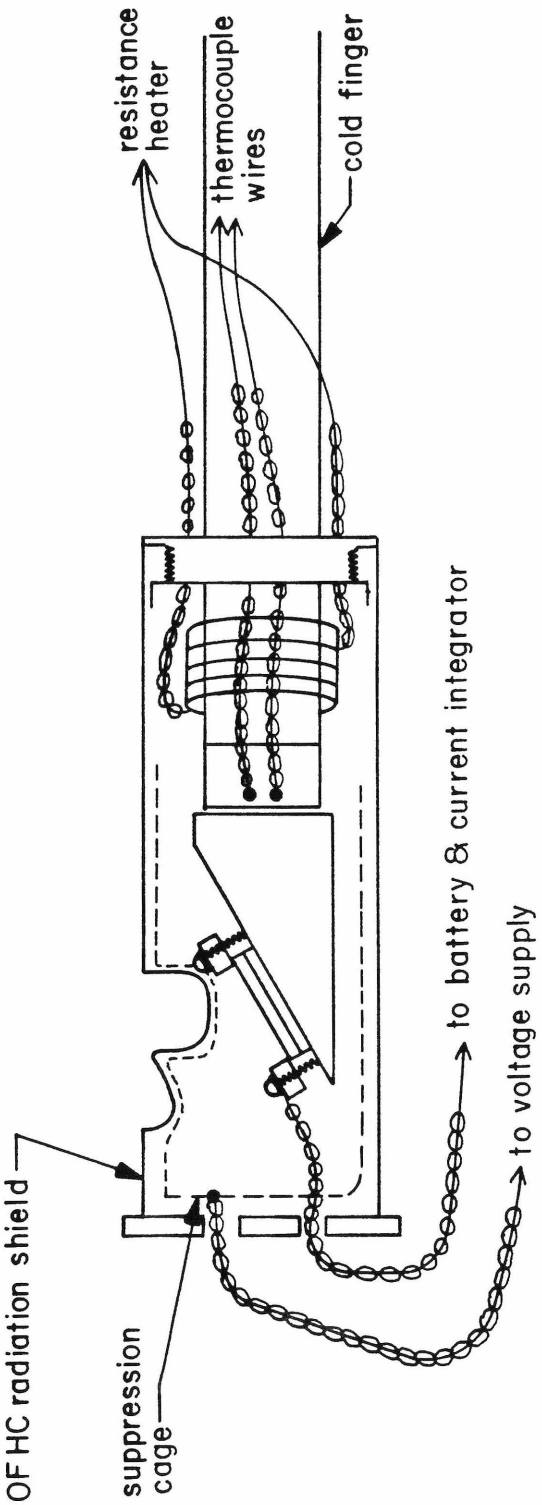
resistance heater
thermocouple wires
cold finger
OF HC radiation shield
suppression cage
to battery & current integrator
to voltage supply

Figure 2f

Figure 2f shows the thermocouple (Au(.07% Fe) vs Chromel(APC)) calibration data sent by Air Products and Chemicals, Inc., Allentown, PA. The reference junction for the thermocouple is 273.2°K.

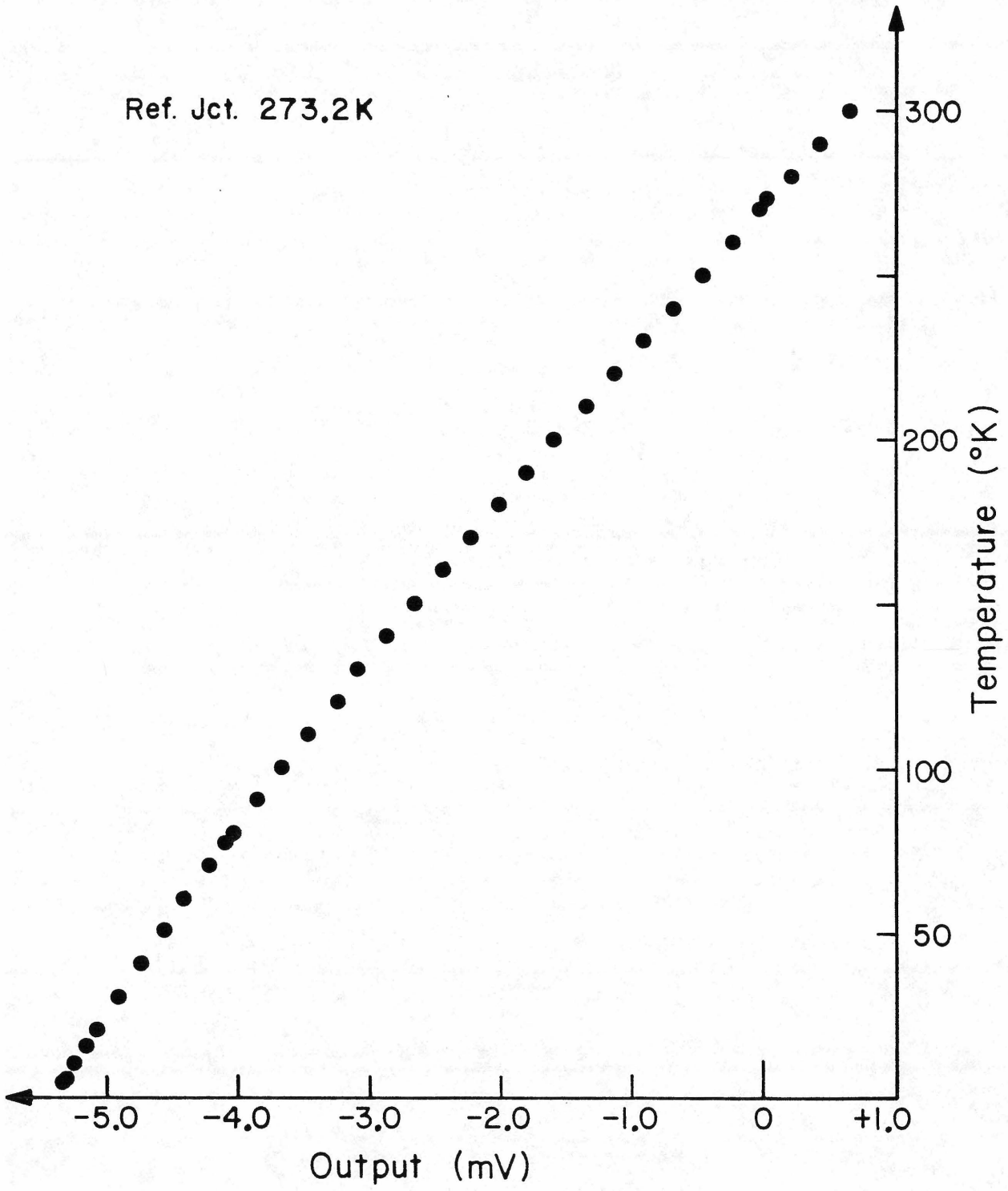
Ref. Jct. 273.2K
300
200
100
50
Temperature (°K)
-5.0
-4.0
-3.0
-2.0
-1.0
0
+1.0
Output (mV)

Figure 2g

Figure 2g shows a schematic of the apparatus inside the UHV chamber. The target formation line extends into the vacuum through a Conflat flange. It connects to a twisted copper tube via a stainless steel Swagelok reducing unit. The inset in the upper left hand corner of figure 2g shows how the copper line is oriented relative to the target.

Also shown in the figure is the detector holder. It is supported and moved up and down using the vernier feedthrough on the top flange. The beam collimators are attached by insulating scres to the detector holder, and move up and down with it. The electrical connections to the detector and collimators are made through an electrical feedthrough on the top flange.

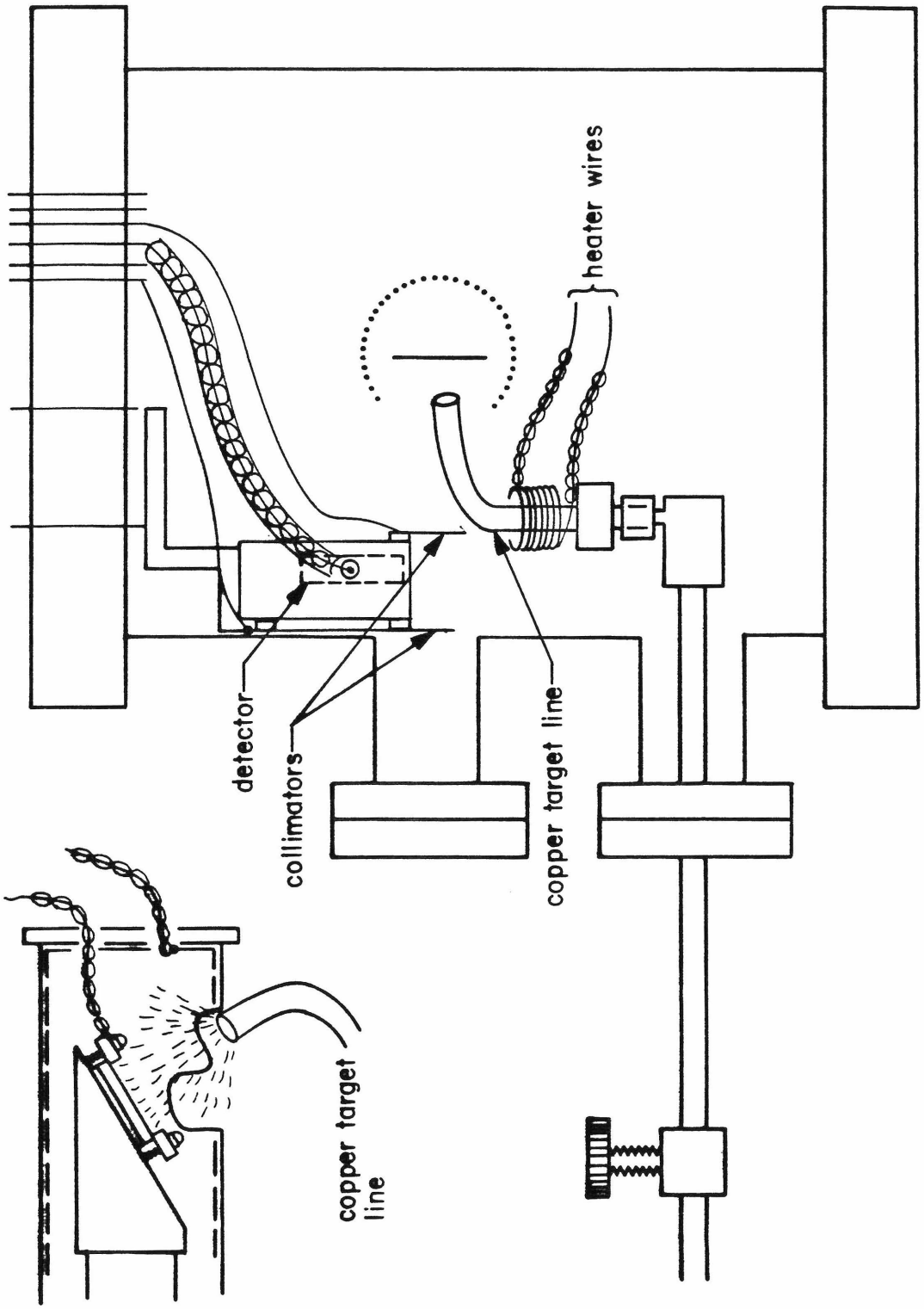
heater wires
detector
collimators
copper target line
copper target line

Figure 2h

Figure 2h shows a schematic of the target formation line. Water vapor resides above the water level in the pyrex vessel. This vapor pressure may be reduced by the mechanical roughing pump, and by the liquid nitrogen coil which isolates the pump from the target formation line. Flow of water vapor is controlled by adjusting the leak valve just above the water vessel. The final entrance into the chamber is through a high vacuum valve which is open only during target formation.

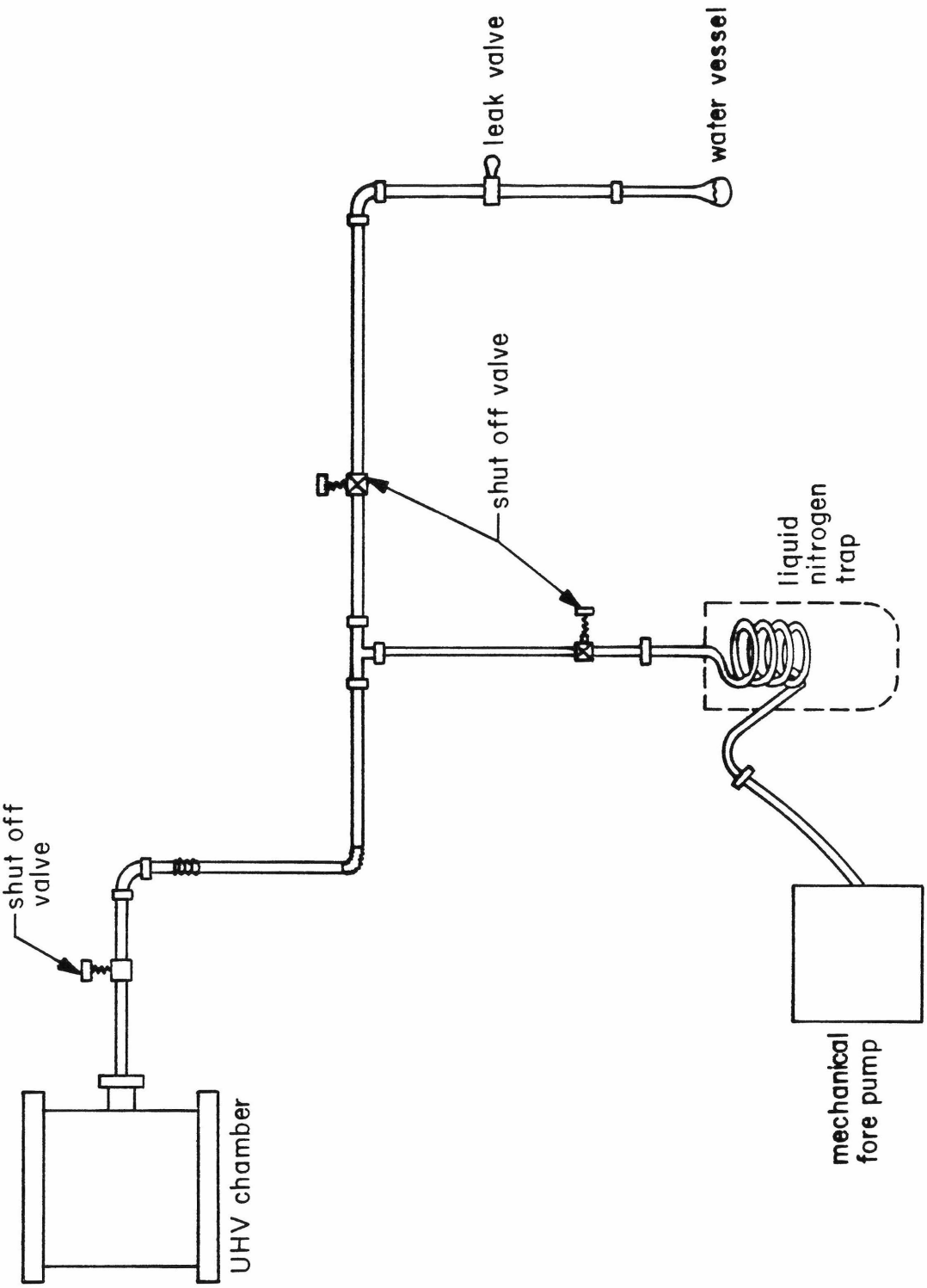
leak valve
water vessel
shut off valve
liquid
nitrogen
trap
shut off
valve
UHV chamber
mechanical
fore pump

Figure 21

This figure shows the detector holder, surface barrier detector, and beam collimators. In the top view, the beam approaches from the left, passes through the collimators, and scatters back onto the detector. In the bottom view, the area between the two shaded collimators represents the sensitive surface of the detector. This is the view seen by the target.

Collimator a is electrically isolated, and biased to +300V. Its central hole is 0.041" diameter, the lower hole is 0.062" by 0.161".

Collimator b is grounded. The central hole is 0.080".

Collimator c is grounded, and has a thin-walled stainless steel tube on one side (0.081" I. D. tube).

Collimator d is electrically isolated and held at -600V. Its aperture is 1/4" by 1/4".

Collimator e is grounded. The hole is 0.377" diameter.

Collimator f is also grounded. It is a 0.200" diameter hat with a hole through the middle to admit beam.

Also shown in the figure are; the 800 Gauss horseshoe magnet located between collimators a and d, and the 1/4" stainless steel rod and ball bushing used to keep the horizontal alignment of the detector holder constant.

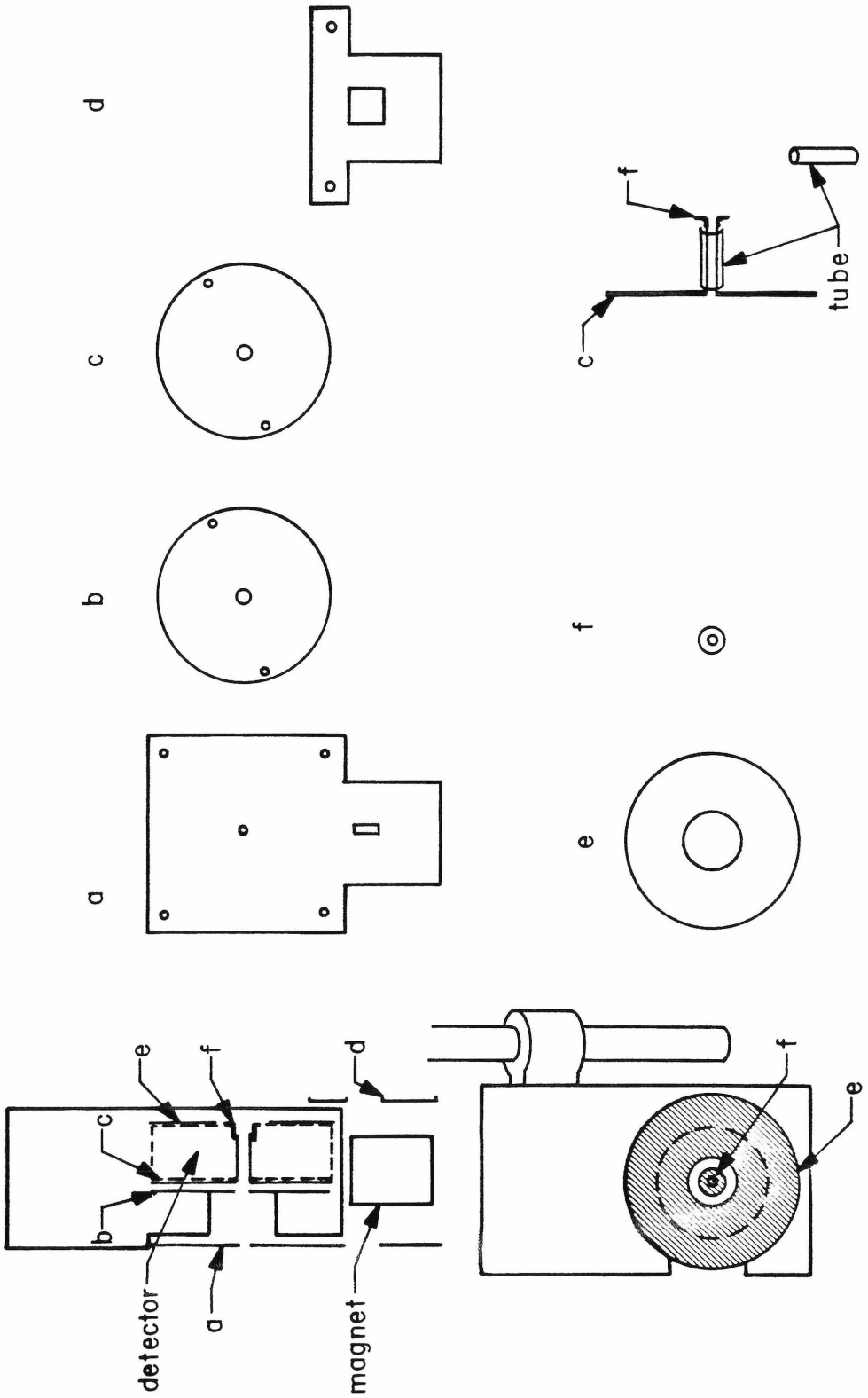
a
b
c
d
e
f
tube
detector
magnet

Figure 2j

Figure 2j shows the two configurations of the detector and collimators with respect to the target. Also shown is the path that the beam must take after scattering off the target and into the detector

The top diagram shows the case when the beam passes through the annular surface barrier detector and scatters at 180° into the detector. The bottom diagram shown the detector moved up out of the path of the beam. The beam passes first through a collimator biased at +300V. It then passes between the pole faces of an 800 Gauss magnet, and finally through a -600V collimator. In this case, beam scatters from the target at 145°–163° to reach the detector.

Also shown in the top diagram is the target biasing configuration. Beam that has passed through the collimators passes through the aperture in the grounded radiation shield. It then passes through the -2000V suppression cage, and strikes the target biased at +300V. The target is electrically connected to the current integrator, where the beam current is monitored.

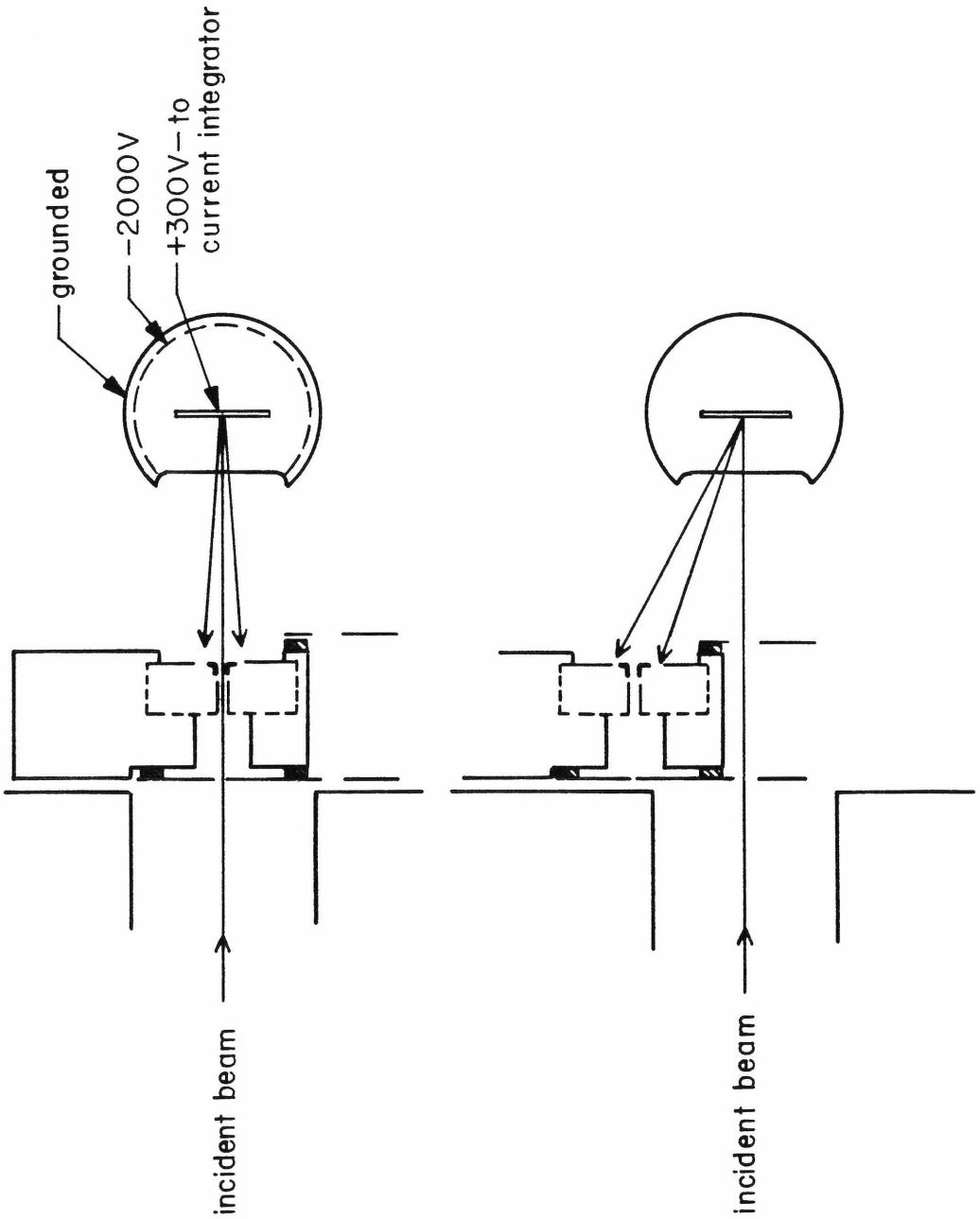
grounded
-2000V
+300V—to
current integrator
incident beam
incident beam

Figure 2k

Figure 2k shows a schematic of the electronics used to accumulate spectra. Current signals are sent from the detector to a charge-sensitive preamplifier. (A fixed amplitude pulser signal is also fed to the preamplifier). Voltage steps from the preamplifier are sent to an amplifier where they are shaped as unipolar and bipolar pulses (two separate amplifiers were used to take the ^{4}He and ^{19}F spectra). The bipolar pulses are sent to an oscilloscope used to monitor pulse shape during the runs. The unipolar pulses were sent to the multi-channel analyzer which accumulated the spectra. These spectra were stored on magnetic tape.

Digital pulses from the current integrator were fed to a preset charge collector which was used to gate the ADC from collecting charge after the preset value was reached. These same digital pulses were sent to the inputs of a pair of master-slave scalers. The master was gated by the preset charge collector, and the slave was gated by the busy signal of the ADC. Comparing the counts in the two scalers gave an indication of the dead time of the system.

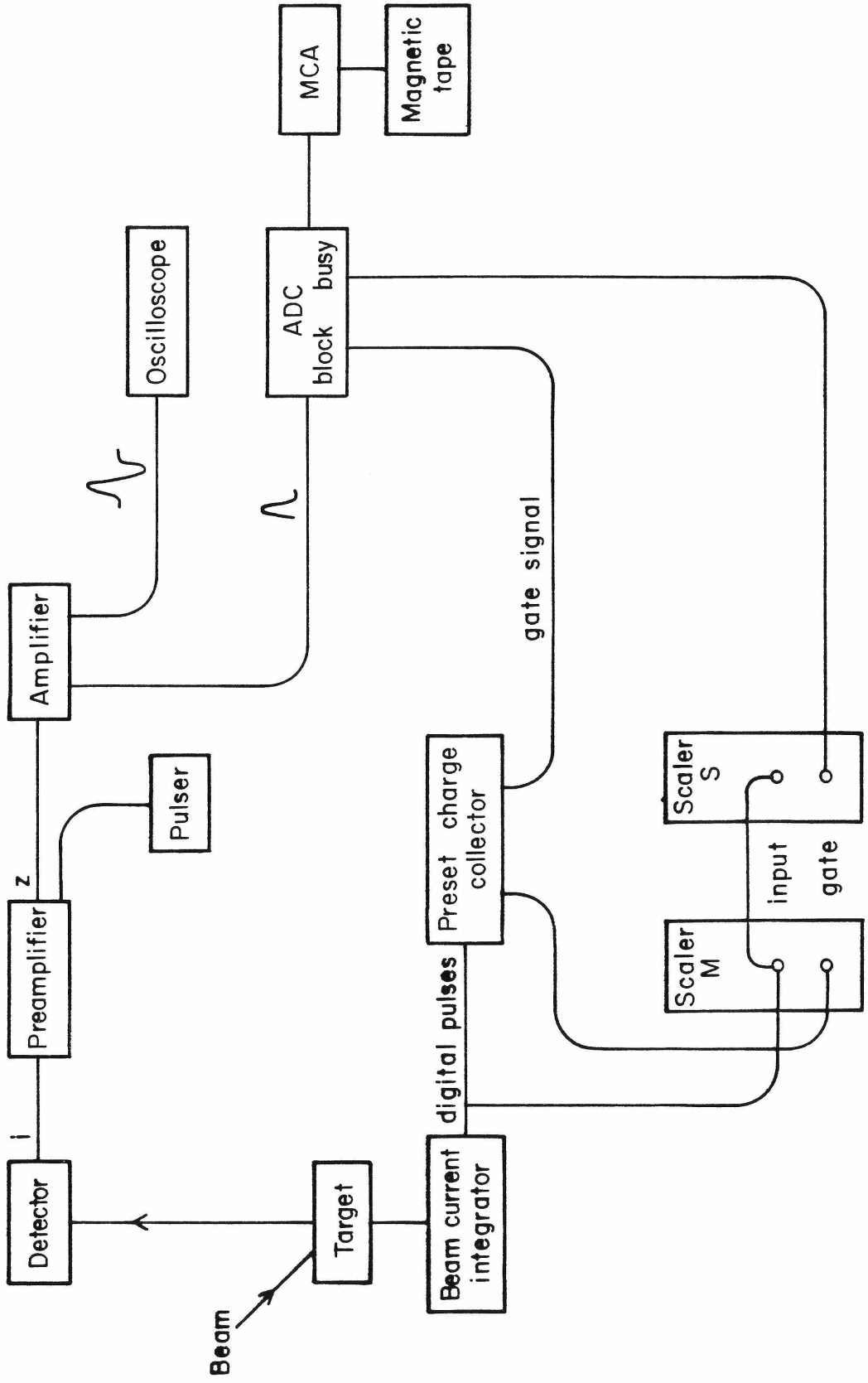
MCA
Magnetic tape
Oscilloscope
ADC
block busy
Amplifier
gate signal
Pulser
Preamplifier
z
i
Preset charge collector
Scaler S
input
gate
Scaler M
digital pulses
Detector
Target
Beam current integrator
Beam

Figure 3a

Figure 3a shows two examples of the spectra taken on the He analysis runs. One is a spectrum taken on the bare target (the horizontal dashes); the other was taken after deposition of a new ice target (the dots). Notice the shifts in the Be edge (~ channel 100) and the gold peak (~ channel 650). Also note the change in the size of the oxygen peak before and after the ice was deposited (~ channel 250).

Figures 3b and 3c are expanded versions of different parts of these same two spectra. Also shown in figures 3b and 3c are points from the analysis run taken after the ice target was sputtered. All three spectra are taken from the second measurement from run f of table A.

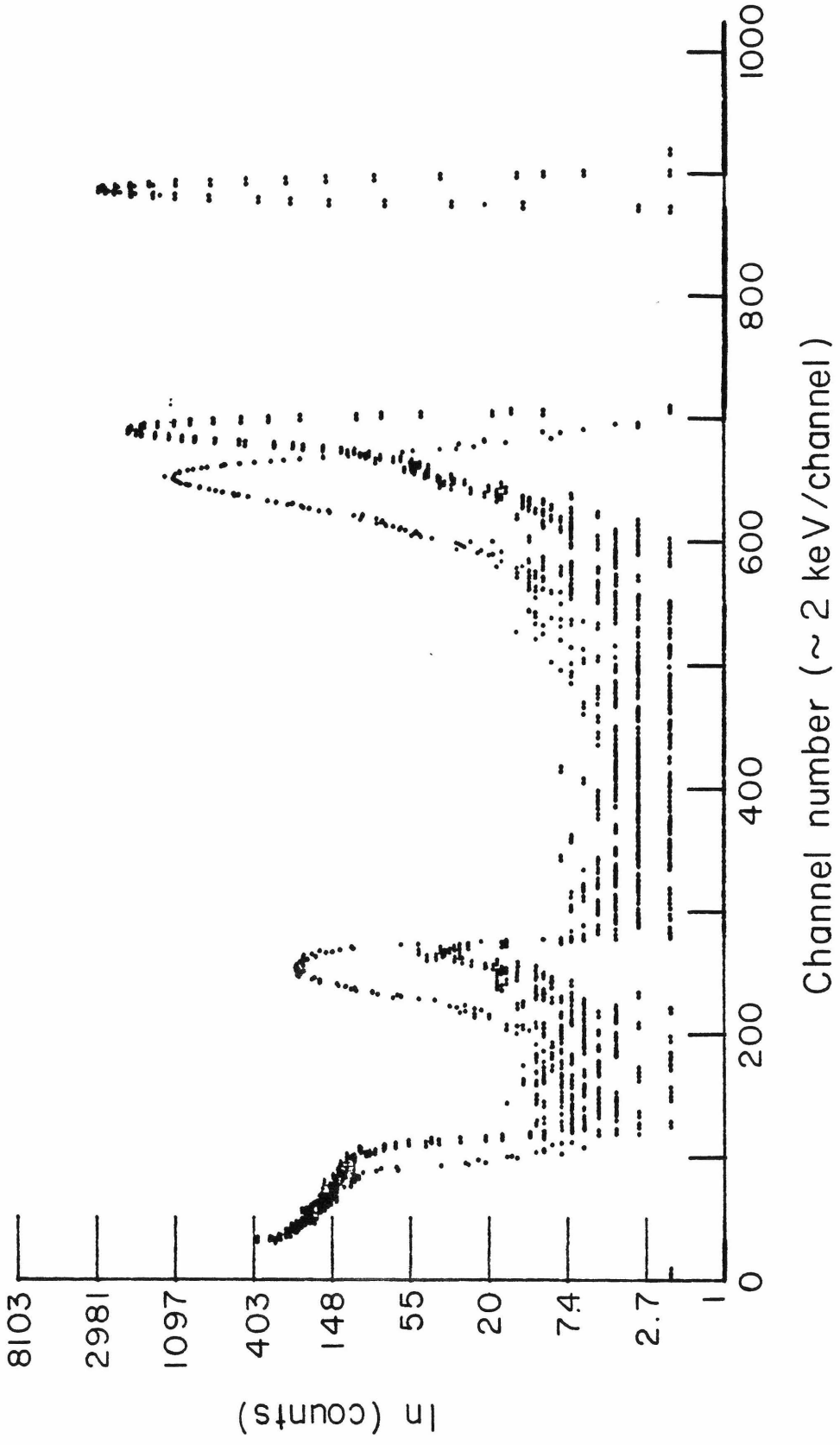
8103
2981
1097
403
148
55
20
7.4
2.7
1
ln (counts)
0
200
400
600
800
1000
Channel number (~ 2 keV/channel)

Figure 3b

Figure 3b shows the Be edge and oxygen peaks of three spectra. The dots are from an analysis run taken on the bare target, the dots with circles are a new ice target, and the horizontal dashes are from the spectrum taken after a sputtering run. These spectra are from the second measurement from run f of table A.

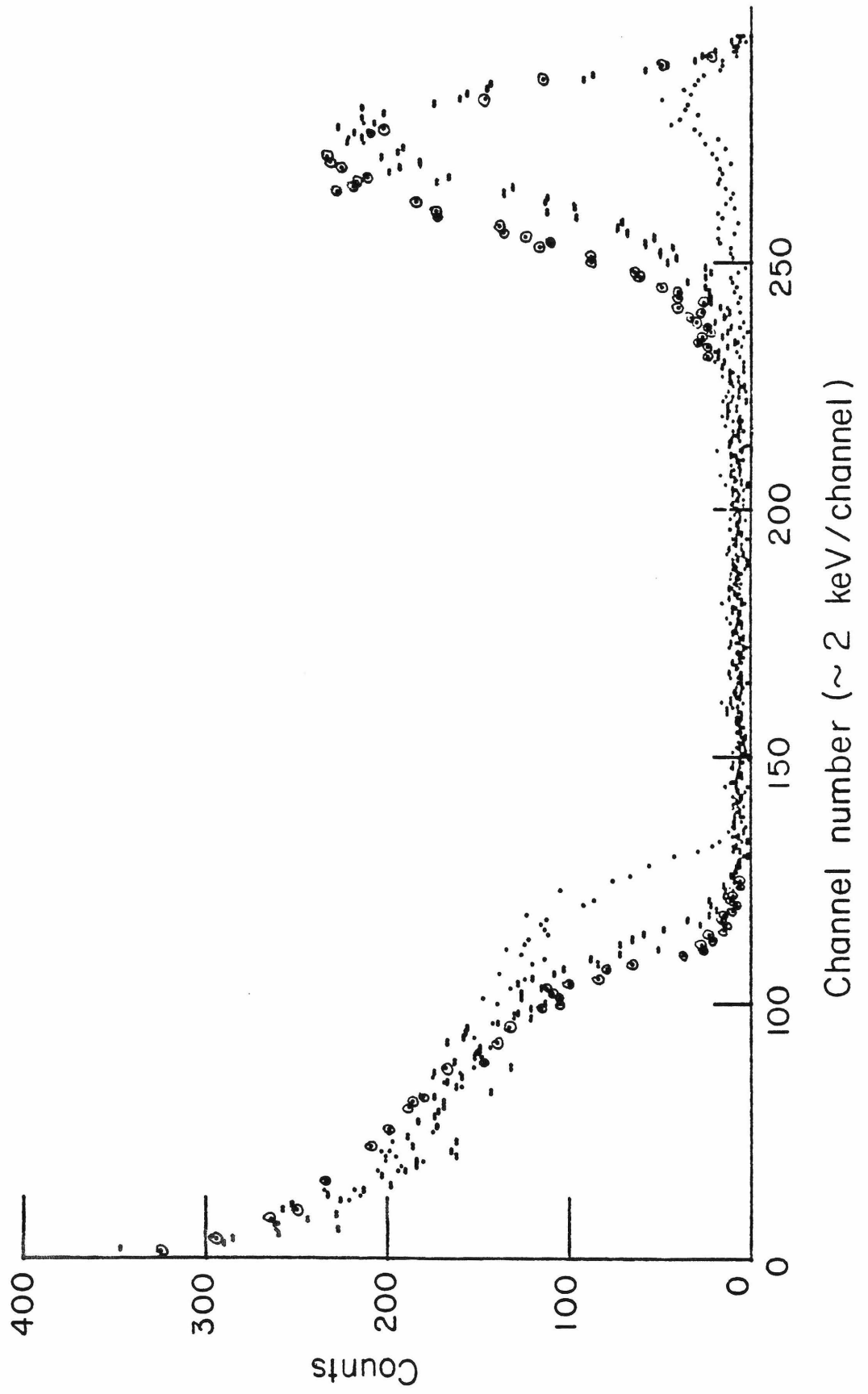
Counts
400
300
200
100
0
0
100
150
200
250
Channel number (~ 2 keV/channel)

Figure 3c

Figure 3c shows the gold peak from the same three spectra shown in figure 3b. The dots are the bare target run, the dots with circles are the new ice target, and the horizontal dashes are from the spectrum taken after the sputtering run (see run f of table A).

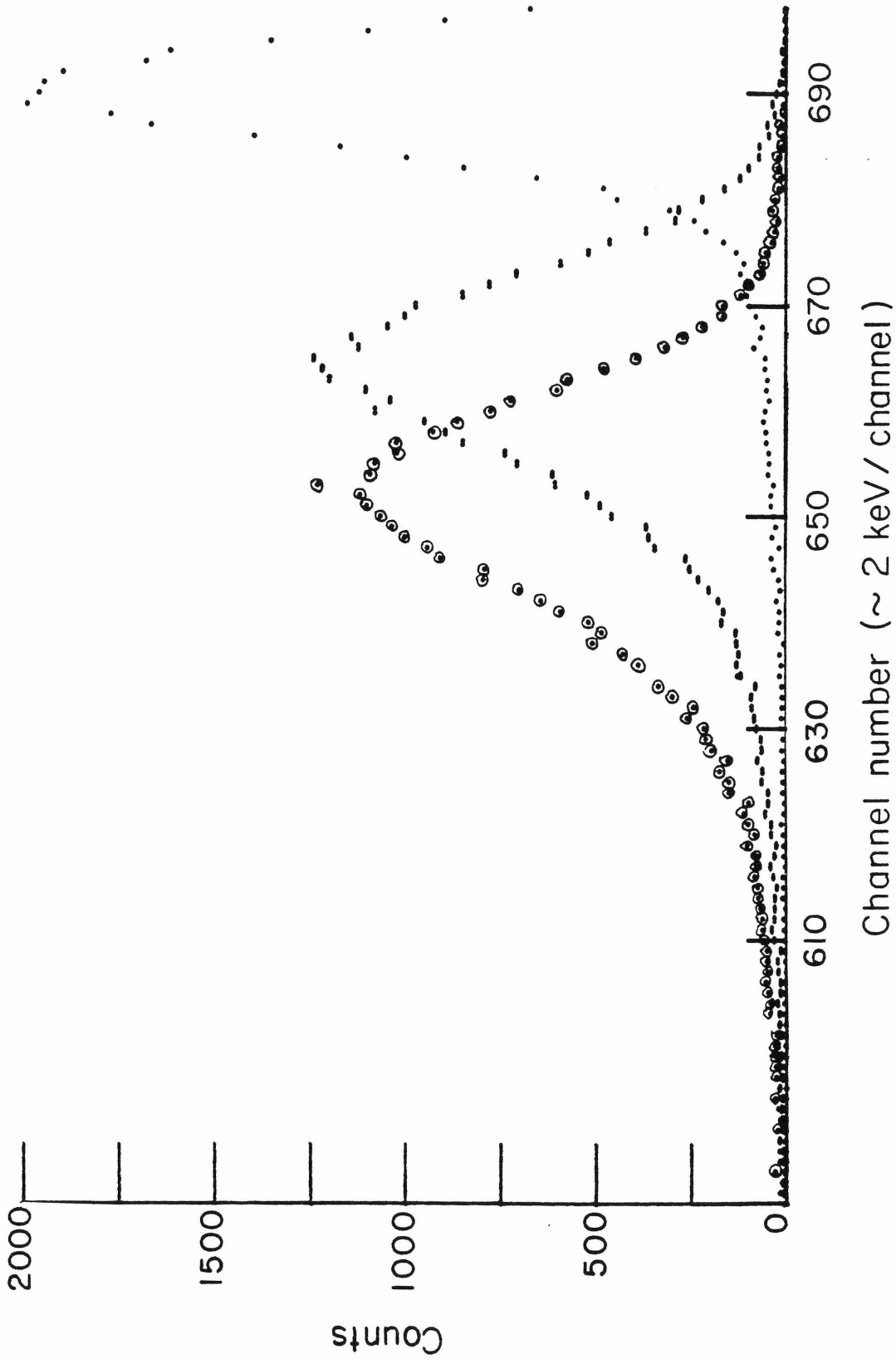
Counts
2000
1500
1000
500
0
610
630
650
670
690
Channel number (~ 2 keV / channel)

Figure 4a

Figure 4a shows the thickness profiles of the initial ice layers used in the F sputtering runs (see runs a-m from table A). The thicknesses shown here were calculated from the shifts in the gold peaks on spectra taken with He scattered from four spots on the target. These were the same four locations as those where the sputtering runs were done.

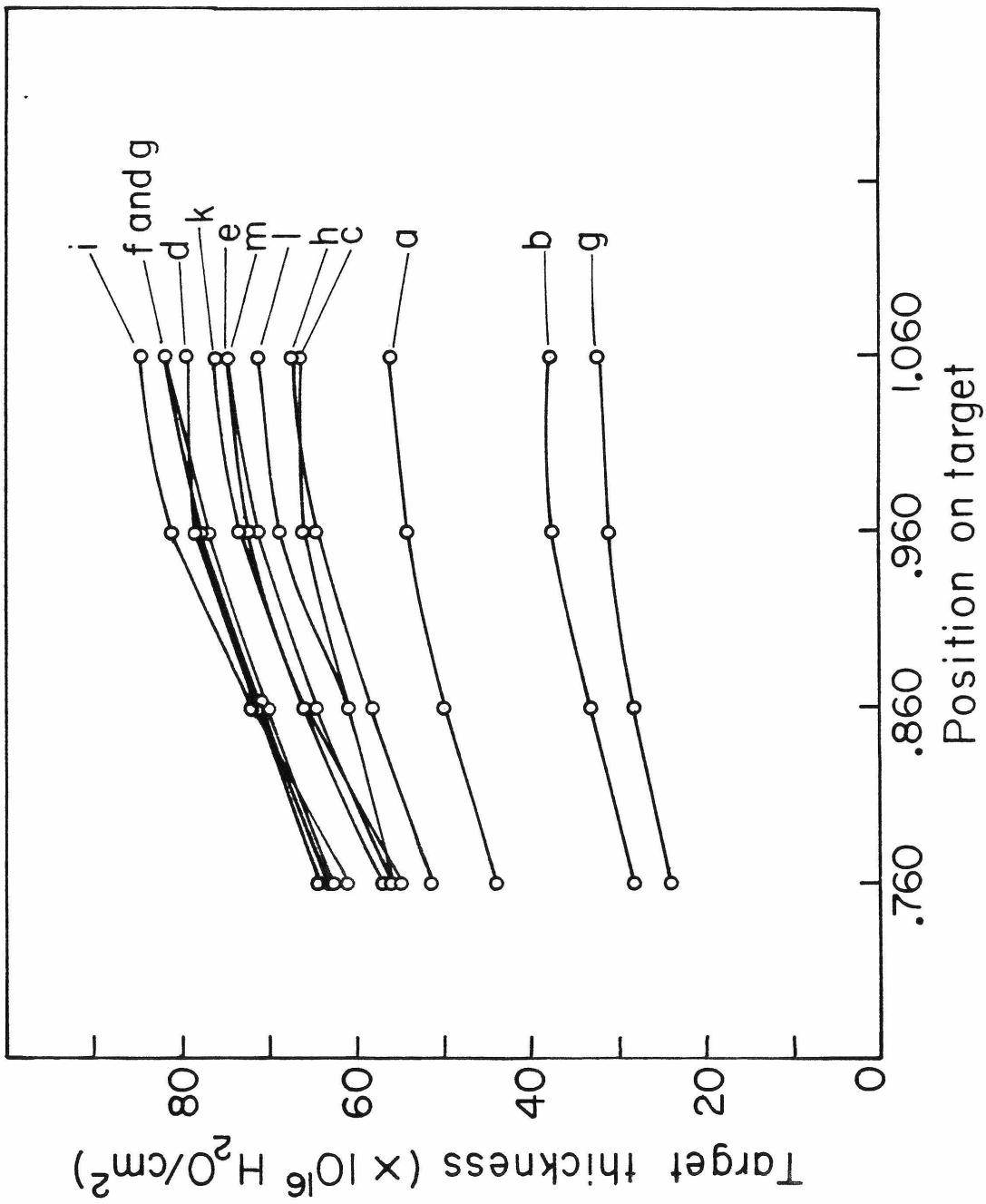
Target thickness (x 10^{16} H_2O/cm^2)
0
20
40
60
80
.760
.860
.960
1.060
Position on target
i
f and g
d
k
e
m
l
h
c
a
b
g

Figure 4b

Figure 4b shows the results of the erosion of ice targets (~10°K) by ^{19}F beams of energy (charge state) 1.6(+2), 5.0(+2), 6.0(+3), 7.5(+3), 10.0(+3), 15.0(+4), 20.0(+4), and 25.0MeV(+5). The results of the two different methods of calculating S are shown (error bars indicate experimental reproducibility; where no error bars are shown, there was only one run, or the errors are smaller than the point size; see table A). The curve of dE/dx, also shown in the figure, is the electronic stopping power for H in H_2O calculated using Bragg's rule and the Ziegler tables (Ziegler 1980).

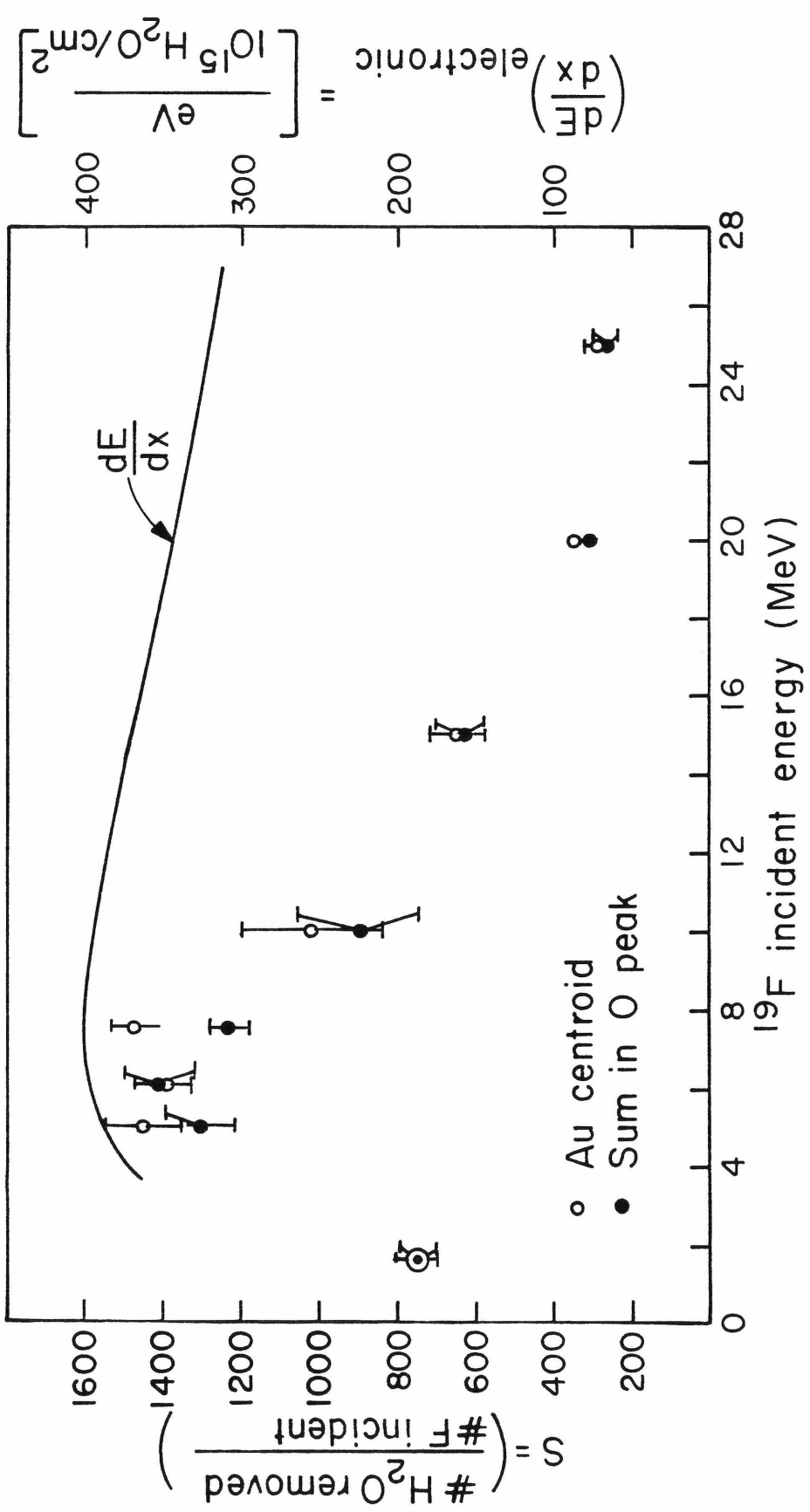
S = (# H2O removed / # F incident)
1600
1400
1200
1000
800
600
400
200
0
4
8
12
16
20
24
28
19F incident energy (MeV)
dE/dx
o Au centroid
• Sum in O peak
100
200
300
400
(dE/dx)electronic = [eV / 10^15 H2O/cm2]

Figure 4c

Figure 4c shows the charge states of ^{19}F as a function of energy. The solid curve gives the equilibrium charge states of F, calculated using a formula given by Ziegler (1980). The diamonds are also equilibrium charge states, calculated from curves given by Marion and Young (1968). The circles and squares are data taken on the equilibrium charge state of ^{19}F, as given by Wittkower and Betz (1973). The triangles show the incident F charge states used in the sputtering runs.

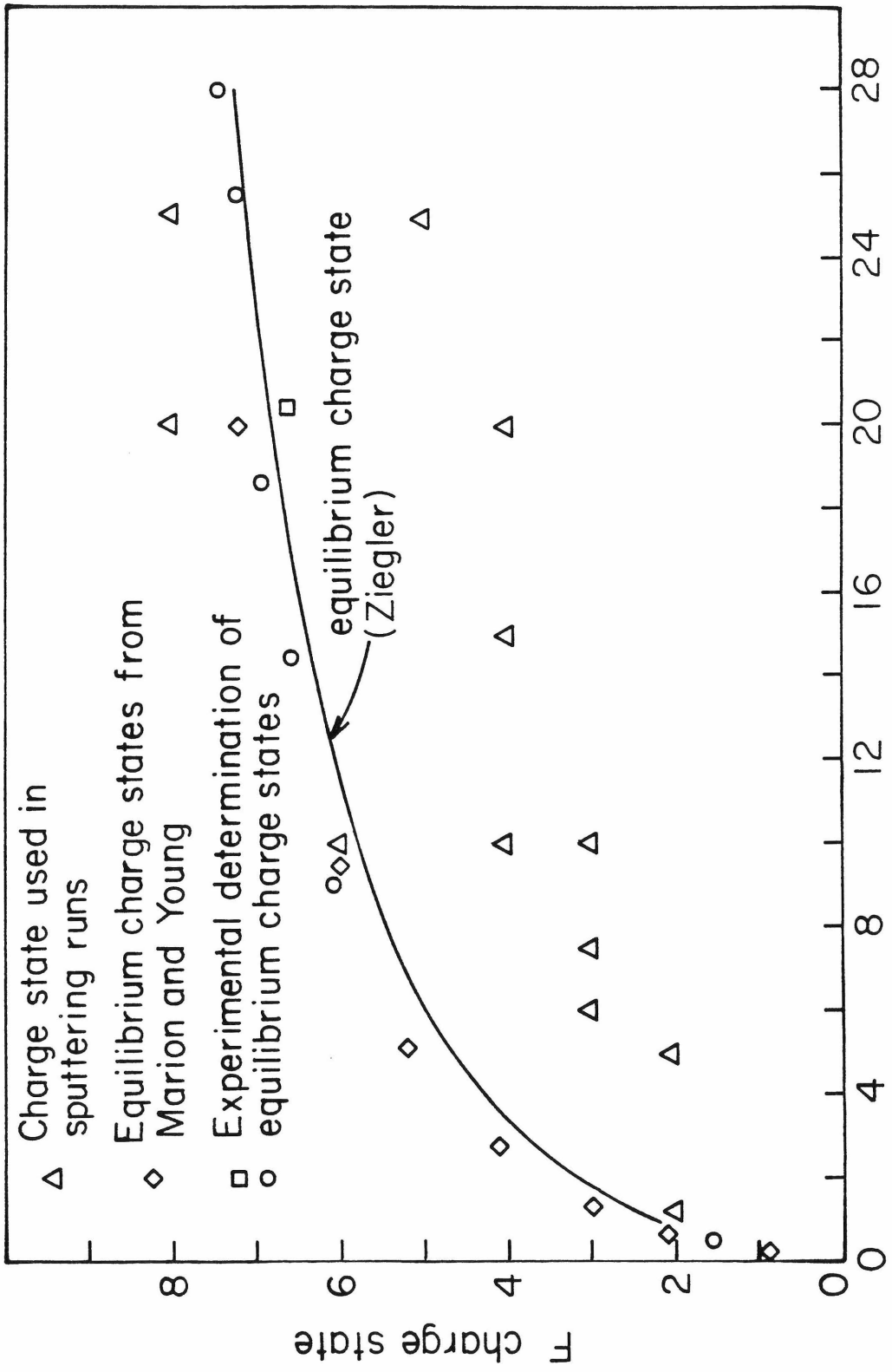
Charge state used in sputtering runs
Equilibrium charge states from Marion and Young
Experimental determination of equilibrium charge states
equilibrium charge state (Ziegler)
F charge state
0
2
4
6
8
0
4
8
12
16
20
24
28
19F energy (MeV)

Figure 4d

Figure 4d shows results of the erosion of ice targets (10°K) with ^{19}F beams. These data are the same as those shown in figure 4b, except that additional high charge state runs are shown for some F energies. Also shown in the figure are the equilibrium charge states at each of the F energies. These charge states were calculated from a formula given by Ziegler (1980). The curve for dE/dx is calculated using Bragg's rule and data from Ziegler (1980).

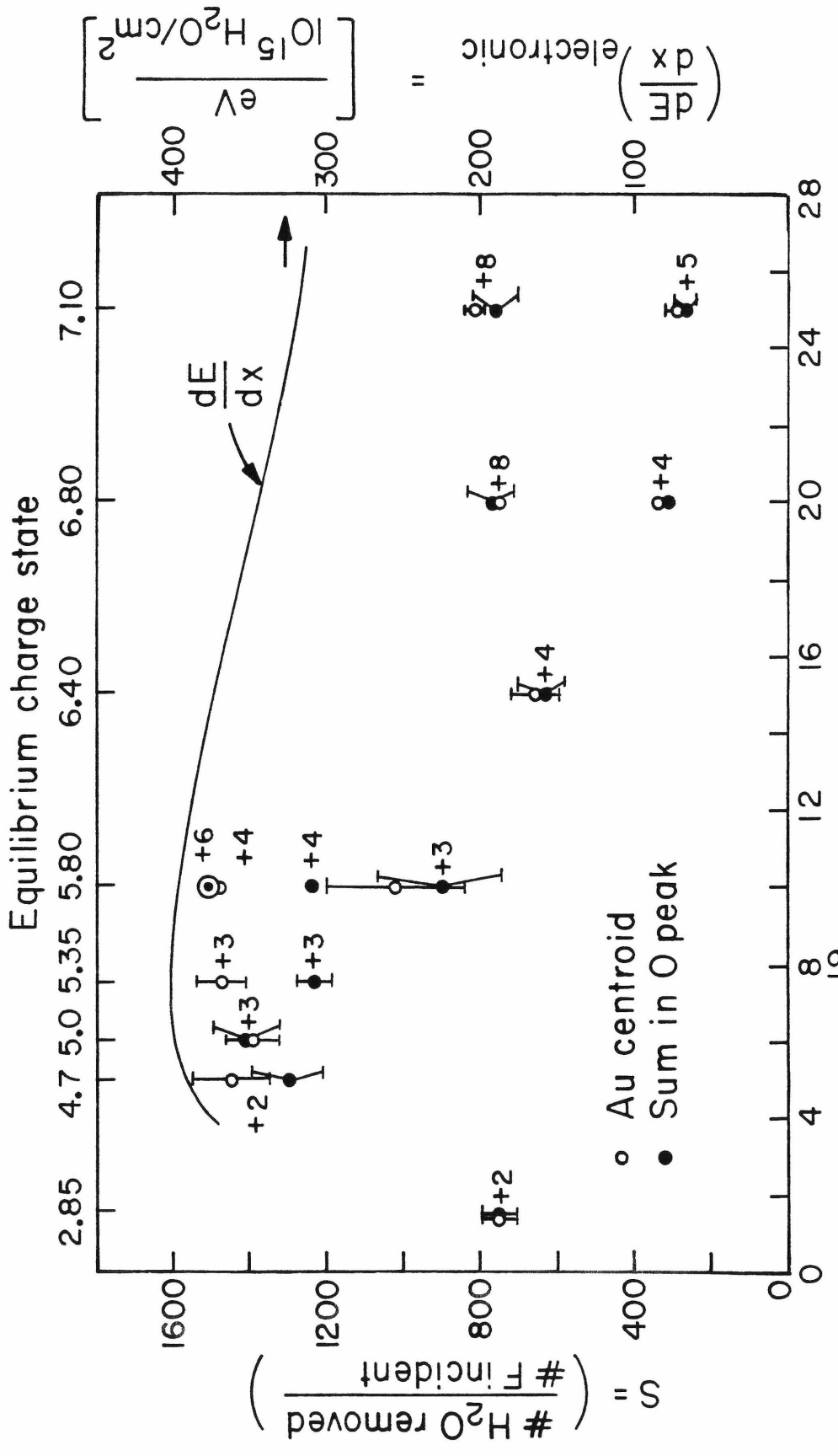
S = (# H2O removed / # F incident)
1600
1200
800
400
0
Equilibrium charge state
2.85
4.7
5.0
5.35
5.80
6.40
6.80
7.10
+2
+3
+3
+6
+4
+3
+4
+3
+2
+8
+4
+8
+5
dE/dx
o Au centroid
• Sum in O peak
0
4
8
12
16
20
24
28
19F incident energy (MeV)
400
300
200
100
(dE/dx)electronic = eV / [10^15 H2O/cm2]

Figure 4e

Figure 4e shows the results of sputtering ice with 10.0MeV $^{19}F^{+3}$ beams as a function of the substrate temperature. The runs are from f and h of table A. The two runs at ~10°K are the average of the measurements taken in runs e, g, the first two of i, and the first two of h from table A.

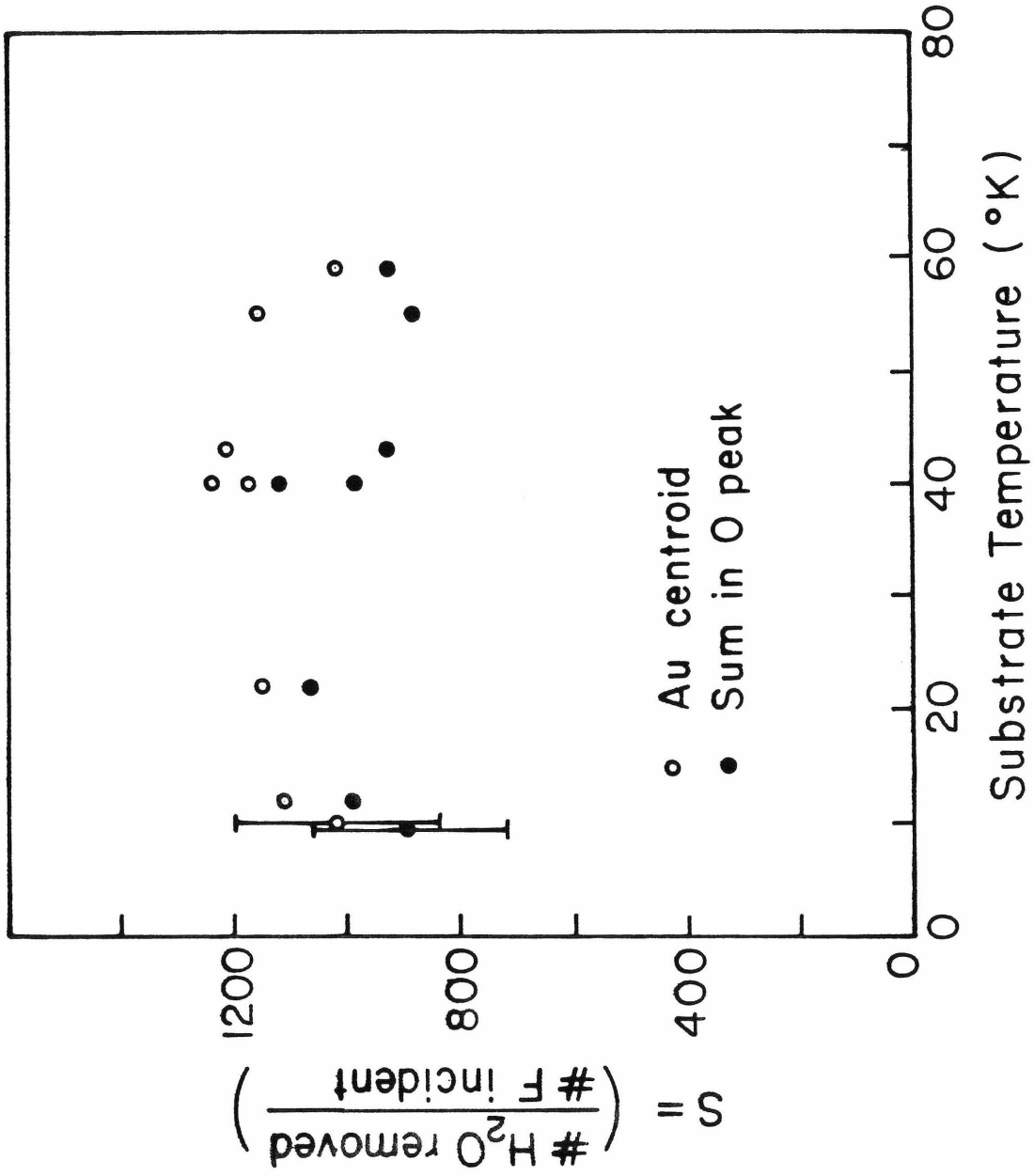
S = (# H2O removed / # F incident)
0
400
800
1200
0
20
40
60
80
Substrate Temperature (°K)
Au centroid
Sum in O peak

Figure 4f

Figure 4f shows curves of dE/dx for ^4He in H_2O taken from various sources in the literature. The values of dE/dx used in analyzing the sputtering data were taken from the experimental curve for the stopping power of He on H_2O(solid) measured by Matteson and coworkers (1977). The other curves shown in figure 4f are described in chapter IV, section C-2.

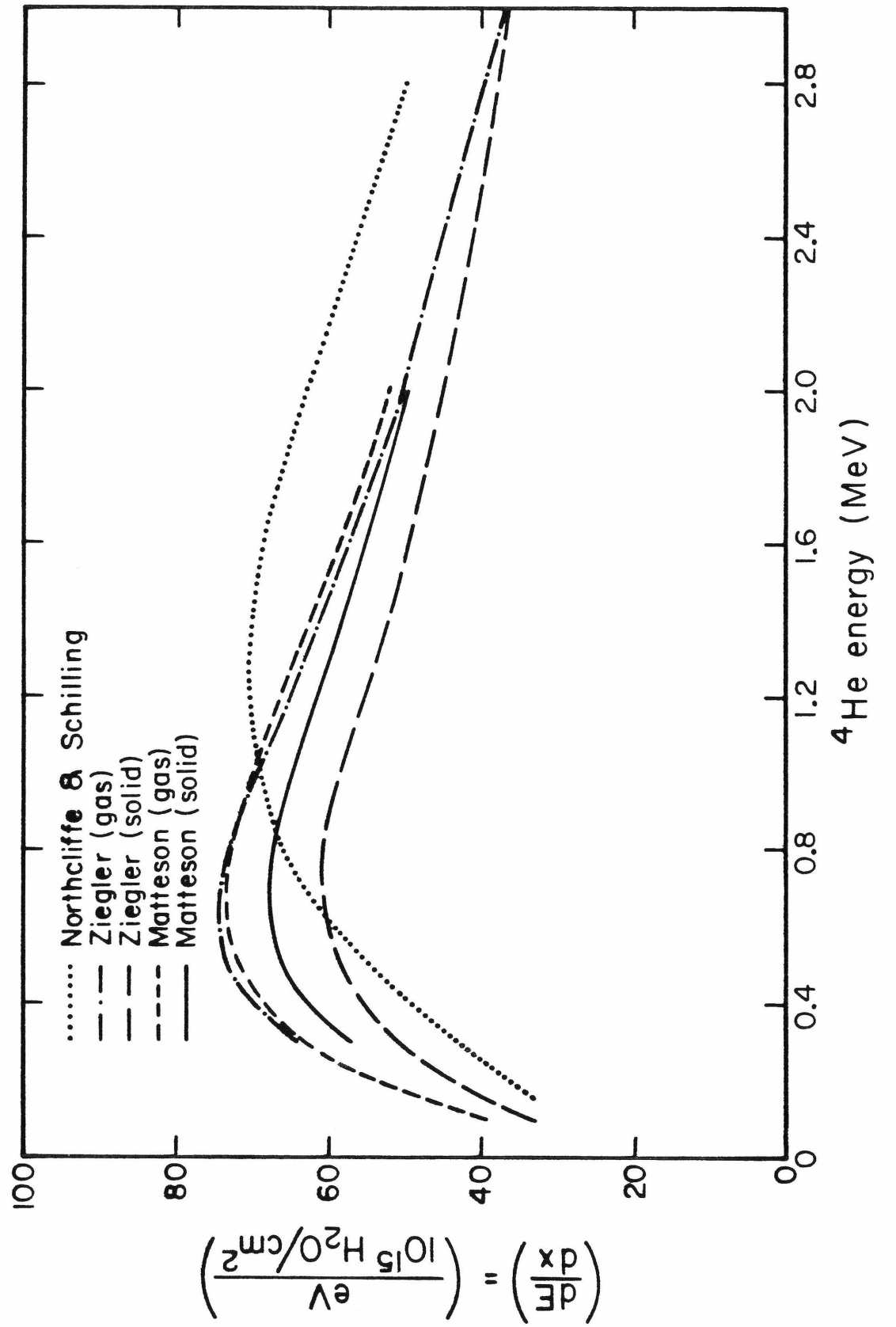
Northcliffe & Schilling
Ziegler (gas)
Ziegler (solid)
Matteson (gas)
Matteson (solid)
$\left(\frac{dE}{dx}\right) = \left(\frac{eV}{10^{15}\ H_2O/cm^2}\right)$
^{4}He energy (MeV)
0
20
40
60
80
100
0
0.4
0.8
1.2
1.6
2.0
2.4
2.8

Figure 4g

Figure 4g shows curves of dE/dx for ^{19}F in H_2O. The curve labelled Ziegler was calculated by using Bragg's rule and data given for the stopping power of F in H(solid) and O(solid) (Ziegler 1980). These Ziegler values were the ones used to fit the experimental sputtering data.

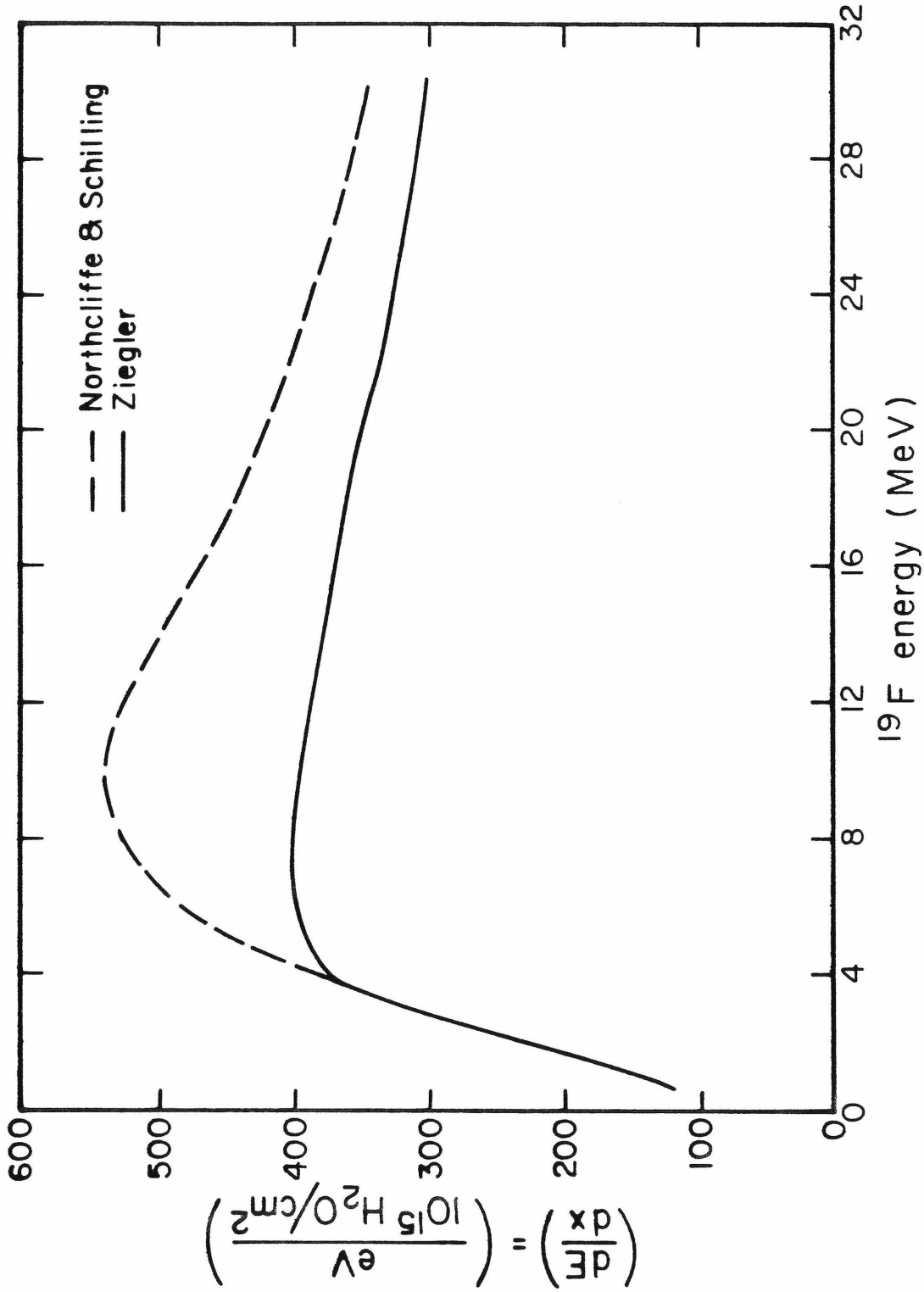
Northcliffe & Schilling
Ziegler
$\left(\frac{dE}{dx}\right) = \left(\frac{eV}{10^{15}\ H_2O/cm^2}\right)$
^{19}F energy (MeV)
0
100
200
300
400
500
600
4
8
12
16
20
24
28
32

Figure 4h

Figure 4h shows the results of measuring the size of the oxygen peak in an ice layer by backscattering beams of 1.3, 1.4, 1.5, 1.6, and 1.7MeV ^4He from the same ice layer. The counts in the oxygen peaks are plotted vs $1/E^2$. The purpose of these runs was to test for a non-elastic cross section in the He-O scattering reaction at He energies close to 1.5MeV. Since the Rutherford cross section goes as $1/E^2$, the sizes of the oxygen peak should scale as $1/E^2$. No significant deviation from a straight line was seen.

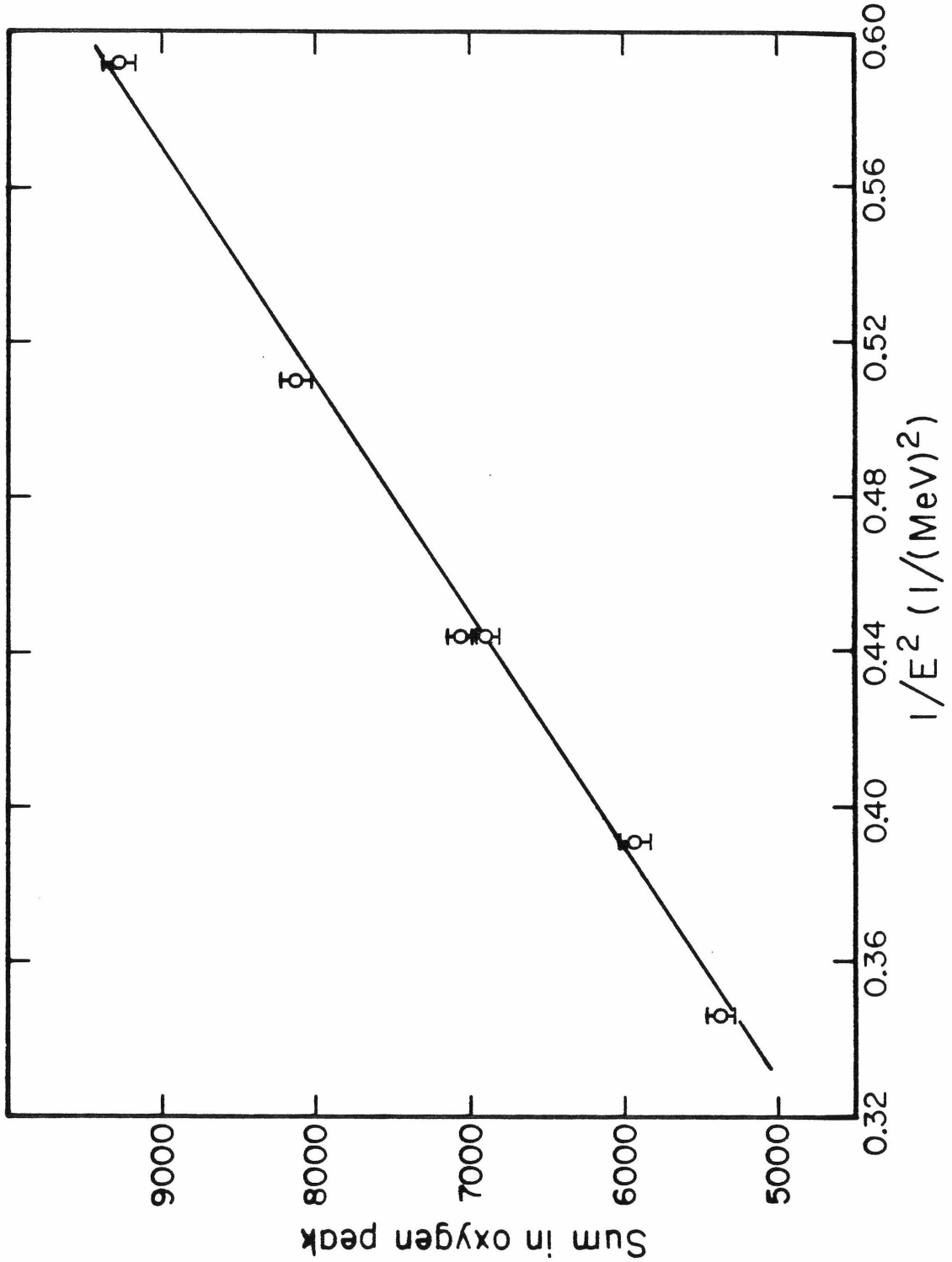
Sum in oxygen peak
9000
8000
7000
6000
5000
0.32
0.36
0.40
0.44
0.48
0.52
0.56
0.60
1/E² (1/(MeV)²)

Figure 4i

Figure 4i shows the results of sputtering ice by protons (Brown et al. 1980a). Also shown are arbitrarily normalized curves of (dE/dx), $(dE/dx)^2$, and $(dE/dx)^4$ obtained by Bragg's rule and data from Anderson and Ziegler (1977) for H on H(solid) and O(solid) targets.

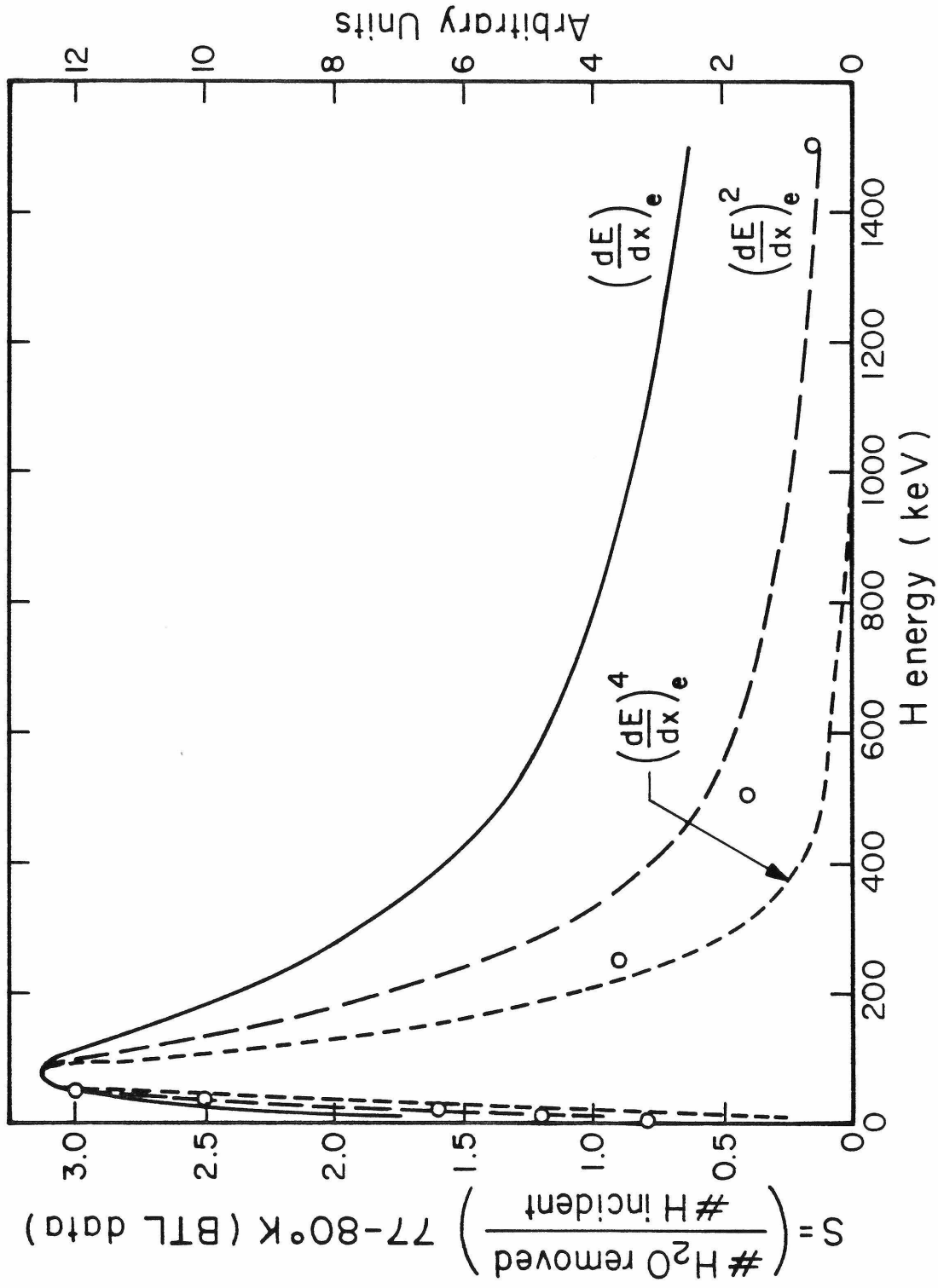
S = (# H2O removed / # H incident) 77-80°K (BTL data)
3.0
2.5
2.0
1.5
1.0
0.5
0
0
200
400
600
800
1000
1200
1400
H energy (keV)
Arbitrary Units
12
10
8
6
4
2
0
(dE/dx)e
(dE/dx)e2
(dE/dx)e4

Figure 4j

Figure 4j shows the erosion yield of ice by ^{4}He ions (Brown *et al.* 1980a). Also shown on the graph are arbitrarily normalized curves of (dE/dx), $(dE/dx)^2$, and $(dE/dx)^4$ obtained from experimental measurements of dE/dx from Matteson *et al.* (1977).

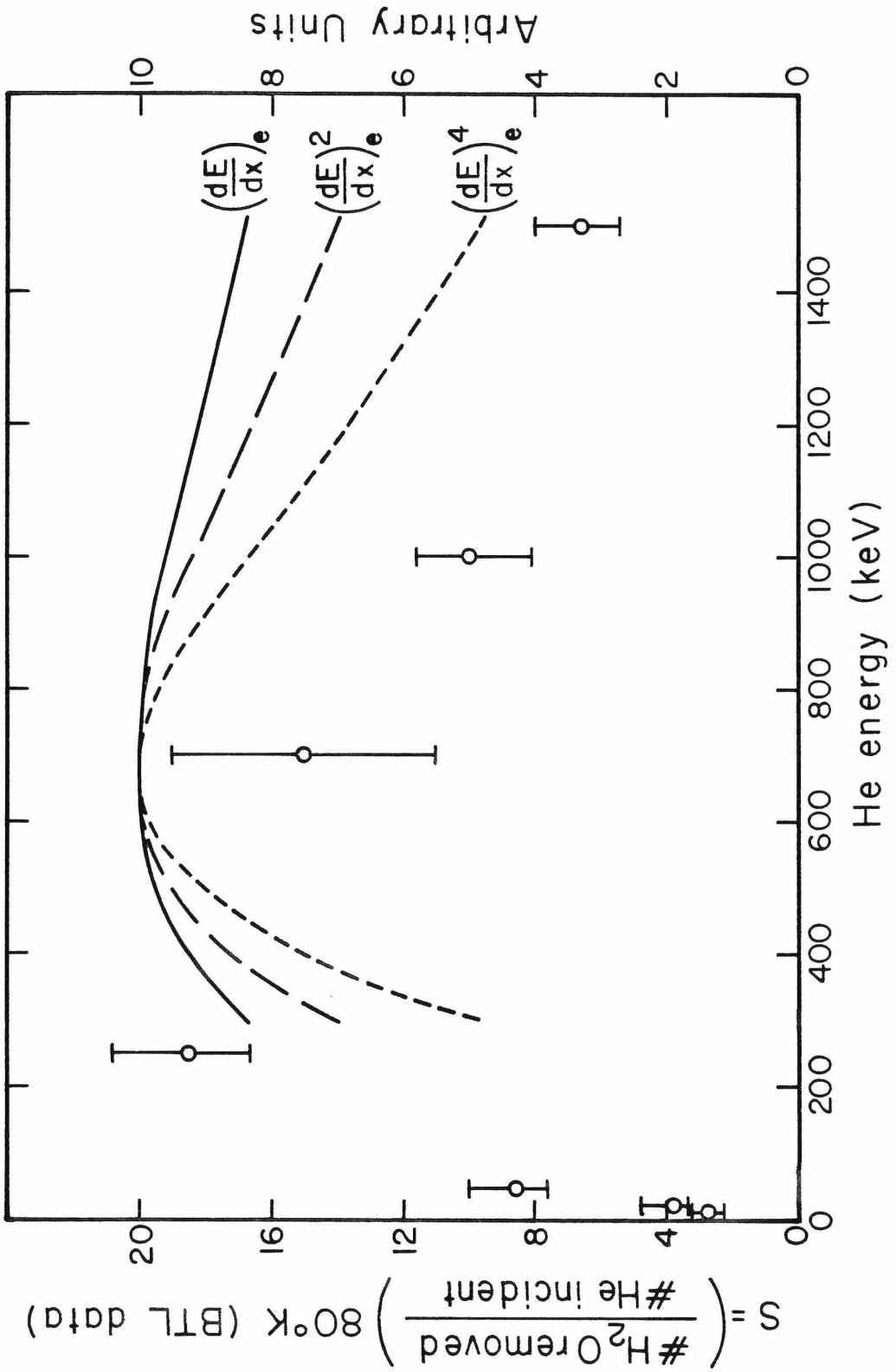
$S = \left(\frac{\#H_2O \text{ removed}}{\#He \text{ incident}} \right)$ 80°K (BTL data)
Arbitrary Units
He energy (keV)
$\left(\frac{dE}{dx}\right)_e$
$\left(\frac{dE}{dx}\right)_e^2$
$\left(\frac{dE}{dx}\right)_e^4$

Figure 4k

Figure 4k shows a comparison of the sputtering yields of ^{19}F erosion of H_2O and UF_4 targets (Griffith et al. 1980). The yields for the H_2O are divided by 200.

Also shown are (dE/dx) for F on H_2O and 1/4(dE/dx) for F on UF_4. Both of these stopping power curves were obtained using Bragg's rule and stopping power data given by Ziegler (1980).

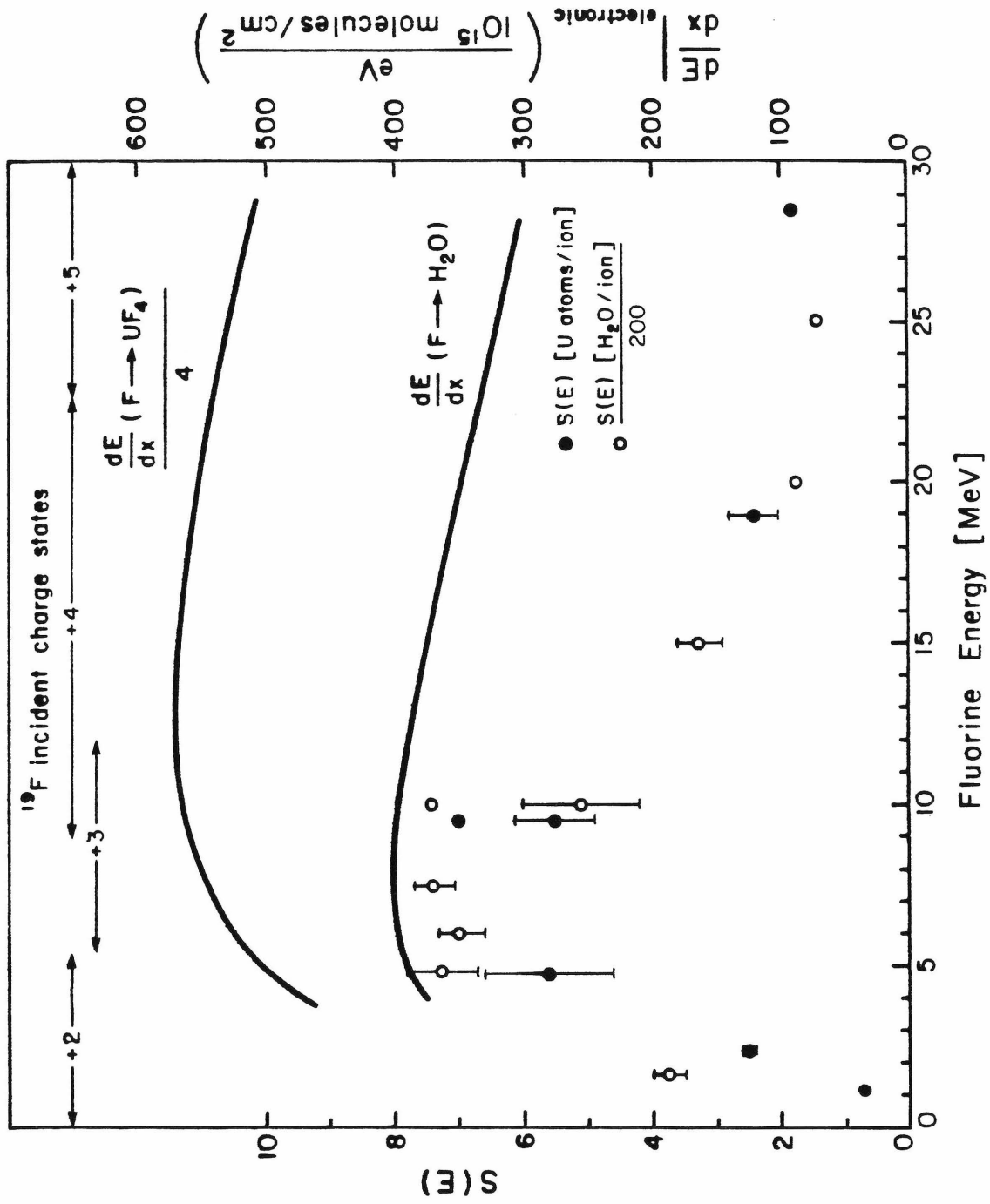
S(E)
Fluorine Energy [MeV]
$\frac{dE}{dx}\Big|_{electronic}$ $\left(\frac{eV}{10^{15}\ molecules/cm^2}\right)$
^{19}F incident charge states
+2
+3
+4
+5
$\frac{dE}{dx}(F \rightarrow UF_4)$ / 4
$\frac{dE}{dx}(F \rightarrow H_2O)$
● S(E) [U atoms/ion]
○ $\frac{S(E)\ [H_2O/ion]}{200}$

Figure 5a

Figure 5a shows the thermal diffusivity of ice as a function of temperature.

$$K = \frac{\kappa}{C\rho}$$

κ = thermal conductivity of polysrystalline ice (Fletcher 1970)

C = heat capacity of amorphous ice (Sugisaki 1968)

ρ = density of ice, 1 gm/cm^3

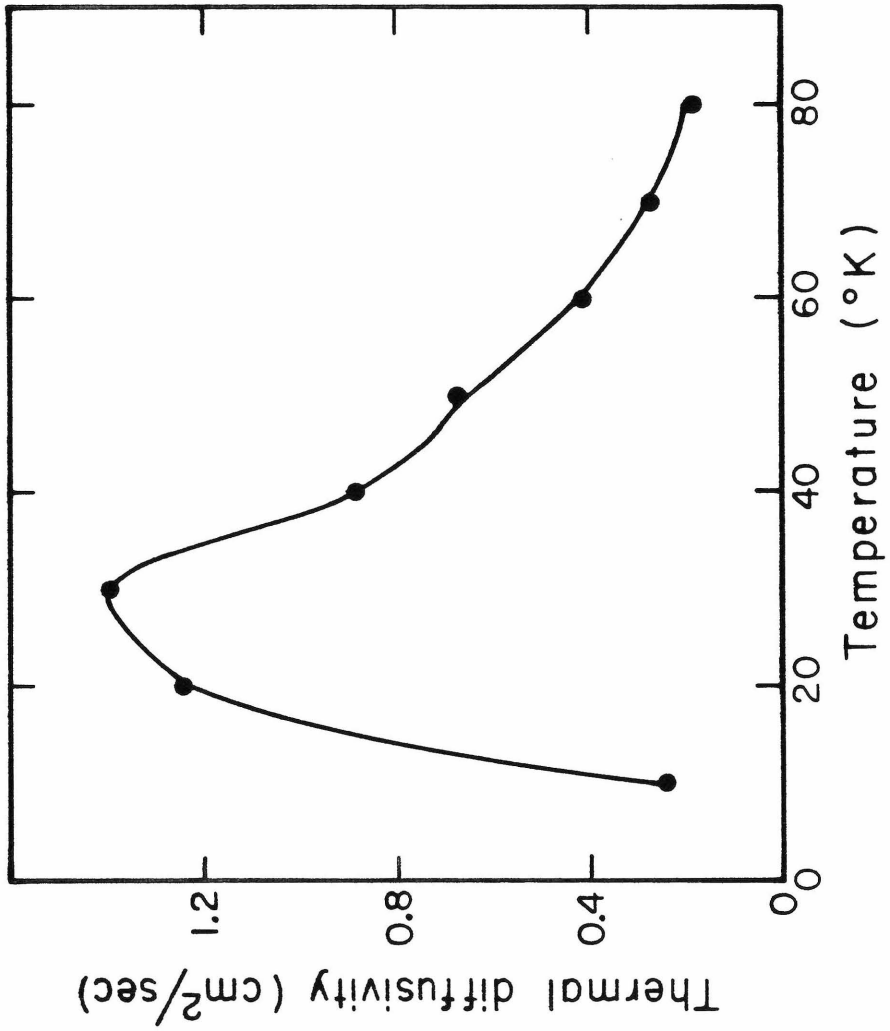
Thermal diffusivity (cm²/sec)
1.2
0.8
0.4
0
0
20
40
60
80
Temperature (°K)

Figure 5b

Figure 5b shows the results of measurements of the sputtering yield of H_2O at ~10°K by ^{19}F ions as a function of the F energy. The two curves are $(dJ/dx)^4$ where

$$dJ/dx(E) = A \frac{(Z^*(E))^2}{E} ln(BE)$$

B = 35 amu/MeV, 45 amu/MeV

Z^* = effective charge calculated from a formula given by Ziegler (1980)

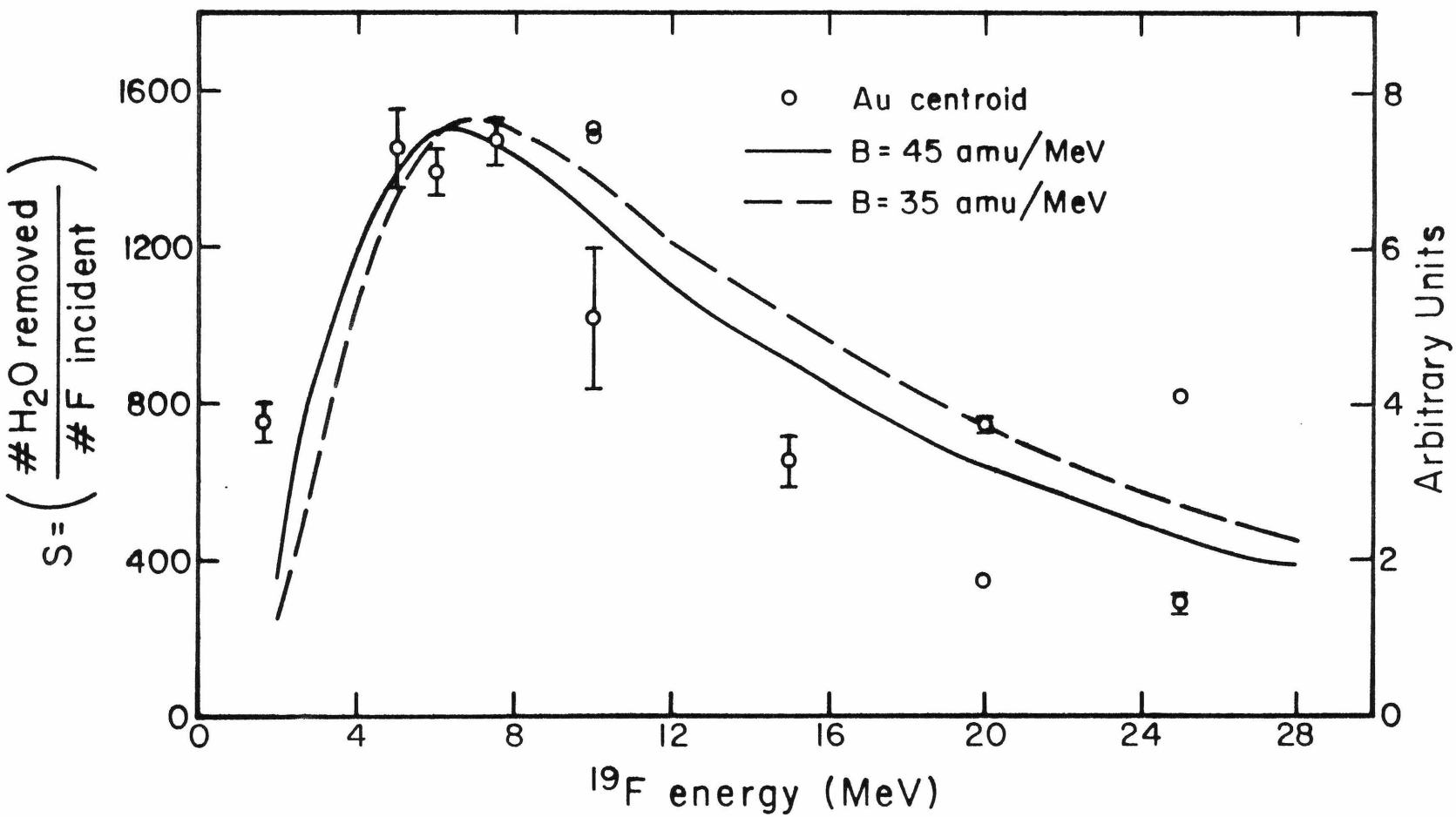
Au centroid
B = 45 amu/MeV
B = 35 amu/MeV
$S = \left(\frac{\#H_2O \text{ removed}}{\#F \text{ incident}} \right)$
Arbitrary Units
^{19}F energy (MeV)
0
400
800
1200
1600
2
4
6
8
12
16
20
24
28

Figure 5c

Figure 5c shows the resluts of measurements of the sputtering yields of H_2O (~10°K) by ^{19}F ions as a function of the F energy. The three curves represent (dE/dx), $(dE/dx)^2$, and $(dE/dx)^4$, where (dE/dx) values were calculated using Bragg's rule and data from Ziegler (1980).

Also shown on the graph are values of the equilibrium charge states (Ziegler 1980), and the incident charge states of the F beams used in the sputtering runs.

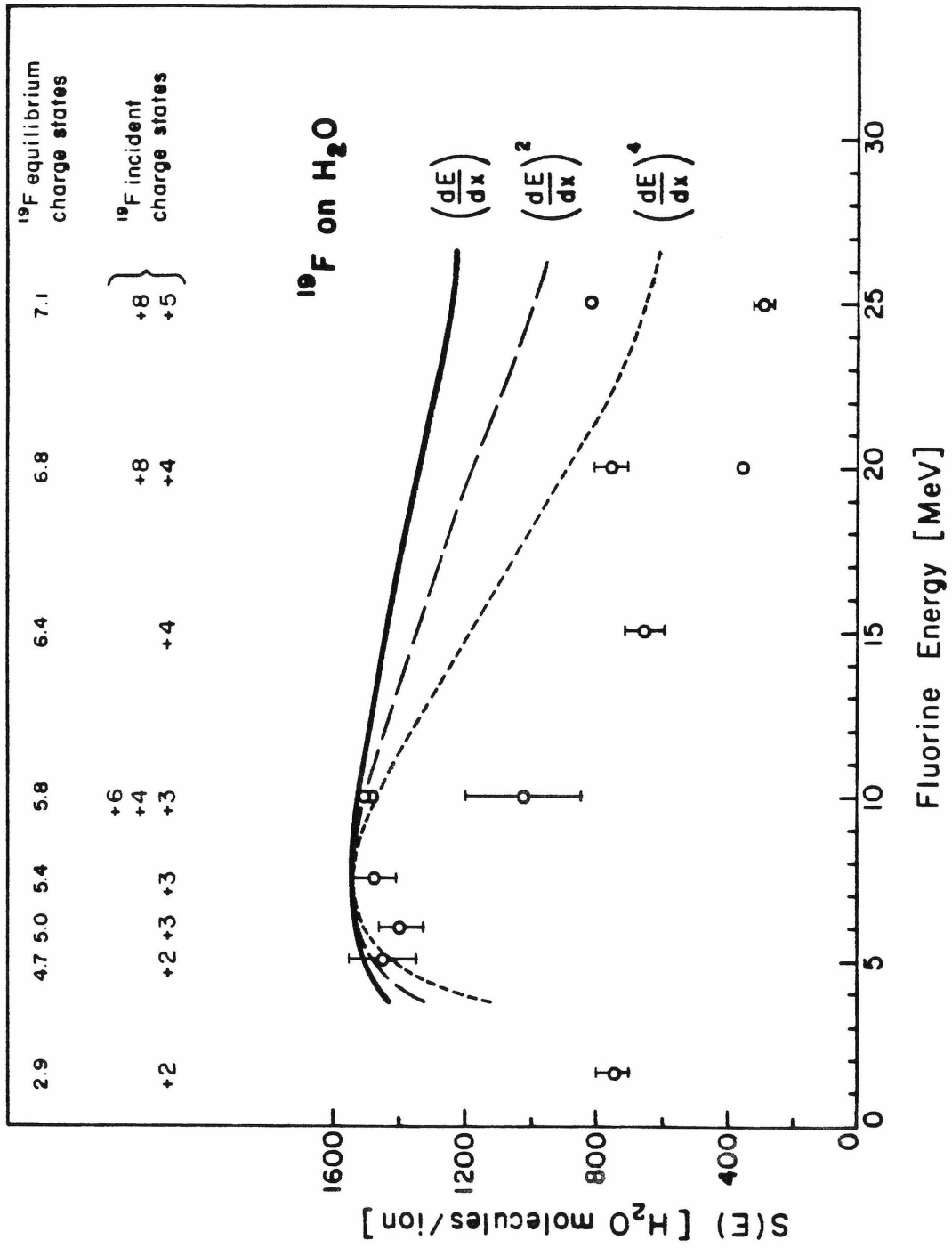
^{19}F on H_2O
$\left(\frac{dE}{dx}\right)$
$\left(\frac{dE}{dx}\right)^2$
$\left(\frac{dE}{dx}\right)^4$
^{19}F equilibrium charge states
2.9
4.7 5.0 5.4
5.8
6.4
6.8
7.1
^{19}F incident charge states
+2
+2 +3 +3
+6 +4 +3
+4
+8 +4
+8 +5
S(E) [H_2O molecules/ion]
Fluorine Energy [MeV]
0
400
800
1200
1600
5
10
15
20
25
30

Figure 5d

Figure 5d shows a graph of dE/dx vs S for H_2O targets bombarded with different ions. H ions; data from Brown and coworkers (1980a), dE/dx from Anderson and Ziegler (1977). He ions; data from Brown and coworkers (1980a), dE/dx from Ziegler (1977). F ions; data from the present work, dE/dx from Ziegler (1980).

Notice the "hairpin" shape of the F data; the arrow shows the direction of increasing energy.

To guide the eye, curves of $(dE/dx)^2$ and $(dE/dx)^4$ are also shown on the figure.

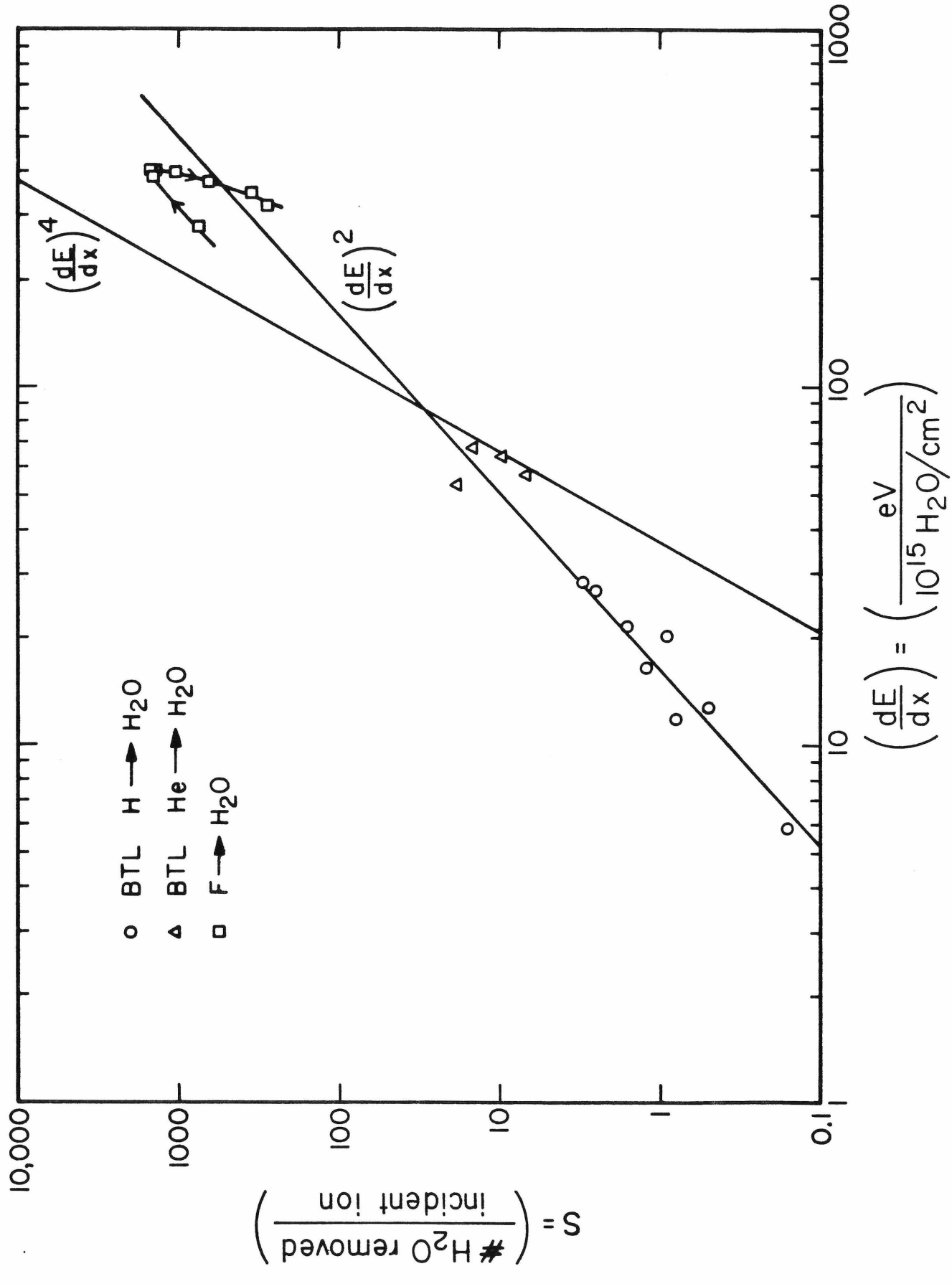
10,000
1000
100
10
1
0.1
1
10
100
1000
$S = \left(\frac{\#\ H_2O\ \text{removed}}{\text{incident ion}}\right)$
$\left(\frac{dE}{dx}\right) = \left(\frac{eV}{10^{15}\ H_2O/cm^2}\right)$
$\left(\frac{dE}{dx}\right)^4$
$\left(\frac{dE}{dx}\right)^2$
o BTL H → H_2O
Δ BTL He → H_2O
□ F → H_2O